Investigation of the diffusion behaviour of aluminium in different semiconductors

by

Thilo Michael Hauser

Submitted in partial fulfilment of the requirements for the degree

PHILOSOPHIAE DOCTOR

in the

Faculty of Science (Department of Physics)

University of Pretoria

Pretoria

December 1999

Supervisor: Professor E. Friedland

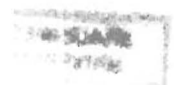

UNIVERSITEIT VAN PRETORIA
UNIVERSITY OF PRETORIA
YUNIBESITHI YA PRETORIA

SUMMARY

Investigation of the diffusion behaviour of aluminium in different semiconductors

by

Thilo Michael Hauser

Supervisor: Professor E. Friedland

Physics Department

Submitted in partial fulfilment of the requirements for the degree Philosophiae Doctor in the Faculty of Science.

In the semiconductor technology aluminium is used for the production of contacts as well as a dopant. When such a semiconductor-aluminium compound in an electronic circuit is exposed to heat or radioactivity its physical properties can alter due to thermal and radiation enhanced diffusion. It is important to know the diffusion behaviour of these compounds to predict lifetimes of circuits. However, reported diffusion coefficients of aluminium in several previously investigated semiconductors are contradictory. It is important to understand the reasons for these discrepancies and additional measurements with different analysing methods have to be performed under well-controlled conditions. Furthermore diffusion data of aluminium in several compound semiconductors investigated in this study are not available.

The semiconductors investigated in this study were silicon, germanium, indium phosphide, indium antimonide and gallium arsenide. Two different methods were applied to analyse the diffusion behaviour of aluminium in these semiconductors. Firstly thin aluminium films were deposited by vapour deposition onto the investigated semiconductors. Secondly, samples were implanted at room temperature and at T_i = 250 °C with a fluence of 5 x 10^{16} aluminium ions cm^{-2}.

Aluminium depth profiles for both methods were obtained by nuclear reaction analysis (NRA) before and after isochronal annealing at different temperatures. NRA is an isotope specific method that has various advantages over other analysing methods. The $^{27}Al(p,\gamma)^{28}Si$ reaction at a proton energy of 992 keV was applied to detect aluminium atoms. Diffusion coefficients as well as the detection limits of this method were extracted from a comparison of the depth profiles before and after annealing.

Additional channeling analysis in a backscattering geometry was performed to analyse the radiation-induced damage during the implantations and their recovery after isochronal annealing.

UNIVERSITEIT VAN PRETORIA
UNIVERSITY OF PRETORIA
YUNIBESITHI YA PRETORIA

SAMEVATTING

Studie van die diffusiegedrag van aluminium in verskillende halfgeleiers

deur

Thilo Michael Hauser

Promotor: Professor E. Friedland

Departement Fisika

Voorgelê ter gedeeltelike vervulling van die vereistes vir die graad Philosophiae Doctor in die Fakulteit Natuurwetenskappe.

In die halfgeleierindustrie word aluminium vir kontakte sowel as doteermiddel gebruik. Wanneer so 'n halfgeleier-aluminium verbinding in 'n elektroniese stroombaan aan warmte of radioaktiwiteit blootgestel word, kan sy fisiese eienskappe as gevolg van termies- en stralings-versnelde diffusie verander. Dit is belangrik om die diffusie-gedrag van hierdie verbindings te ken om die leeftye van stroombane te voorspel. In die literatuur is uiteenlopende diffusiekoëffisiënte vir aluminium in 'n aantal halfgeleiers gepubliseer. Dit is belangrik om die redes hiervoor te verstaan en verdere metings met verskillende tegnieke onder beheerde omstandighede is derhalwe nodig. Verder is diffusie-data van aluminium in verskeie saamgestelde halfgeleiers wat in hierdie studie ondersoek is, nie beskikbaar nie.

Die halfgeleiers wat in hierdie studie ondersoek is, is silikon, germanium, indiumfosfied, indiumantimonied en galliumarsenied. Twee verskillende tegnieke is gebruik om die diffusiegedrag van aluminium in hierdie halfgeleiers te ondersoek. Eerstens is dun aluminiumlagies op die halfgeleiers opgedamp. Tweedens is die halfgeleier by kamertemperatuur en 250 °C met 'n dosis van 5×10^{16} aluminiumione cm^{-2} geïnplanteer.

Aluminiumdiepteprofile is vir albei metodes deur middel van kernreaksieanaliese (NRA) voor en na isochroniese uitgloeiing by verskillende temperature bepaal. NRA is 'n isotoopspesifieke tegniek met verskeie voordele bo ander tegnieke. Die $^{27}Al(p,\gamma)^{28}Si$-reaksie by 'n protonenergie van 992 keV is gebruik om aluminiumatome waar te neem. Diffusiekoeffisiënte sowel as die gevoeligheid van hierdie tegniek is verkry deur die diepteprofiele voor en na uitgloeiïng te vergelyk.

Hierbenewens is kanaliseringsanalise in 'n terugverstrooiingsgeometrie uitgevoer om die uitgloeigedrag van die stralingskade wat deur die inplantering veroorsaak is, te bepaal.

UNIVERSITEIT VAN PRETORIA
UNIVERSITY OF PRETORIA
YUNIBESITHI YA PRETORIA

Acknowledgements

I would like to thank the following persons for their contribution towards this study:

My supervisor, Professor E. Friedland for giving me the opportunity to make my PhD in South Africa and for his guidance and support throughout this study.

Mr. Roelf van Weele and Mr. Gerrit Pretorius for their help and technical support.

Professor G. Myburg for the deposition of the thin films and lots of good tips.

Mr. W. Meyer for his help with the Afrikaans translation.

Mr. S.R. Naidoo for the implantations at the Schonland Research Center for Nuclear Sciences.

Professor J. Malherbe, Professor H. Alberts, Professor S. Kalbitzer, Professor F.D. Auret, Professor H.L. Gaigher, Dr. M. Hayes, Dr. N. v.d. Berg and Mr. N. Kemp for fruitful discussions and encouragement.

TABLE OF CONTENTS

CHAPTER 1:	**INTRODUCTION**	**1**
CHAPTER 2:	**DIFFUSION**	**3**
2.1. :	Diffusion coefficient	3
2.2. :	Diffusion mechanisms in solids	4
2.2.1. :	Diffusion in semiconductors	7
2.3. :	Methods for analysing diffusion coefficients	8
2.4. :	The finite difference method	10
CHAPTER 3 :	**STOPPING OF IONS IN SOLIDS**	**12**
3.1. :	Energy loss	12
3.1.1. :	Nuclear cross section	13
3.1.2. :	Electronic cross section	15
3.2. :	Energy loss in compounds	17
3.3. :	Energy straggling	18
3.4. :	Mean range and range straggling	20
CHAPTER 4 :	**NUCLEAR REACTION ANALYSIS (NRA)**	**22**
4.1. :	Nuclear reactions	23
4.2. :	Electromagnetic transitions	23
4.3. :	Depth profiling by using narrow resonances	26
4.3.1. :	Depth resolution	27
CHAPTER 5 :	**EXPERIMENTAL**	**29**
5.1. :	Sample preparation	29
5.1.1. :	Silicon	30

5.1.2. : Germanium 30

5.1.3. : Gallium arsenide 31

5.1.4. : Indium phosphide 31

5.1.5. : Indium antimonide 32

5.2. : Implantations 32

5.3. : Annealing system 33

5.4. : The energy scanning system 33

5.5. : γ - Ray detection 35

5.6. : Data acquisition 36

5.6.1. : Setting of energy windows 38

5.6.2. : NRA measurements 38

5.6.3. : Magnet setting 39

5.7. : The $^{27}Al(p,\gamma)^{28}Si$ reaction 40

5.8. : Channeling 42

5.9. : Error calculations 44

5.10 : Diffusion analysis 44

CHAPTER 6 : PREVIOUSLY PUBLISHED RESULTS 46

6.1. : Elemental semiconductors 46

6.1.1. : Silicon 47

6.1.2. : Germanium 51

6.2. : Compound semiconductors 52

6.2.1. : Gallium arsenide 52

6.2.2. : Indium phosphide 56

6.2.3. : Indium antimonide 56

CHAPTER 7 : RESULTS AND DISCUSSION 58

7.1. : Silicon 58

7.1.1. : Aluminium diffusion into silicon 59

7.1.2. : Room temperature implantation 60

7.1.3. : Hot implantation 64

7.2. :	Germanium	72
7.2.1. :	Aluminium diffusion into germanium	72
7.2.2. :	Room temperature implantation	74
7.2.3. :	Hot implantation	76
7.3. :	Gallium arsenide	80
7.3.1. :	Aluminium diffusion into gallium arsenide	81
7.3.2. :	Room temperature implantation	82
7.3.3. :	Hot implantation	84
7.4. :	Indium Phosphide	89
7.4.1. :	Aluminium diffusion into indium phosphide	89
7.4.2. :	Room temperature implantation	91
7.4.3. :	Hot implantation	94
7.5. :	Indium antimonide	97
7.5.1. :	Aluminium diffusion into indium antimonide	97
7.5.2. :	Room temperature implantation	99
7.5.3. :	Hot implantation	101
CHAPTER 8 :	**SUMMARY OF RESULTS AND OUTLOOK**	**103**
8.1. :	Silicon	103
8.2. :	Germanium	105
8.3. :	Gallium arsenide	106
8.4. :	Indium phosphide	108
8.5. :	Indium antimonide	110
8.6. :	Outlook	112
APPENDIX A		**113**
REFERENCES		**114**

CHAPTER 1

INTRODUCTION

Diffusion and inter-diffusion between different solids has long been a subject of scientific studies going back to the last century. *Roberts-Austen* carried out one of the first quantitative investigations in 1896, when he reported his work on the fast diffusion of gold into solid lead at different temperatures [1]. He estimated the rate of gold diffusion by measuring the weight change after sectioning the lead. Diffusion history is reviewed in refs. [2,3]. Over the last 100 years many researchers studied inter-diffusion of solids and many different models of diffusion mechanisms were developed.

In recent years with the rapid development of semiconductors, diffusion became of great technological importance for manufacturing *p-n* junctions in elementary semiconductors. Different diffusion models in solids and in particular in semiconductors are discussed in chapter 2.

Aluminium is still widely used for contacts on semiconductors. As a group *III* element it can also be used as an acceptor for group *IV* elemental semiconductors.
In the present work the diffusion of aluminium in different semiconductors was investigated. For analysing the in-diffusion, aluminium films were deposited onto clean silicon, germanium, gallium arsenide, indium phosphide and indium antimonide surfaces. To activate a possible in-diffusion, the semiconductor samples were annealed in vacuum at different temperatures. Depth profiles before and after every annealing step were compared to extract diffusion coefficients.

Further research was done on the aluminium diffusion within these semiconductors. Clean samples of the above mentioned semiconductors were implanted with aluminium at room temperature and at $T_i = 250$ °C at different dose rates. These samples were annealed for one hour in vacuum at different temperatures. The depth profiles of aluminium after implantation and after every annealing step were compared and diffusion coefficients were extracted.

The aluminium depth profiles were obtained by nuclear reaction analysis (NRA) by making use of the narrow $^{27}Al(p,\gamma)^{28}Si$ reaction at a proton energy of 992 keV. This non-destructive method has various advantages over other methods like Rutherford backscattering (RBS), as it is isotope sensitive and light elements in a heavy bulk can be analysed. In some of the analysed systems channeling measurements in backscattering geometry were performed to obtain additional information on radiation induced damage in the surface region of the specimen.

Chapter 3 summarises the concept of stopping powers of ions in solids. The p-γ resonance reaction applied in this research is described in chapter 4. Chapter 5 is on the experimental set-up as well as the sample preparation for the different diffusion experiments. The automatic energy scanning system, which provided a convenient tool for depth profiling with NRA is explained. The channeling of α - particles to determine the radiation induced damage before and after the different annealing steps is briefly discussed.

In chapter 6 previously published results in this field of research are reviewed. The discussion of the diffusion results of aluminium in the investigated semiconductors is presented in Chapter 7. Chapter 8 summarises the results of this work and gives a brief outlook.

CHAPTER 2

DIFFUSION

Heat conductivity, viscosity and diffusion are transport phenomena. Hence, the existing diffusion theories are derived from theories of heat flow through solid media that date back to Fourier and Lord Kelvin. In a diffusion process atoms or molecules are transported from a region of higher concentration to a region of lower concentration in a system, which can be of gaseous, liquid or solid nature. Diffusion alters physical and chemical properties of a system. It increases with temperature and can be enhanced by irradiation.

A proper study of diffusion mechanisms as well as diffusion coefficients for different systems is therefore necessary to predict modifications of solids in a hot or radioactive environment.

More recent diffusion studies are on semiconductor – impurity systems to predict their long time thermal stability [4].

2.1. DIFFUSION COEFFICIENT

Fick's first law of diffusion [5,6] macroscopically connects the diffusion coefficient D and the gradient of the concentration C to the flow rate J. In the differential form it can be written as:

$$J = -D \, grad \, C \tag{1}$$

In equation 1 the transfer rate of atoms per unit area is calculated. The definition constitutes the theoretical basis of most experimental methods for determining diffusion coefficients in generally used methods such as the chemical and tracer techniques and the *p-n-* junction method which is a specific method for semiconductors (chapter 2.3.).

Ficks's second law, also called the general diffusion equation, can be derived from equation (1) by assuming diffusion in the positive x - direction of a cylinder of unit cross section. From the continuity equation:

$$\frac{\partial C}{\partial t} + div\, J = 0 \tag{2}$$

Fick's second law can be derived after inserting equation (1):

$$\frac{\partial C}{\partial t} = D\, div\, grad\, C = D\, \nabla^2\, C \tag{3}$$

The solutions of these differential equations depend strongly on the boundary conditions of an experiment. Equation (3) is often expressed in spherical polar co-ordinates and in cylindrical co-ordinates [7] depending on the geometry of the experimental set-up.
For a semi-infinite medium equation (3) can be analytically solved [7]:

$$C(x,t) = \frac{1}{2\sqrt{\pi D t}} \int_0^{\infty} C(\xi,0) \left[\exp\left(-\frac{(\xi - x)^2}{4Dt} \right) \pm \exp\left(-\frac{(\xi + x)^2}{4Dt} \right) \right] d\xi \tag{4}$$

where $C(\xi,0)$ is the initial distribution. The positive sign is for a reflecting surface, the negative sign for a permeating surface.

For high temperatures the diffusion coefficient is found to obey an Arrhenius equation:

$$D(T) = D_0 \exp\left(-\tfrac{E_A}{kT}\right) \tag{5}$$

with the Boltzmann constant k and the Temperature T in units of Kelvin. Here the diffusion is characterised by just two quantities, the pre-exponential factor or diffusion constant D_0 and the activation energy for diffusion E_A.

2.2. DIFFUSION MECHANISMS IN SOLIDS

An ideal crystal consists of a perfectly ordered array of atoms, ions, or molecules in three dimensions. There cannot be atomic diffusion in a perfect lattice, which conserves its ideal order under all circumstances. But most crystals are far from being ideal. An actual evidence of the fact that crystals are not ideally ordered under all conditions lies in the existence of diffusion.

Existing defects in a crystal can be vacancies (Schottky-defects) or displaced atoms from their regular lattice sites to interstitial sites. Such an interstitial atom together with its vacated lattice site is called a Frenkel-pair. Extended defects in a crystal are agglomerates of vacancies (point defect clusters) or interstitials, dislocations and grain boundaries.

Investigations on point defects in a crystal can be performed after their artificial creation, which is achieved by quenching from high temperatures, through plastic deformation or after irradiation with particles or γ-rays [8].

Some interstitial sites and most of the above mentioned defects are locations of minimum energy for displaced and for impurity atoms. For an atom to move from one of these sites to another site of minimum energy a certain amount of energy, the so-called activation energy is required. A vacated lattice site (vacancy) can also start to move or diffuse when energy above a threshold energy is applied. However, the migration energy for vacancies in a solid is much larger than that for interstitials ($E_{AV} >> E_{AI}$).

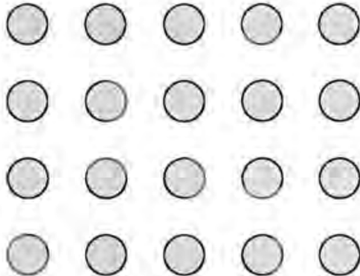

Fig.1: Undisturbed lattice

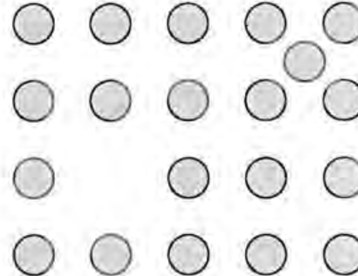

Fig.2: Frenkel disorder in a two dimensional lattice.

In thermal equilibrium the number of vacancies n in a solid with N atoms is given by:

$$\frac{n}{N-n} = \exp\left(-E_V / k_B T\right) \tag{6}$$

where E_V is the energy to displace one atom from its lattice site to the surface.

Lattice defects and impurities can influence the thermal atomic diffusion in a solid. The diffusing atoms can be trapped at such lattice defects where they can precipitate, segregate or

undergo chemical reactions with the matrix elements. To describe a Fickean diffusion process in the presence of trapping, a source and a sink term have to be added to equation (3):

$$\frac{\partial C_F(x,t)}{\partial t} = D\frac{\partial C_F(x,t)}{\partial x^2} - C_F(x,t)\left(\sum_i \mu_i(x,t)\right) + \sum_i \left(\nu_i C_{T,i}(x,t)\right) \tag{7}$$

C_F and $C_{T,i}$ is the concentration of the free and the trapped atoms respectively. μ_i describes the trapping probability for a certain trapping centre as a function of its radius r_i (typically a few Å) and the concentration of traps F_i:

$$\mu_i = 4\pi r_i D F_i(x,t) \tag{8}$$

ν_i is the dissociation frequency of the complex, which follows an Arrhenius type behaviour:

$$\nu_i = \nu_{i,o}\, e^{-E_i/kT} \tag{9}$$

where $\nu_{i,o}$ is about 10^{13} s^{-1} and E_i is the dissociation energy of the complex, which is typically between 0.8 and 2.5 eV.

The solid solubility of the diffusant in the solid also influences the diffusion behaviour. The diffusion constant depends inversely upon the solid solubility and is therefore small for self-diffusion, where the solute and the solvent are identical and the solute can occupy a regular lattice site without distorting the lattice.

It has become customary to classify impurities into 'slow' and 'fast' diffusers. Diffusion coefficients of 'slow' diffusers are in the same range or at most about 10^2 times higher than the self-diffusion coefficients of the investigated solids. 'Fast' diffusers usually diffuse several orders of magnitudes faster than 'slow' diffusers.

2.2.1. DIFFUSION IN SEMICONDUCTORS

With the importance of the semiconductor technology many diffusion data have been reported over the last years (see chapter 6). Diffusion processes play an important role in

various aspects of modern semiconductor technology. One of the most important applications is the generation of *p-n* junctions by diffusing impurity atoms into semiconductors at elevated temperatures, without melting the crystal or the formation of a liquid alloy. The diffusing impurities are either applied to the semiconductor surface in the gaseous state or as a solid or liquid compound. The depth and the sharpness of the junction can be controlled quite accurately by applying the desired amount of impurity atoms to the surface with a successive heat treatment.

The diffusion data of the elemental semiconductors silicon and germanium are in several respects different from those of metals. In a review on diffusion in silicon and germanium by Seeger and Chik [8] the following was reported on self-diffusion:

i. due to the low point defect concentration in the thermal equilibrium, the self-diffusion in semiconductors is much slower than in metals (more than 10^4 times),
ii. the pre-exponential factor D_0^{SD} is at least 10^2 times larger in germanium and 10^4 times larger in silicon than in metals,
iii. from (i) and (ii) it follows that the activation energies for self diffusion are much larger in silicon and germanium than in metals with comparable melting points.

In semiconductors, intrinsic defects such as vacancies and interstitials may be electrically charged and may therefore strongly interact with impurities such as donors and acceptors. In general, the intrinsic defects may exist in different charge states. The change in the Fermi level due to the addition of electrically active impurities affects the populations of these charge states and may thus have a strong influence on the observed diffusion coefficients.
For the elemental semiconductors silicon and germanium it was found that typical representatives of 'slow' diffusers are group *III* and group *V* elements of the periodic table, i.e. those usually employed as acceptors or donors in *p-n*-junctions. Group *I* and group *VIII* elements constitute the most important 'fast' diffusers. Therefore diffusion coefficients of group *III*- impurities are expected to be of the order of the self-diffusion coefficient (see Chapter 6).

In semiconducting compounds the diffusivity of impurity atoms depends on the vapour pressures of the components, since these have an influence on the concentrations of the various intrinsic point defects.

While in-diffusion is widely used to manufacture *p-n* junctions in elemental semiconductors difficulties of this method can occur in *III-V* device structures. The high vapour pressures of the group *V* elements lead to incongruent evaporation from the surface unless an overpressure or encapsulant is provided [9].

Other doping methods like ion-implantation can be applied for *III-V* semiconductors. The desired impurities are placed into the near surface region of the solid by first accelerating them to a high velocity and directing them as a beam onto the semiconductor surface. The ions are then able to penetrate the solid, and are gradually brought to rest. However, to anneal the damage introduced during the implantation requires displaced atoms to diffuse back to appropriate sites. This is sometimes not possible in *III-V* semiconductors for the diffusion lengths are not large enough to accomplish complete regrowth. An application of this method lies in the production of semi-insulating layers in the surface area of the *III-V* semiconductor.

To avoid extended defects, implantations at elevated temperatures are performed into elemental and compound semiconductors, where due to an increased mobility of point defects radiation induced damage can be largely avoided. This method is also known as dynamic annealing.

2.3. METHODS FOR ANALYSING DIFFUSION COEFFICIENTS

Apart from nuclear reaction techniques, which is used in this study (described in chapter 4) a variety of other methods can be applied to analyse the diffusion behaviour of impurities in solids. A widely used method for diffusion analysis is secondary ion mass spectroscopy (SIMS). In this technique the analysed specimen is subjected to sputtering. The material sputtered from the surface is analysed by mass spectrometry. The concentration of the investigated elements versus the sputter time is recorded from which the depth profiles are calculated.

The tracer method consists of introducing radioactive isotopes of the dopant into the studied solid. Thin layers of the investigated sample are mechanically or chemically removed and the concentration of the isotope in the removed layer is determined by measuring its radioactivity. An advantage of this method is the possibility of self-diffusion studies by using a radioactive isotope of the sample material as a diffusant.

The four-point probe method measures the conductivity of a thin layer just below the surface of a semiconductor. It can be applied in the investigation of concentration profiles of *n*-type dopants in *p*-type substrates or vice versa. Four equally spaced probes are applied to the semiconductor surface. A current I is passed between the two outermost probes and the voltage V between the two probes in the middle is measured. From the geometry of the specimen it is possible to calculate the amount of electrical active dopants. The diffusion profile of the dopant can be obtained by using a sectioning technique.

A similar method is obtained by carrying out the differential Hall measurements rather than simple conductivity measurements. Measurements are again taken before and after stripping thin layers from the diffused specimen. The values for mobility and carrier concentration are obtained at each stage and these data can be converted to a depth profile.

The *p*-*n*-junction method can be used for diffused acceptors into a homogeneous *n*-type sample. The junction occurs at the depth x_j where the concentration of the acceptors is equal to the concentration of the donors. From the concentration of donors N_D versus the depth x_j in the diffused material the depth profile of the acceptor can be extracted. Diffusion coefficients can be calculated from the difference in shape of the diffused profiles after various annealing temperatures.

2.4. THE FINITE DIFFERENCE METHOD

To evaluate a diffused profile a numerical method based on the finite difference method, described by Crank [10] was applied in this thesis. This method shall be described for a one-dimensional solution of Fick's laws.

For analysing the diffusion in a plane sheet with a constant diffusion coefficient D, the following dimensionless variables are introduced:

$$X = \frac{x}{l}, \qquad T = \frac{Dt}{l^2}, \qquad c = C/C_0 \tag{10}$$

where l is the thickness of the layer. C_0 and C are the initial and the diffused concentration, respectively. Advantages of these substitutions are that numbers occurring in the computation cover roughly the same range for all calculations and that the basic independent parameters are isolated. With these variables Ficks second law can be written as:

$$\frac{\partial c}{\partial T} = \frac{\partial^2 c}{\partial X^2} \tag{11}$$

The variation of an initial distribution $c(X)$ at a time T_0 is obtained by dividing the X-T space into intervals of δX and δT. For every lattice point (X_i, T_j) both sides of equation (11) can be developed by Taylor's expansion theorem. An expression for the left-hand side of equation (11) can be obtained from:

$$c_{i,j+1} = c_{i,j} + \delta T \left(\frac{\partial c}{\partial T} \right)_{i,j} + \frac{1}{2} (\delta T)^2 \left(\frac{\partial^2 c}{\partial T^2} \right)_{i,j} + ... \tag{12}$$

when neglecting second and higher order terms equation (12) is written as:

$$\left(\frac{\partial c}{\partial T} \right)_{i,j} = \frac{c_{i,j+1} - c_{i,j}}{\delta T} \tag{13}$$

A similar development leads to the expressions of the right hand side of equation (11):

$$c_{i+1,j} = c_{i,j} + \delta X \left(\frac{\partial c}{\partial X} \right)_{i,j} + \frac{1}{2} (\delta X)^2 \left(\frac{\partial^2 c}{\partial X^2} \right)_{i,j} + ... \tag{14}$$

$$c_{i-1,j} = c_{i,j} - \delta X\left(\frac{\partial c}{\partial X}\right)_{i,j} + \frac{1}{2}(\delta X)^2\left(\frac{\partial^2 c}{\partial X^2}\right)_{i,j} - .... \tag{15}$$

and after neglecting third and higher order terms:

$$\left(\frac{\partial^2 c}{\partial X^2}\right)_{i,j} = \frac{c_{i+1,j} - 2c_{i,j} + c_{i-1,j}}{(\delta X)^2} \tag{16}$$

Introducing equations (13) and (16) into equation (11):

$$c_{i,j+1} = c_{i,j} + r\left(c_{i-1,j} - 2c_{i,j} + c_{i+1,j}\right) \tag{17}$$

with $r = \delta T / (\delta X)^2$.

With this the diffused concentration profile at any time can be calculated from the initial profile. This method converges for $r < 0.5$.

The schematic diagram in Fig.3 shows how this method is applied to analyse diffused spectra. After setting the required parameters such as boundary conditions and trapping distribution, a diffused profile is calculated from the initial profile with the finite difference method. This simulated profile is now compared with the experimentally obtained diffused profile. In case of good agreement of the two profiles the product *Dt* is obtained. In case of disagreement the initial parameters have to be changed and new calculations have to be performed.

For analysis of our depth profiles the computer code DIFFUS by Kashny [11,12] was used.

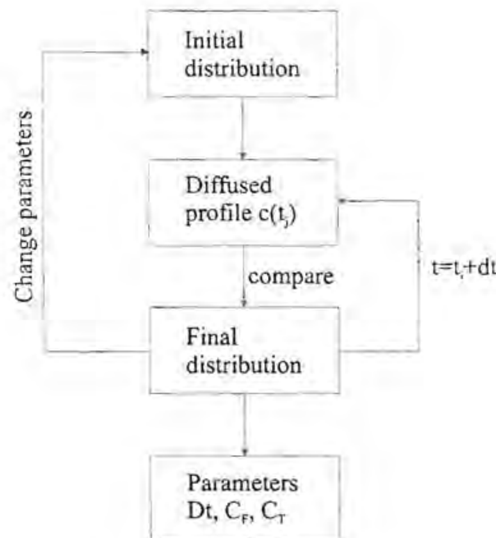

Fig.3: Schematic diagram of the data analysis with DIFFUS. The initially obtained aluminium depth distribution is used as initial distribution from which diffused profiles are calculated with the finite difference method.

CHAPTER 3

STOPPING OF IONS IN SOLIDS

When a charged particle with a certain velocity penetrates a solid, elastic and inelastic collisions with target atoms slow it down. The magnitude of this slowing down depends on the ion, its energy and the target material. For more than the last century stopping powers are of fundamental scientific interest. Various authors developed theories about energy loss mechanisms of charged particles that penetrate a target material. Several approaches are listed in ref.[13].

3.1. ENERGY LOSS

The final range distribution of energetic ions in a solid as well as the defect distribution is determined by the energy loss. The energy loss in a solid dE / dx is often called stopping power or specific energy loss. Here E is the ion energy and x is the distance within the target, usually measured along the instantaneous direction of the ion trajectory.

Two stopping processes that are considered to be ideally independent from each other can be distinguished. These processes are nuclear and electronic stopping. From their sum the total stopping power S is calculated to:

$$S = \frac{dE}{dx} = \left(\frac{dE}{dx}\right)_n + \left(\frac{dE}{dx}\right)_e \tag{18}$$

The stopping cross section ε is calculated from the stopping power divided by the target density N:

$$\varepsilon = -\frac{1}{N}\frac{dE}{dx} \tag{19}$$

The relative importance of the interaction process between ion and target medium depends mostly on the ion velocity and the charge state of the ion and target material.

3.1.1. NUCLEAR CROSS SECTION

Nuclear stopping of the projectile is caused from the elastic scattering by the screened atomic potential. At ion velocities v_1, significantly lower than the orbital velocities v_0 of the atomic electrons, the ion becomes neutralised by electron capture. Energy can be transferred from the nucleus of the projectile to that of a target atom by electrostatic interaction between the screened charges of the two nuclei.

The energy transfer T between the projectile and a target atom is calculated from energy and momentum conservation. It is a function of scattering angle θ (in the centre of mass system), projectile energy E, impact parameter b, mass of the projectile (M_1), mass of the target atoms (M_2) and the inter-atomic potential $V(r)$:

$$T(\theta, E) = \frac{4M_1 M_2}{(M_1 + M_2)^2} E \sin^2 \frac{\theta}{2} \tag{20}$$

The nuclear stopping is calculated from the integration over all impact parameters:

$$\varepsilon_n = \frac{\langle \Delta E \rangle_n}{N \, \Delta x} = 2\pi \int_0^{b_{max}} T(\theta, E) b \, db \tag{21}$$

θ depends on the inter-atomic potential $V(r)$. When assuming target atoms as positive point charges then $V(r)$ is the Coulomb potential. However, it has to be taken into account that target atoms are screened by their electrons. After introducing a screening function ϕ with a screening length a the inter-atomic potential can be written as [14]:

$$V(r) = \frac{Z_1 Z_2 e^2}{r} \phi\left(\frac{r}{a}\right) \tag{22}$$

Here r is the distance between the nuclei, e is the unit charge and $Z_{1,2}$ are the atomic numbers of the projectile and the target atom, respectively.

The charge distribution in a solid can be approximated by Hartree-Fock calculations. However, there is no analytical expression for the inter-atomic potential function $V(r)$ that is valid for all interaction radii. Several approximations for ϕ have been derived, each valid for a certain distance between the two atoms.

When separation of the atoms is small, e.g. up to about 0.2 Å, then the screening function due to Bohr can be applied:

$$\phi\left(\frac{r}{a}\right) = e^{\frac{r}{a}} \qquad (23)$$

$$a = a_0\left(Z_1^{2/3} + Z_2^{2/3}\right)^{-1/2}$$

with the Bohr radius $a_0 = 5.29 \times 10^{-11}\ m$.

Kalbitzer and Oetzmann [15] suggested a screening function ϕ with the universal screening length a:

$$\phi\left(\frac{r}{a}\right) = \left(e + r/a\right)^{\gamma \ln\left(1+\gamma^{-1} r/a\right)} \qquad ; \gamma = \tfrac{2}{3} \quad ; e = 2.718....$$

$$a = \frac{0.8854\, a_0}{Z_1^{0.23} + Z_2^{0.23}} \qquad (24)$$

With comparable accuracy, using the same universal screening length a, Ziegler, Biersack and Littmark (*ZBL*) [16,17] found the screening function phenomenological to be:

$$\phi\left(\frac{r}{a}\right) = 0.1818\, e^{-3.2 r/a} + 0.5099\, e^{-0.9423 r/a} + 0.2802\, e^{-0.4029 r/a} + 0.02817\, e^{-0.20162 r/a} \qquad (25)$$

This universal screening potential is useful for Monte Carlo calculations. It speeds up these calculations, but discrepancies with experimental results are observed for many projectile-target combinations.

3.1.2. ELECTRONIC CROSS SECTION

The electronic energy loss of an ion penetrating a solid can have different reasons [16].

- transfer of kinetic energy from the ion to the target electrons,
- plasma oscillations or other collective behaviour of the target electrons,
- charge transfer, e.g. excitation, ionisation or electron capture of the ion.

Because of the different processes involved it is not possible to describe the stopping of ions in a solid with one single theory. Different models are applied for the different ion energies and velocities. The validity of a theoretical approach is usually given within multitudes of the Bohr velocity v_0. A hydrogen atom at 25 keV atom moves with a comparable velocity as its orbital electron. The corresponding energy for a helium atom is at 252 keV. This energy is a function of the ion's mass and atomic number. It calculates to $E = Z_1^{4/3}\, A_1\, 25\ keV$.

Slow ions ($v_1 \le v_0\, Z_1^{2/3}$) cannot transfer enough energy to electrons that are much lower than the Fermi level to excite them to an unoccupied state. In this case only electrons that are close to the Fermi level can contribute to the energy loss.

The electronic stopping reaches its maximum near $v_1 = v_0\, Z_1^{2/3}$. For much higher ion velocities ($v_1 >> v_0\, Z_1^{2/3}$) mainly ionisation of the target atoms takes place. The ions transfer a much higher energy to the target electrons than their binding energy ($T >> I_1$).

i. Low Ion Velocities ($v_1 \le v_0\, Z_1^{2/3}$)

For low energies ($E < Z_1^{4/3}\, A_1$ 25 keV) the stopping of ions in solids was calculated by Lindhard, Scharff and Schiøtt (*LSS*) [18-20]. This projectile velocity is lower than the velocity of the target electrons. *LSS* calculate the electronic stopping by assuming a free electron gas with a density ρ that changes only slightly with the location.

The electronic cross section of a particle with Z_1 is obtained by integrating all interactions I with the electron gas over all volume elements:

$$\varepsilon_e = \int I(v,\rho)\left(Z_1^*(v)\right)^2 \rho dV \qquad (26)$$

The interaction with a charged particle is treated like a perturbation of the free electron gas. Therefore effects like polarisation and screening are taken into account. The state of the projectile can deviate from Z_1 through charge transfer and is therefore replaced by the projectile's effective charge Z_1^*. Electron capture and loss are in an equilibrium which depends mainly on the velocity of the projectile.

Lindhard found that the transferred energy from the projectile to the target electron and therefore also the electronic stopping cross section is proportional to the projectile velocity:

$$\varepsilon_e = 19.2 \frac{Z_1^{7/6} Z_2}{\left(Z_1^{2/3} + Z_2^{2/3}\right)^{3/2}} \frac{v_1}{v_0} \left[\frac{eV\,cm^2}{10^{15}\,at} \right] \tag{27}$$

with the Bohr velocity $v_0 = 2.19 \times 10^6\ m/s$.

ii. Bethe – Bloch Region ($v_1 >> v_0\, Z_1^{2/3}$)

The energy loss of a point charge in matter through collisions with electrons in the shell was already calculated by Bohr [21] in 1913. Bethe and Bloch [22,23] calculated quantum mechanical in Born approximation that the stopping cross section of a point charge can be obtained from:

$$\varepsilon_e = \frac{\langle \Delta E \rangle}{N\,\Delta x} = \frac{4\pi\, Z_1^2\, Z_2\, e^4}{m_e\, v_1^2} \left[\ln\left(\frac{2 m_e v_1^2}{\langle I \rangle} \right) - \frac{C_k(v_1)}{Z_2} \right] \tag{28}$$

where m_e is the electron mass, v_1 the velocity of the projectile, $\langle I \rangle$ the averaged ionisation potential and C_k shell corrections according to Bethe.

The main contribution for the energy loss in the Bethe – Bloch formula is from the first logarithmic term. Bloch estimated the ionisation potential $\langle I \rangle$ of the electrons to be approximately $\langle I \rangle = Z_2\ 10\ eV$ [23].

The last term $C_k\ (v_1)$ contributes shell corrections for low projectile velocities. The contribution of a certain electron shell in the target disappears when the projectile velocity is: $v_1 >> v_i$, with v_i being the electron velocity in the i-shell. This term is ~1 close to the maximum of the electronic cross section ε_e, where shell corrections come into account that limit the application of the Bethe-Bloch theory [24].

The Bethe-Bloch equation describes only the stopping of an ionised point charge correctly. Bohr [25,26] already assumed in 1940 that the projectile gets only stripped of those electrons whose classic orbital velocity is smaller than the projectile velocity. Therefore the projectile is stripped of all its electrons when $v_1 >> v_0 Z_1^{2/3}$ (Fig.4). This corresponds to a proton energy of about 250 *keV* and a helium energy of 2500 *keV*.

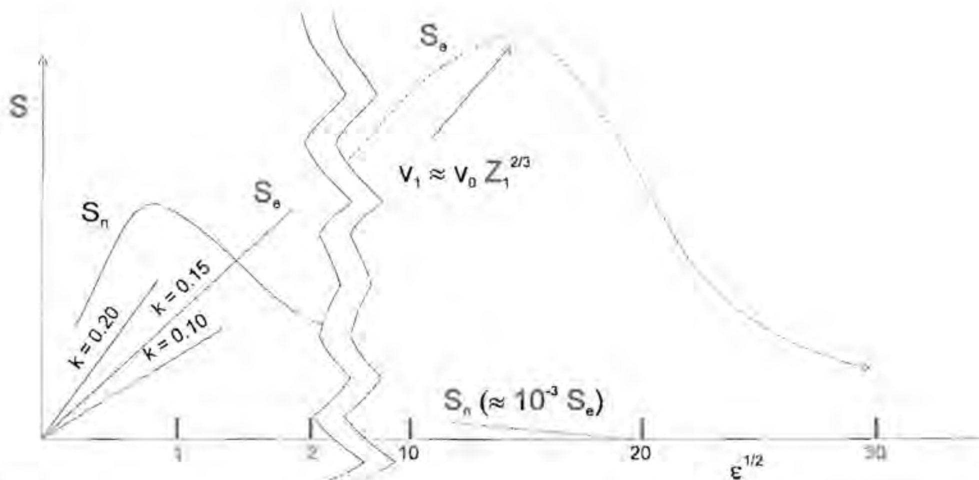

Fig.4: Nuclear (S_n) and electronic (S_e) stopping powers in reduced units versus energy in reduced units

3.2. ENERGY LOSS IN COMPOUNDS

Having a compound A_mB_n of two different elements A and B one can apply a simple additivity rule on the assumption that the interaction processes between ions and component target elements are independent of the surrounding target atoms. If ε^A is stopping cross section of element A and ε^B is the stopping cross section of element B one can write for the total stopping cross section:

$$\varepsilon^{AB} = m\varepsilon^A + n\varepsilon^B \tag{29}$$

where m and n denote relative fractions of the compound materials; $m + n$ is normalised to unity. This equation is known as Bragg's rule.

The energy loss however is found to be influenced by the chemical and physical state of the medium. Deviations of the order of 10% - 20% to Bragg's rule are found in experimental results around the stopping maximum for light organic gases and for solid compounds containing heavier constituents.

A model to correct for the chemical state was developed by Ziegler and Manoyan (1988) which is called 'cores and bonds' (*CAB*) model [27]. This model assumes the energy loss of ions in compounds to be due to the cores (closed electron shell of atoms) and the chemical bonds. Some of the so calculated stopping cross sections in organic compounds can be found in ref. [27]. However, for the calculation of the *CAB* corrections one has to know the bond structure of the compound. The largest differences between the *CAB* theory and predictions for Bragg's additivity rule are found near the stopping maximum. Differences reduce with increasing energy and finally disappear at about 10 v_0.

3.3. ENERGY STRAGGLING

Charged particles loose energy through many individual encounters in a target. The number of undergone collisions and the energy transferred with each collision is due to statistical fluctuations. These fluctuations are reflected in the second moment of the stopping powers of ions in a solid. The ions have an average energy loss ΔE due to the stopping powers $S(E)$ of the target material. However, the energy distribution also widens to $\delta\Delta E$ due to:

- statistical fluctuations in the nuclear energy loss
- statistical fluctuations in the electronic energy loss
- a change of the projectile charge state causes a change of the effective charge which results in a variation of the interaction.

All the above mentioned points contribute to energy straggling.

Fig. 5 shows a sketch on how the target thickness influences the energy straggling.

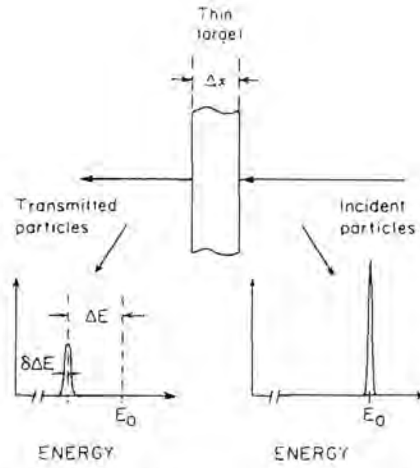

Fig.5: Influence of the target thickness on the energy loss and straggling [28].

i. Nuclear Energy Loss Straggling

The statistical fluctuations W_n^2 of the nuclear energy loss can be calculated in a similar way as the nuclear stopping by assuming a universal potential [15]:

$$\begin{aligned} W_n^2 &= \int_0^\infty T^2 \, d\sigma \\ &= 16\pi Z_1^2 Z_2^2 e^4 \frac{M_1^2}{(M_1+M_2)^2} F_n(\varepsilon) \end{aligned} \tag{30}$$

with: $F_n(\varepsilon) = \dfrac{1}{4 + 0.197\,\varepsilon^{-1.6991} + 6.584\,\varepsilon^{-1.0494}}$

and the reduced energy $\varepsilon = \dfrac{M_2\, a}{(M_1+M_2) Z_1 Z_2 e^2} E$

When $E \to \infty$ then the reduced energy $\varepsilon \to \infty$ and $F_n(\varepsilon) \to 0.24$. Therefore the maximum of the nuclear energy loss straggling tends to:

$$W_n^2 = 4\pi Z_1^2 Z_2^2 e^4 \frac{M_1^2}{(M_1+M_2)^2}$$

For high projectile energies the importance of W_n^2 is negligible compared to the electronic energy loss straggling Ω_B^2.

ii. Electronic Energy Loss Straggling

Bohr [29,30] used the same assumptions as in the Bethe – Bloch equation to derive the electronic energy loss straggling. For a point charge with a high velocity he got the relation:

$$\Omega_B^2 = 4\pi Z_1^2 Z_2 e^4 N\Delta x = W_e^2\, N\,\Delta x \tag{31}$$

Ω_B^2 is called Bohr straggling. It is the variance of the average energy loss of a projectile after passing through a layer of thickness Δx. For the number of independent collisions of the projectile with the target electrons Bohr assumed a Poisson distribution. From this a Gaussian energy loss distribution is obtained with a half width of Γ_B (with $\Gamma_B^2 = 8\, ln\, 2\; \Omega_B^2$).

3.4. RANGE AND RANGE STRAGGLING

The range straggling is the second moment of the range distribution. The total range $R = \sum l_i$ is the total distance that the particle travelled in the target as schematically seen in Fig.6. The projected range is defined as the mean depth from the target surface at which the ion comes to a halt.

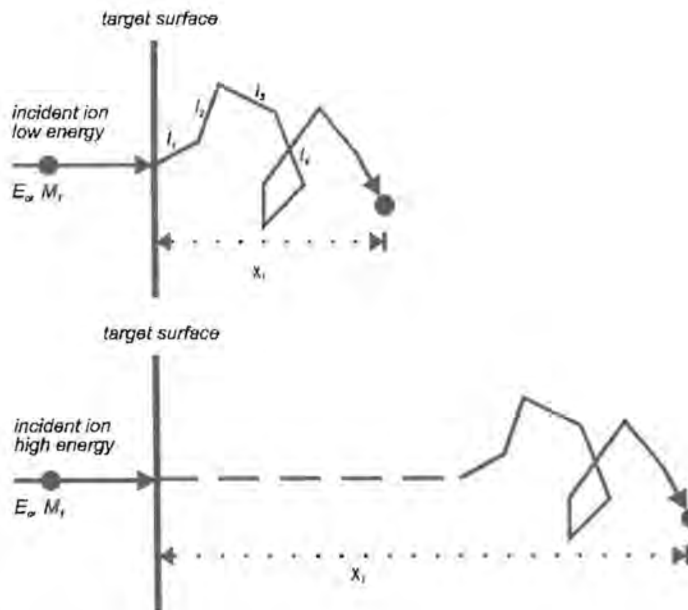

Fig.6: Range concepts for incident ions with low and high energies in a target material.

An ion incident onto a target changes its trajectory during collisions with target atoms until it comes to rest. Although the initial ion energy is fixed the number of collisions in a certain depth varies for every ion. The total distance travelled into the target is determined by the stopping powers.

The mean projected range R_p of the statistical distributed atoms after the implantation is calculated from:

$$R_p = \frac{\sum_i x_i y_i}{\sum_i x_i} \tag{32}$$

Here y_i stands for the number of particles stopped in $\Delta x = x_i - x_{i-1}$. The second range moment ΔR_p of the distribution is calculated from:

$$\Delta R_p = \sqrt{\frac{\sum_i (x_i - R_p)^2 y_i}{\sum_i y_i}} \tag{33}$$

This is also the standard deviation from the mean range R_p.

i14643042
b14353921

CHAPTER 4

NUCLEAR REACTION ANALYSIS (NRA)

Nuclear Reaction techniques for analysing near surface regions of solid samples are a convenient tool and have several advantages over other methods like Rutherford Backscattering (RBS) [31]. Nuclear reactions are isotope specific with no direct relationship between the mass of the target nucleus and the energy of the detected particle. Therefore light isotope tracing is possible even in heavy targets.

For NRA particles such as protons, alphas or deuterium are incident onto a target surface. When the particle penetrates the target with an energy that is high enough to overcome the Coulomb potential barrier V_C of the target nuclei it can induce a nuclear reaction. The Coulomb barrier is proportional to Z_1Z_2/R where $R = r_0\,(A_1^{1/3} + A_2^{1/3})$ with $r_0 \approx 1.25\,fm$. The nucleon numbers of the projectile and the target atoms are given by A_1 and A_2, respectively. Z_1 and Z_2 are the corresponding atomic numbers.

The barrier height for incident protons onto ^{27}Al calculates to $V_C = 3.74\,MeV$ [32]. Such high energies cannot be reached with our Van de Graaff accelerator. However, nuclear reactions can already be induced at lower energies due to tunneling effects of the projectile.

The barrier height becomes lower for decreasing atomic numbers, which makes *NRA* a suitable method to analyse light isotopes that are usually difficult to be detected by other methods.

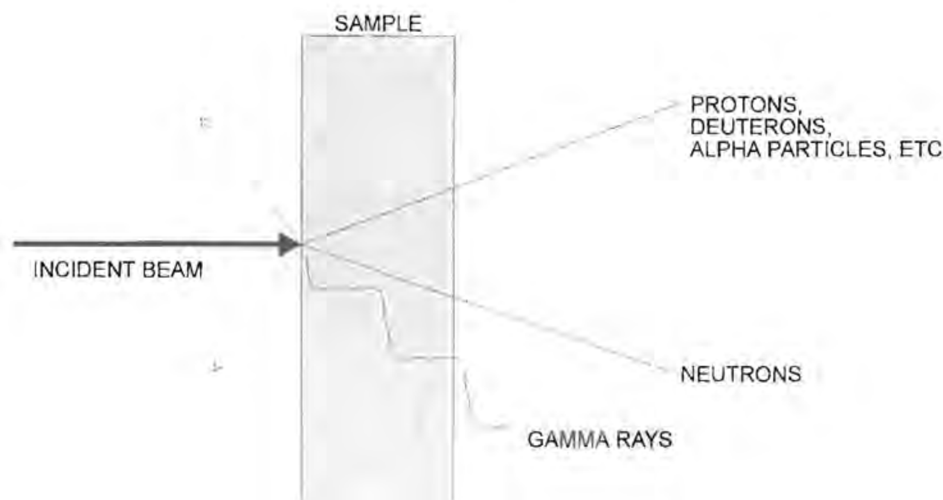

Fig.7: Schematic drawing of an incident ion beam onto a target with the various nuclear reaction products.

UNIVERSITEIT VAN PRETORIA
UNIVERSITY OF PRETORIA
YUNIBESITHI YA PRETORIA

4.1. NUCLEAR REACTIONS

Fig.7 displays a schematic diagram of an incident beam onto a target and its resulting reaction products. When a particle *a* hits a target nucleus *A* different processes can take place:

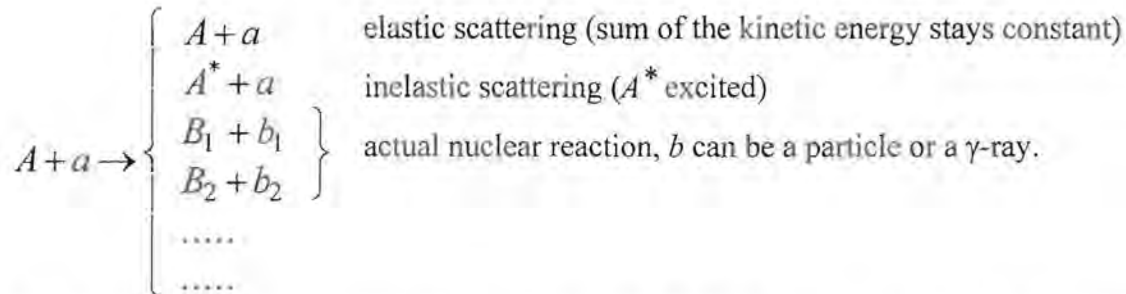

Usually a reaction is written in the form $A(a,b)B$. With the exception of the elastic scattering every resulting particle b shows an energy spectrum that contains information about the energy levels of the nucleus B. The angular distribution of the reaction particles holds information about the reaction mechanism.

Of interest for depth profiling with NRA are prompt reactions where the resulting radiation occurs instantaneously during irradiation, in contrast to activation techniques where the radiation is detected after irradiation. The resulting radiation is usually a gamma ray, a charged nuclear particle, a neutron or an electron.

4.2. ELECTROMAGNETIC TRANSITIONS

When a nucleus is in its ground state all its nucleons are in their lowest possible energy state that is allowed according to Pauli's principle. Similar to the atomic shell the state of a nucleus can be excited through energy transfer. The excitation can be the result of a single nucleon or several nucleons that are lifted from their ground state to a higher level. This can be caused by a radioactive fission, a nuclear reaction or by electromagnetic excitation from outside. When the excited state is a bound state the nucleus can only decay to its ground state by electromagnetic transition, which usually happens through the emission of a γ-ray. However, angular momentum and parity of the nucleus have to be conserved during this transition.

The eigenfunction of a nuclear state and its radiation field can be described by its angular momentum and parity eigenfunctions. Multipole fields are obtained from calculating the transition between two angular momentum eigenstates due to the conservation. These multipole fields are classified by the order l, which is an integer. For example, the lowest order $l=1$ is called dipole radiation.

One can distinguish between electric and magnetic multipole radiation. It is therefore customary to specify the kind of radiation field and the order l of the multipole. The terminology used is *M1* for a magnetic dipole transition and *E2* for an electric quadrupole transition.

The sum of the spins of the initial and final nuclear states $\vec{I}_1$, $\vec{I}_2$ and $\vec{l}$ of the emitted γ-ray stays constant due to conservation of the angular momentum. This leads to the following selection rules:

$$|I_1 - I_2| \leq l \leq I_1 + I_2 \quad ; \quad m = m_1 - m_2 \tag{34}$$

However, only transitions with low l are observed experimentally and in most cases the selection rules reduce to:

$$l = |I_1 - I_2| \tag{35}$$

During the emission process the parity must also be conserved which leads to additional selection rules. From the transformation characteristics of multipole fields one can deduce from the parity transformation $\vec{r} \to (-\vec{r})$ that the electric multipole radiation has the parity $(-1)^l$ and the magnetic multipole radiation has the parity $(-1)^{l+1}$. Therefore a transition can only take place when the parity π of the nuclear states before and after emission obey the following selection rules:

$$\pi_1 = (-1)^l \pi_2 \qquad \text{for } El \text{ radiation} \tag{36}$$

$$\pi_1 = (-1)^{l+1} \pi_2 \qquad \text{for } Ml \text{ radiation} \tag{37}$$

The emission of a γ-ray during an electric multipole transition causes the same parity change as an emitted particle with the angular momentum *l*.

change of spin $\|\Delta I\|$		0 no 0→	1	2	3	4	5
change of parity	yes	*E1* *(M2)*	*E1* *(M2)*	*M2* *E3*	*E3* *M4*	*M4* *E5*	*E5* *(M6)*
	no	*M1* *E2*	*M1* *E2*	*E2* *(M3)*	*M3* *E4*	*E4* *(M5)*	*M5* *E6*

Table 1: Multipole order of γ-transitions

The lowest multipole orders possible at a γ-transition for a given spin and parity are listed in table 1. Because of parity conservation there can never be *E* and *M* radiation of the same multipole order be emitted together. The transition probability is usually much smaller for magnetic radiation than for electric radiation of the same multipole order. With the selection rules it is possible that an *E2* and *M3* radiation can be emitted together. However, the *M3* radiation has a very small transition probability compared to the *E2* radiation. During a transition with $\Delta I = 1$ (no parity change) the transition probability of *E2* radiation is of the same order of magnitude as the *M1* radiation.

The quantum mechanical calculation of the transition amplitude is quite involved and is described in ref. [33].

In Fig.8 the calculated probabilities for different multipole transitions are sketched as a function of γ-energies for $A = 100$, $S = 1$ and $r_0 = 1.2\,fm$. At a γ-energy of 0.5 *MeV* the half times for transitions varies between 10^{-14} *s* (*E1*) and 10^{8} *s* (*E5, M5*). These calculations are only an approximation for the real interactions in a nucleus. The experimental values are usually slower by a factor 10^3 to 10^7 for the *E1* transition and faster by a factor of 10^2 for the *E2* transition. The values of the other transitions are in the right order of magnitude.

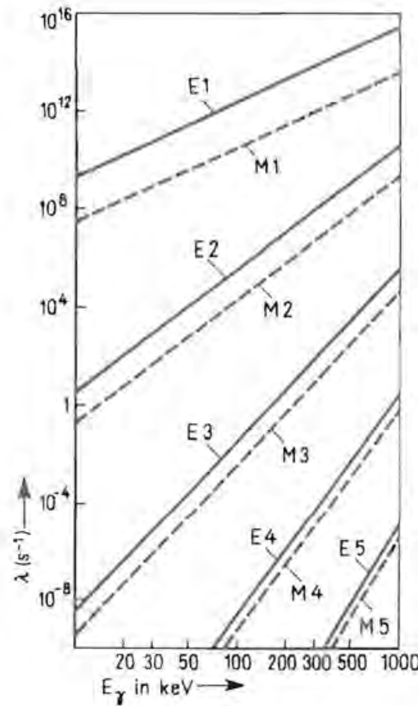

Fig.8: One particle transition probability calculated for different kinds of multipole radiation [34].

4.3. DEPTH PROFILING BY USING NARROW RESONANCES

Most of the light nuclei ($Z < 30$) have strong, sharp resonances in the cross section $\sigma(E)$ of the nuclear reactions, induced mainly with protons at low bombarding energies (< 3 MeV). Here the discussion is limited to resonances leading to prompt γ-ray emission.

When resonance reactions are used for depth profiling, the resulting γ-rays of the resonance reaction are counted versus the beam energy while the energy of the analysing beam is incremented, starting just below the resonance. The profiled depth is typically limited to a few microns.

An example for this method can be given by assuming a flat, laterally uniform sample that contains a homogeneous distribution $C(x)$ of an isotope of the element to be analysed. While bombarding the sample perpendicular to the surface with the analysing beam the induced γ-ray emission is detected. For beam energies lower than the ones required for the reaction the measured yield corresponds to background readings. After incrementing the beam energy to the one required the nuclear reactions can be induced at the surface of the sample. For higher beam energies the particles cannot induce a reaction at the surface of the sample. They get

slowed down within the target until they reach a certain depth x in the sample with the necessary energy for the nuclear reaction. As already discussed (chapter 3) the depth can be correlated to the energy loss of the projectile through the stopping powers of the target material. If the investigated isotopes are located in this depth the nuclear reaction can be induced. The detected γ-yield for this beam energy corresponds to the isotope concentration at this depth. The excitation curve of the resonance reaction $Y(E_b)$, where E_b stands for beam energy, gives an estimate of the isotope concentration distribution as a function of depth.

The depth x is correlated with the energy loss of the particles of the incident beam $(dE / dx)_{in}$ through the equation:

$$E_b = E_R + \left(\frac{dE}{dx}\right)_{in} \frac{x}{\cos\theta_1} \tag{38}$$

where θ_1 is the angle between the surface normal and the incident particle and E_R is the projectile energy where the resonance occurs. The energy loss $(dE / dx)_{in}$ can be approximated as constant within the small energy interval $E_0 \leq E \leq E_R$ (surface approximation).

4.3.1. DEPTH RESOLUTION

The experimental resonance width is broadened due to the natural width of the resonance, the energy resolution of the beam, and the energy straggling of the beam particles during the energy loss E_b - E_R. In order to deduce the precise shape of the actual concentration profile $N(x)$, the shape of the resonance cross section $\sigma(E)$, the energy distribution of the beam $g(E_b, E)$ and the energy straggling $f(E, E', x)$ of particles at depths x have to be taken into account. The excitation curve of the resonance reaction $Y(E_b)$, i.e. the yield of the reaction vs. the bombarding energy gives an estimate of the concentration distribution [35]:

$$Y(E_b) = K \int_0^\infty dx \int_0^\infty dE \int_0^\infty dE' N(x) g(E_b, E) f(E, E', x) \sigma(E') \tag{39}$$

K is a constant for given detection conditions. If the resonance is narrow and the beam energy resolution good, the functions g, f, and σ are sharp and therefore the yield curve corresponds well to the actual distribution.

The depth resolution depends on experimental parameters like the energy spread of the incident beam ΔE_b, the resonance width of the used reaction ΔE_R, the widening of the analysing beam energy $\Delta E_{ew}(x)$ in the depth x and the Doppler broadening ΔE_D due to the thermal motion of the reactant target atoms. By using a Gaussian approximation the total depth resolution as a function of the depth is obtained:

$$d(x) = \frac{\Delta E_{tot}(x)}{S(x)} \tag{40}$$

where:

$$\Delta E_{tot}(x) = \sqrt{\Delta E_b^2 + \Delta E_D^2 + \Delta E_R^2 + \Delta E_{ew}^2(x)} \tag{41}$$

In the set-up used for the experiments the accelerator energy beam spread was about 1 *keV*. In comparison to this the Doppler broadening and the resonance width of the $^{27}Al(p,\gamma)^{28}Si$ of about 105 *eV* are negligible.

The computer code PROFIL [36] corrects the obtained yield curves for straggling and instrumental resolution. In the first step this program calculates a depth profile from the experimental data, ignoring any energy resolution effects. It then computes from this concentration profile the expected shape of the spectrum, taking into account the determined resolution function. The difference between the calculated and experimental spectrum is then subtracted from the experimental spectrum and a new concentration profile is computed. This algorithm is repeated until the calculated spectrum coincides with the original experimental data within a given accuracy.

CHAPTER 5

EXPERIMENTAL

The diffusion behaviour of aluminium in the semiconductors silicon (Si), germanium (Ge), gallium arsenide (GaAs), indium phosphide (InP) and indium antimonide (InSb) was investigated by nuclear resonance analysis (NRA). The sample preparation from these materials is described in chapter 5.1., followed by a short description of the implantations that were performed. The annealing system as well as the analysing set-up are described. A summary of the automatic energy scanning system installed at the University of Pretoria is followed by a description of the (p,γ) reaction used for this work. A short summary of the channeling technique concludes this chapter.

5.1. SAMPLE PREPARATION

The surface of the investigated semiconductors had to be cleaned before they were implanted and before the thin aluminium films were deposited. The different semiconductors were cleaned and prepared as described in the following sub-chapters.

A successive heating of the same sample for investigation of the diffusion behaviour might influence the results by leading to difficulties in the reproducibility that might arise due to several heating and cooling cycles. Therefore larger pieces of every semiconductor were implanted or prepared by vapour deposition. Samples of about 5 x 5 *mm* were cut from these pieces. This ensures that all samples of a semiconductor are prepared in the same way for an experiment.

For every annealing temperature a different sample was annealed to exclude effects that could occur from multiple heating and cooling of the same sample. Another advantage of this annealing method is the possibility to check obtained results by repeating the annealing experiment with a sample that is prepared in the same way.

5.1.1. SILICON

The surface of a float-zone (FZ) Si <100> and a Si <111> B^+ - doped wafer was etched with a 2 % HF water solution in order to remove the oxide layer. Half of this wafer was immediately transferred into a vacuum system for deposition of the t = 20 *nm* aluminium film with a resistive evaporation technique.

For every annealing experiment two samples cut from this wafer half were placed into a quartz tube with the aluminium sides facing each other in order to prevent evaporation of aluminium during the annealing process (sandwich - method). The annealing system is described in chapter 5.3.

The remaining wafer half was cut in two and one of the quarters was implanted at room temperature, the other quarter at 250 °C. Samples were cut from these quarters after implantation for subsequent annealing for one hour in vacuum at T_a = 500, 700 and 900 °C. During the annealing process the samples were not covered in order to avoid interdiffusion of the implanted aluminium samples.

5.1.2. GERMANIUM

A <111> n-type germanium crystal of the size 25 x 25 x 1 mm was mechanically polished and chemically cleaned with HNO_3 and placed into a vacuum system. A t = 13 *nm* aluminium film was deposited onto the polished surface of half of this crystal with a resistive evaporation method. Samples were cut from this crystal with a diamond saw and annealed for one hour in vacuum at T_a = 500 and 700 °C. The germanium samples were not covered during annealing because pits were observed on the surface after annealing samples with the sandwich method. These pits are diffusion channels that influence the diffusion behaviour dramatically.

The remaining polished germanium half was cut in two. One quarter was implanted at room temperature and the other at 250 °C. The samples cut from these pieces were also not covered during annealing for one hour in vacuum at T_a = 700 °C.

5.1.3. GALLIUM ARSENIDE

The surface of an undoped <100> gallium arsenide wafer was degreased in trichloroethylene (TCE) and isopropanol. Hereafter it was rinsed in deionised water and chemically etched in H_2O_2 : NH_4OH : H_2O (ratio 1 : 3 : 150) followed by another rinse in water. The oxide was removed in HCL : H_2O (ratio 1 : 1) followed by a final rinse in deionised water.

The wafer was cut in half. One of the halves was transferred into a vacuum system for the deposition of the t = 17 *nm* aluminium film with the resistive evaporation technique mentioned above. Samples were cut from this piece and subsequently annealed for one hour in vacuum at T_a = 450 and 550 °C. During the anneal the sandwich method described for silicon in 5.1.1.was applied.

The remaining cleaned wafer half was cut in two. One of the quarters was implanted at room temperature and the other at T_i = 250 °C. The samples cut from these were subsequently annealed for one hour in vacuum at T_a = 350, 450 and 550 °C. During the anneal the samples were not covered.

5.1.4. INDIUM PHOSPHIDE

An undoped *n*-type <100> InP wafer was degreased in hot trichlorethane, acetone and isopropyl alcohol (ratio: 1 : 1 : 1) and rinsed in methanol and deionised water. The wafer was cut in the middle and one half was placed in a vacuum system for deposition of a t = 10 *nm* aluminium film with the resistive evaporation method. Samples were cut from this half and subsequently annealed for one hour in vacuum at T_a = 300 and 400 °C using the sandwich method.

The remaining clean wafer half was cut in two. One of these quarters was implanted at room temperature, the other at T_i = 250 °C. Samples were cut from these quarters and annealed for one hour at T_a = 300 and 400 °C in a vacuum system. During annealing the samples were not covered.

5.1.5. INDIUM ANTIMONIDE

The surface of a tellurium doped *n*-type <110> InSb wafer was cleaned with CP4 for 5 seconds. CP4 consists of HF, HNO_3 and CH_3COOH (ratio: 3 : 5 : 3). After cleaning, the disc was rinsed in deionised water and dried with nitrogen. The wafer was cut in half.

One of the halves was placed in a vacuum system for deposition of a t = 10 *nm* aluminium film onto the surface with the resistive evaporation system. Samples cut from this wafer were annealed for one hour in vacuum at T_a = 250 °C with the sandwich method.

The other cleaned wafer half was cut in two. One of the quarters was implanted at room temperature, the other at T_i = 250 °C. These samples were not covered during annealing for one hour at T_a = 250 °C in vacuum.

5.2. IMPLANTATIONS

All implantations were performed at the Schonland Research Centre for Nuclear Sciences at the University of the Witwatersrand (WITS) in Johannesburg with a Varian-Extrion implanter. Due to implanter problems beyond our control the ion energy could not be measured directly. It was indirectly determined as 120 *keV* by comparing the experimentally observed implantation profiles with TRIM [14] simulations. However, it must be stressed that a knowledge of the exact ion energy is of no importance for our investigation. The fluence of the implantation was for all samples $5x10^{16}$ aluminium ions cm^{-2}.

The implantations at room temperature were performed with a beam current of about 1 μA which corresponds to a dose rate of 1 x 10^{13} ions $cm^{-2}\,s^{-1}$. This rate is low enough to avoid excessive heating of the samples.

Hot implantations were performed at 250 °C with a beam current of about 3.4 μA which corresponds to a dose rate of 3.4 x 10^{13} ions $cm^{-2}\,s^{-1}$. The temperature of the heated sample holder was measured on the surface close to the samples with a thermocouple. During the implantation the temperature was kept within ± 20 °C.

Samples were tilted during implantations at an angle of 7° relative to the surface normal to avoid channelling of the ions during implantation.

5.3. ANNEALING SYSTEM

The samples were annealed in a 60 cm long cylindrical oven. The maximum temperature of this oven is at $T = 1000$ °C, which is reached in the middle of the oven with a slight gradient towards the sides. A thermal sensor with a feedback system keeps the adjusted oven temperature within $\Delta T = \pm 5$ °C.

For the annealing process the samples were placed in quartz-glass tube connected to a vacuum system. A thermocouple was placed next to the samples inside the quartz tube to provide the actual temperature at the location of the samples. The oven was heated to the desired temperature before it was shifted over the quartz-tube. The vacuum was better than 10^{-7} mbar while the quartz tube with the samples was in the oven.

Slight adjustments to the annealing temperature could be made, by moving the oven relative to the quartz-glass tube by making use of the temperature gradient inside the oven.

5.4. THE ENERGY SCANNING SYSTEM

For obtaining depth profiles with NRA the energy of the incoming protons has to be changed in a controlled manner which is difficult to realise by setting the analysing magnet every time the energy has to be changed. This is due to hysteresis effects and difficulties in setting the magnet reproducibly within $\Delta E = 500\ eV$ of the desired energy. Therefore an energy scanning system is necessary to change the proton energy in small reproducible steps. Various scanning methods are employed world-wide. The system installed at the University of Pretoria is based on a principle developed by Amsel et al. [37-39]. The accelerator group of the National Accelerator Centre (NAC) in Faure made the appropriate adaptation for our accelerator. The system is designed for proton energies up to 2.5 MeV and is able to step through a total energy range ΔE of some 40-100 keV.

Displayed in Fig. 9. is a schematic layout of the accelerator beamline, where the energy scanning system is installed.

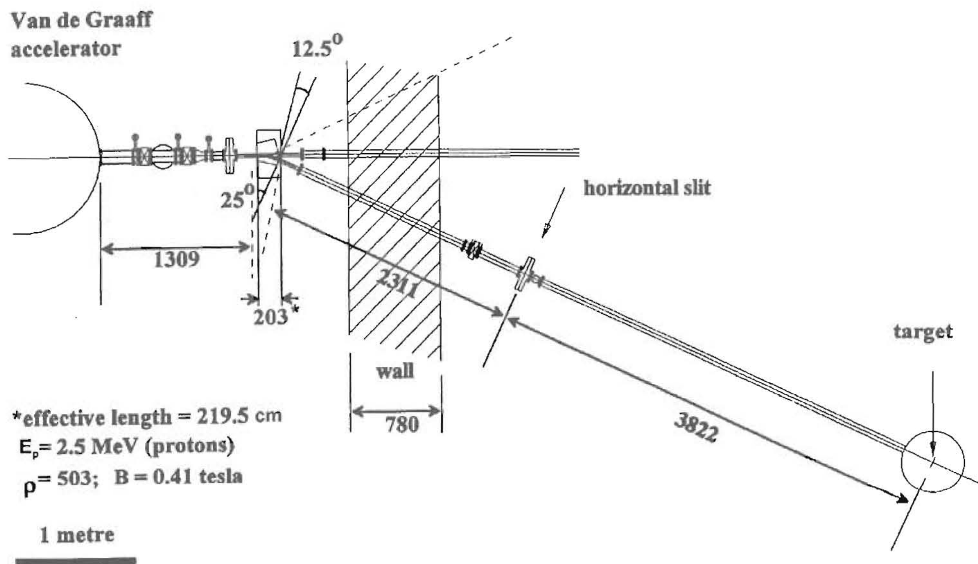

Fig. 9: Layout of the accelerator beamline in which the energy scanning system is installed.

The energy scanning system consists of two sets of electrostatic deflection plates. One set is located in front and the other one behind the switching magnet at similar, but not identical distances from the magnet. When a voltage is applied on the first set of plates the beam gets deflected from its original trajectory.

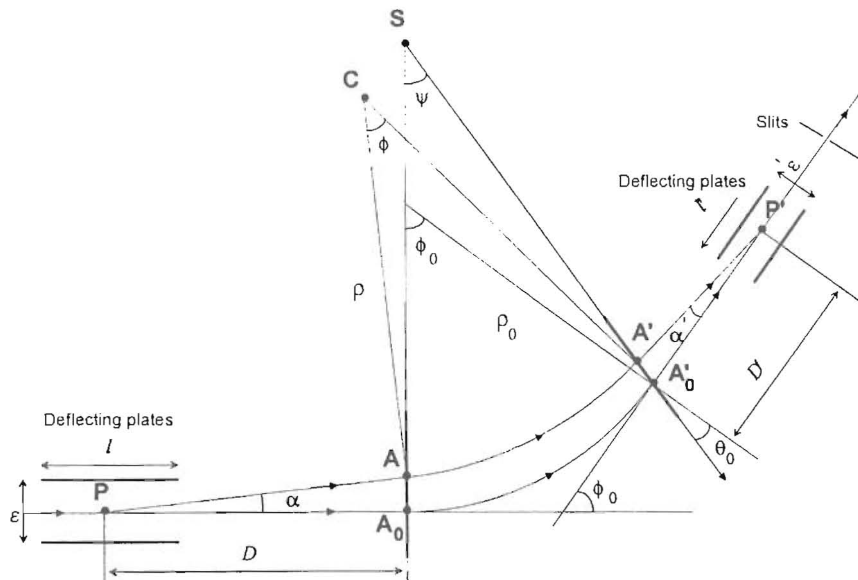

Fig.10: Schematic diagram of a set of deflection plates, together with the deflected and undeflected beam path.

The second set of deflection plates after the magnet has the opposite polarity of the first set of plates. This corrects the disturbed trajectory of the deflected particles in a way that the beam is now deflected onto the horizontal energy selection slits located downstream at the horizontal focus, which is schematically shown in Fig. 10. The feedback from the slits causes the stabilising system to increment the terminal voltage of the accelerator until the beam trajectory is passed through the slits. Detailed calculations for our system are in ref.[40].

By varying the applied voltage on the deflector plates it is easy to change the energy of the analysing ions without changing the setting of the analysing magnet. The energy variation without changing the magnetic field opens up the important possibility of running the experiment in a multi-sweep mode, since no hysteresis problems exist.

A Pentium computer controls the power supply for the deflector plates in front and behind the switching magnet. To automatically save a spectrum after a scan the PCA - Multiport can be run in a batch mode. An example for one of the batch programs, written for that purpose, is listed in Appendix A.

5.5. γ - RAY DETECTION

For the gamma ray detection from the nuclear reaction analysis two gamma detectors were used. One of the detectors is a 5.3 *cm* EG&G Ortec high-purity intrinsic germanium coaxial photon detector, the other a 5 *inch* Bicron NaI-scintillation detector.

When gamma radiation interacts with the NaI(Tl) crystal, the transmitted energy excites an iodine atom and raises it to a higher energy state. When the iodine atom returns to its ground state the energy is re-emitted in the form of a light pulse in the ultraviolet which is promptly absorbed by the thallium atom and re-emitted as fluorescent light. The efficiency of a NaI detector is high, however its resolution is relatively poor (peak width of 6 % at 1 *MeV*).

The coaxial intrinsic germanium detector consists of a cylinder of intrinsic germanium with impurity concentrations of less than 10^{10} atoms cm^{-3}. The core of this cylinder consists of doped germanium and the contact on the surface of the cylinder consists of lithium. Gamma radiation creates electron hole pairs in the active region (intrinsic germanium), and the charge

produced is collected under the influence of the bias voltage of 3000 *volts*. Germanium detectors have a resolution of about 0.15% at 1.3 *MeV*. However, due to the size of the germanium diode the counting efficiency of the germanium detector is poor. By adding the counts of both detectors (Ge and NaI) the counting efficiency was increased to reduce the analysing time to an acceptable level.

Through modified ports in the analysing chamber the two detectors could be positioned close to the target to reach a large solid angle $d\Omega \approx 10^{-1}$ *sterad* of detection. The two detectors and the incident beam are in the same horizontal plane. The angle between the beam axis and the NaI detector is $\theta_1 = 90°$ and between the Ge detector and the beam axis $\theta_2 = 127°$.

In Fig.11 a schematic drawing of the layout of the analysing detector system is shown.

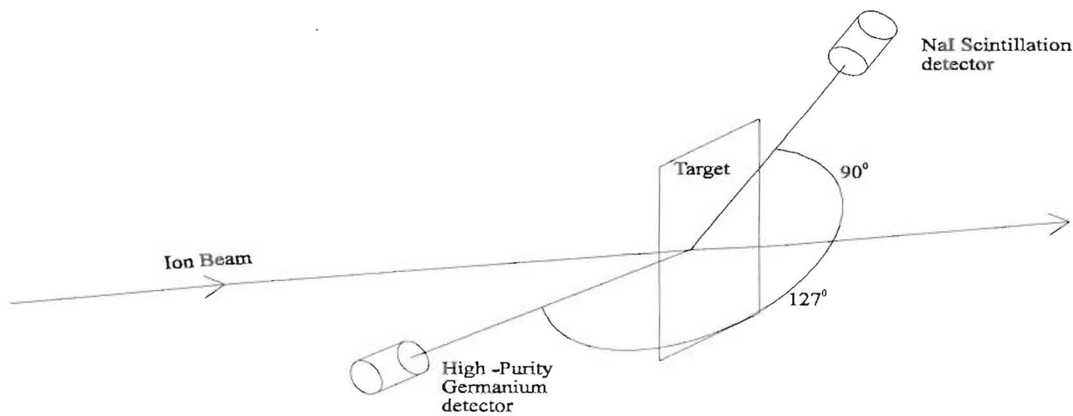

Fig.11: Detector configuration relative to the target and the incoming beam.

5.6. DATA AQUISITION

A block diagram of the electronic circuitry for data acquisition of NRA measurements is displayed in Fig.12. When a gamma ray arrives at one of the detectors the signal is amplified by a Tenelec TC243 amplifier. The output signal of each amplifier is sent to a single channel analyser (SCA). The logic output from the SCA is connected to an Ortec 433 sum-invert amplifier, which is a logic-or amplifier. The sum invert amplifier is set to non-invert, which ensures that when on either detector a gamma-ray in the desired energy window is detected a

logic pulse is given to the PCA-Multiport. This Tenelec multichannel analyser is set on multichannel scaler (MCS) mode.

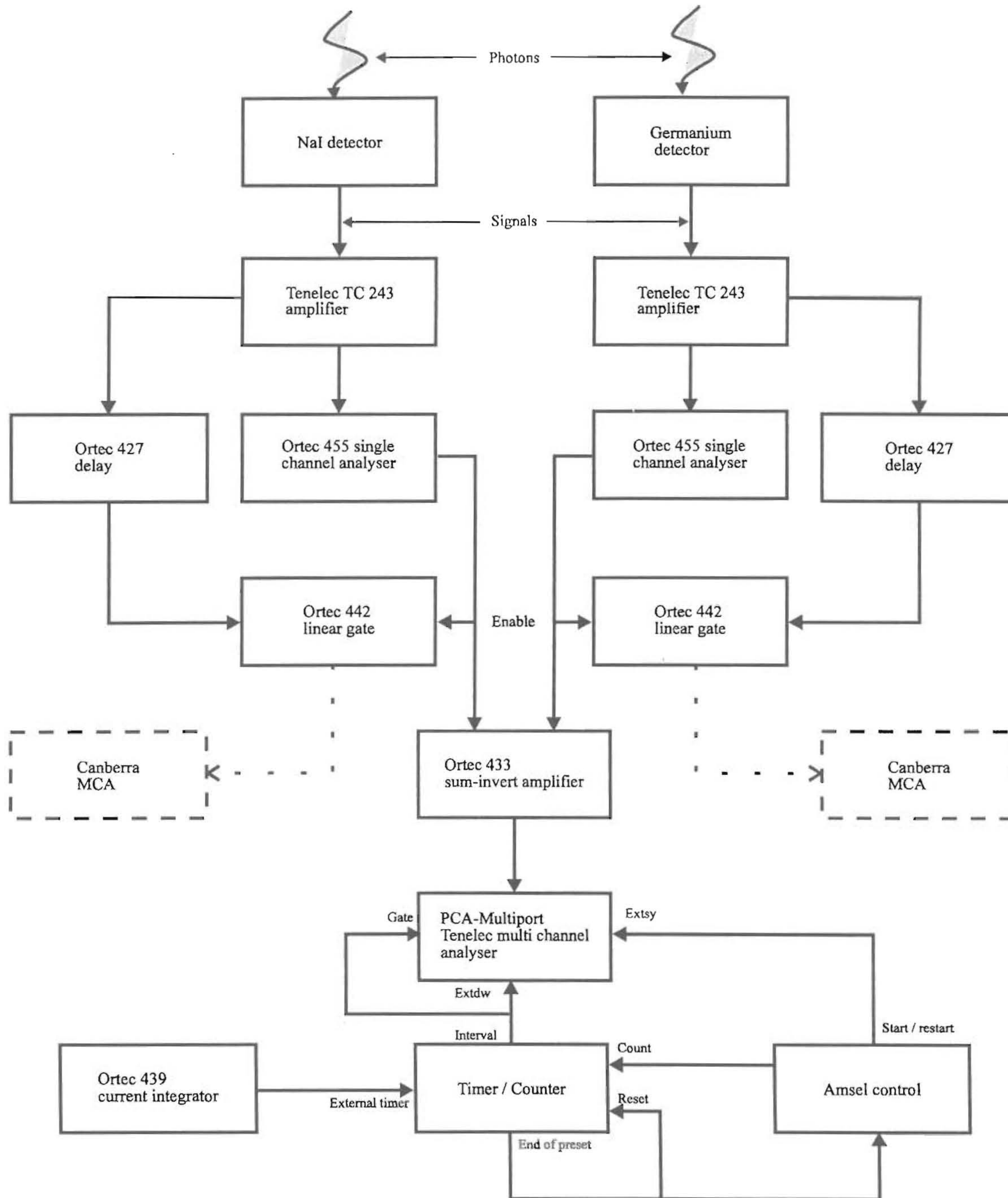

Fig.12: Block diagram of the electronic circuitry used for the NRA measurements.

5.6.1. SETTING OF ENERGY WINDOWS

Before NRA measurements are performed several adjustments and calibrations of the system have to be made. An energy window has to be set at the SCA to detect only γ-rays with energies that result from the employed nuclear reaction. The setting was performed separately for each detector with a radioactive ^{60}Co source, which has characteristic gamma rays at 1173 keV and 1332 keV. The amplified signal from the detector is send simultaneously through a Ortec 427 delay and the SCA to a linear gate. The logic signal from the SCA is connected to the gate to enable analogue pulses within the set energy window to pass to the multichannel analyser MCA (dotted line). The windows of the SCA are at this stage completely open to allow the full energy spectrum to pass and the delay is set to $\tau = 2\ \mu s$ to ensure that the signals arrive at the gate in coincidence.

Once the MCA was calibrated, the upper and lower levels of the SCA were adjusted to the desired energy window. The γ-rays from the $^{27}Al(p,\gamma)^{28}Si$ reaction have a maximum energy of 10.76 MeV (see chapter 5.7). Other γ-rays with lower energies from this reaction were not used for detection because of background problems. The energy windows were set differently for both detectors. The SCA energy window for the germanium detector was set between 10.3 MeV and 11.5 MeV and for the NaI detector an SCA energy window between 10.4 MeV and 11.4 MeV was set. The slightly smaller window for the NaJ detector was chosen because of its higher counting efficiency. With this setting of the SCA energy windows, the best signal to background ratio could be reached.

5.6.2. NRA MEASUREMENTS

The power supply for the energy scanning system (see chapter 5.4.) as well as the PCA Multiport used for the data acquisition are controlled by a Pentium - computer running the Turbo Pascal computer code AMSEL.

At the beginning of a NRA measurement the energy of the incoming proton beam is set to its starting value by the computer program, which also sets the PCA-Multiport to channel 1. After sending the starting pulse, counts from the SCA are collected into that channel until a certain predetermined charge was collected on the sample.

When the set charge is reached on the sample, the counter sends a feedback to the scanning system to increase the energy of the incoming proton beam. The counter for the integrated beam current is reset and the MCA-Multiport is set to the next channel. A start pulse results in counting gamma rays into that channel until the set charge on the sample is reached again.

This charge on the sample is measured with a counter that is connected to the digital output of the Ortec 439 current integrator. Within a measurement the value of the counter is set to a constant value to ensure that all the energy steps are performed for the same charge, e.g. the same amount of incident protons on the sample surface.

Secondary electrons of the analysing beam – target interaction are falsifying the measured beam current readout at the integrator. An aluminium plate with a hole for the analysing beam is connected to a negative potential of $U = -200\ V$ and placed about 1 *cm* before the target to suppress secondary electrons.

Up to 10 energy scans were performed for every measurement. The spectrum obtained after each scan was saved. This was done for several reasons. After about 10 scans a degradation of the surface due to the proton beam was observed. Some of the sample surfaces were flaking. Therefore the spectra taken after every scan were carefully compared to rule out flaking effects on the target surface that would influence the results.

Another reason for saving each scan was that the electricity supply for the system was not reliable. Long measurements were performed without attending to the accelerator. A power failure or a short power drop shuts down the power supply of the analysing magnet as well as the accelerator itself. However, saved spectra after a few scans contained already enough information about the depth profile.

5.6.3. MAGNET SETTING

The scanning system (see chapter 5.4.) scans the energy symmetrically about a central proton beam energy. The central energy together with the step width and the number of steps determines the proton energy region that is covered in a measurement. It is crucial for every

measurement to first calibrate the PCA – Multiport by setting the magnet correctly to the desired central energy.

For setting the analysing magnet of the accelerator a solid aluminium target was used. The spectrum was taken with the PCA-Multiport as described above. An example for such a calibration spectrum can be seen in Fig. 13. The 'step' represents the target surface, which, in the case of aluminium corresponds to incoming protons at 992 keV. The deflecting magnet was set to get this 'step' at about channel 15 of the PCA-Multiport for background corrections at lower proton energies.

The computer program was set to a proton energy step width of ΔE = 500 eV for the implanted samples, which for example corresponds to a step width in silicon of 12.2 nm. To cover the implanted depth in the sample one scan contained 80 steps. For the in-diffusion analysis the step width was set to ΔE = 250 eV which corresponds to 5.3 nm in aluminium and typically 40 steps were performed in a scan. A further description of the system can be found in [41].

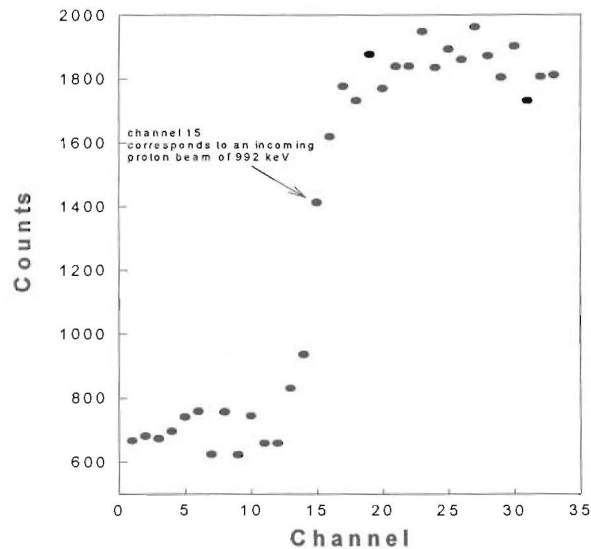

Fig. 13: Spectrum of a solid aluminium target for calibration purposes. Channel 15 corresponds to an incoming proton energy of 992 keV.

5.7. THE ^{27}AL(p,γ)^{28}SI REACTION

The reaction used for the depth profiling analysis is the ^{27}Al(p,γ)^{28}Si reaction at a proton energy of 992 keV. Aluminium has only one stable isotope: ^{27}Al which has at least 22 (p,γ)

resonances below 1 *MeV* [42]. All the resonances have a width smaller than 200 *eV*. The cross section is largest for 992 *keV* (σ = 31 *mb*) followed by 632 *keV* (σ = 5.3 *mb*).

Fig.14 shows a γ-ray spectrum of a thin aluminium sample for the 992 *keV* resonance used in this work recorded with a Ge(Li) detector [43].

The high-energy γ-rays result in three peaks each in the spectrum: full-energy peak, single-escape (*S.E.*), and double-escape (*D.E.*) peaks. The full-energy peak corresponds to the case, when the total energy of the γ-ray is absorbed in the detector. The escape peaks are observed, when one or both of the annihilation γ-rays (511 *keV*) are lost from the detector.

The decay scheme for this reaction, which has a width of ΔE_r = 105 *eV* [44], is presented in Fig.15 [45]. The excited level of silicon is at 12.542 *MeV* from where it decays by different decay modes to its ground state. The direct decay to the excited state at 1.78 *MeV*, resulting in a γ-ray with the energy 10.76 *MeV*, has with 78% the highest probability [46]. A direct transition to the ground state would be a *M3* transition and is therefore very unlikely.

One major advantage of this high γ-ray energy region is the low background yield and usually the lack of other interfering resonances of the target material. The only other possible reaction for ^{27}Al having a γ-energy within our SCA windows is for a proton energy at 632 *keV* resulting in a γ-energy at E_γ= 10.41 *MeV* with a cross section of 5.3 *mb*. However, when analysing silicon with a proton beam of 992 keV this would correspond to a depth of 9 μm in silicon whereas the aluminium is only implanted at a depth of 0.2 μm.

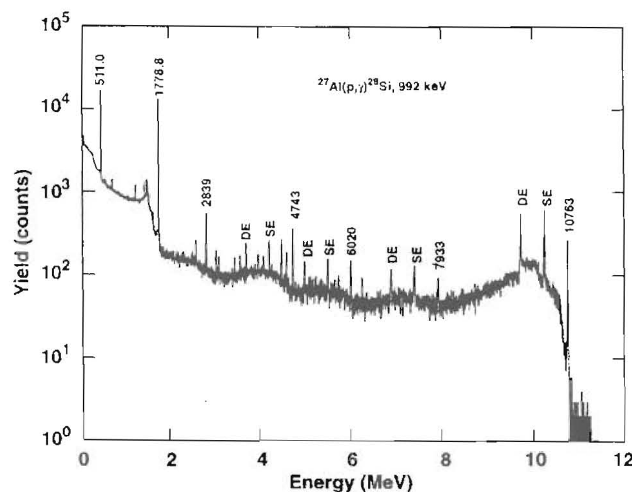

Fig.14: γ-ray spectrum for the 992 keV ^{27}Al(P,γ)^{28}Si resonance [43].

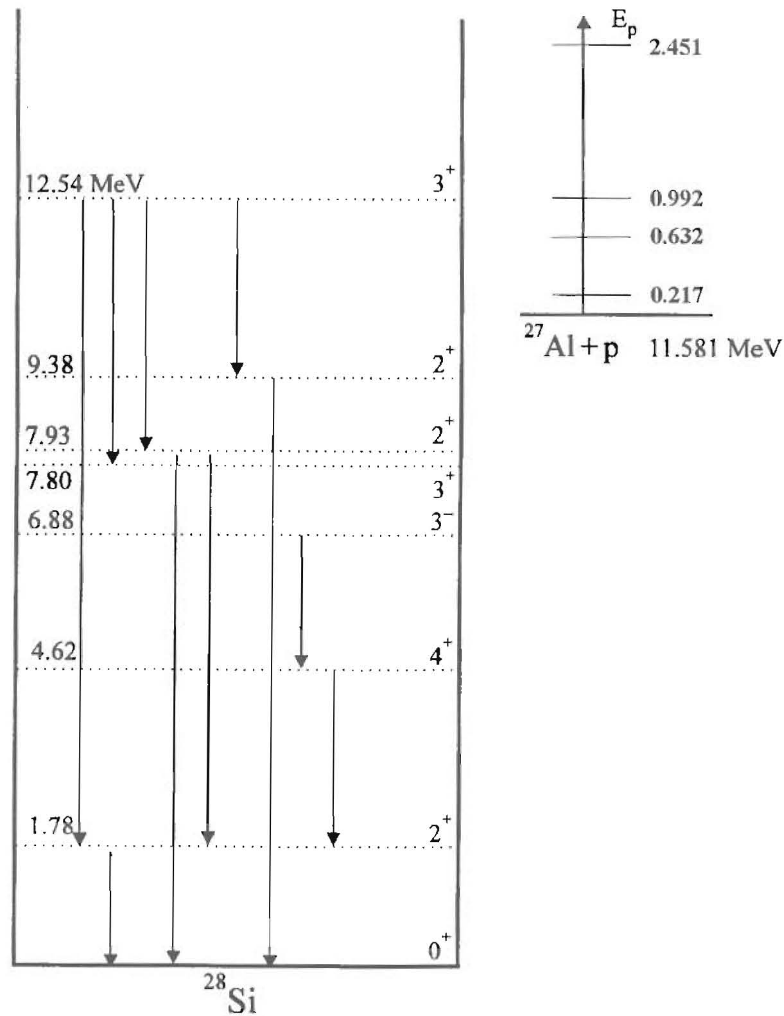

Fig.15: Decay scheme of the excited level of ^{28}Si at 12.542 *MeV* to the ground state.

5.8. CHANNELING

The steering of ions by lattice potentials in a crystal is known as channeling. Channeling of energetic ions occurs when the beam is carefully aligned with a major symmetry direction of a single crystal. A major symmetry direction is one of the open directions as viewed down a row of atoms in a single crystal. Channeled particles cannot get close enough to the atomic nuclei of the target to undergo large angle Rutherford scattering. Therefore the scattering of the substrate is drastically reduced. There is always a full interaction with the first monolayers of the solid, resulting in a surface peak in the spectrum. A schematic drawing of particle trajectories undergoing scattering at the surface and channeling within the crystal is shown in Fig. 16.

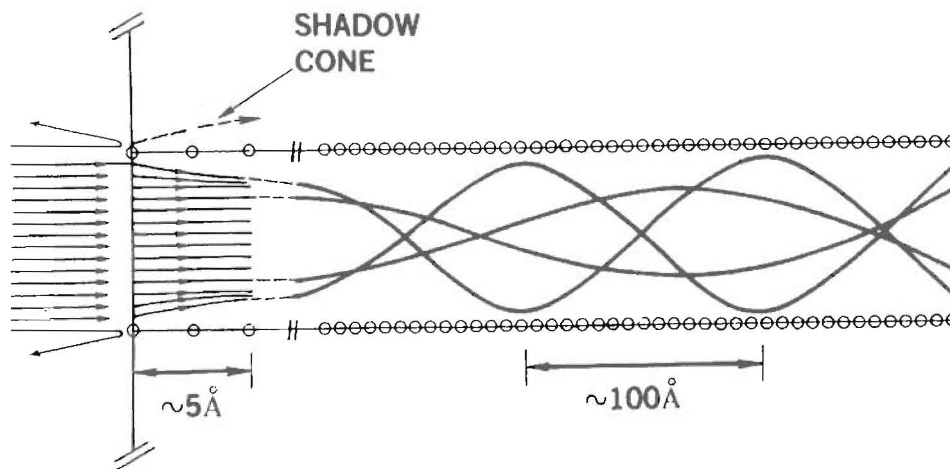

Fig. 16: Schematic of particle trajectories undergoing scattering at the surface and channeling within the crystal. The depth scale is compressed relative to the width of the channel in order to display the trajectories[47].

The trajectory of a channeled ion is such that the ion makes a glancing angle impact with the lattice axes (axial channeling) or planes (planar channeling). Detailed descriptions of the channeling effects as well as for its different applications are in refs. [48-52].

The channeling effect can be used for analysing crystal properties like for example the lattice site occupation of impurity atoms [53] or investigation of the crystalinity of a material. For this work the major interest was in analysing the damage introduced into the semiconductors during the aluminium implantation as well as how the crystal structure recovered during the different annealing steps. Having a disturbed lattice due to point or extended defects results in an increase in the backscattering yield of an orientated (aligned) crystal. Comparing an aligned backscattering spectrum of an unimplanted crystal with the aligned spectrum of an implanted crystal indicates the radiation induced damage introduced into the lattice during the implantation.

The channels from the backscattering spectra were converted to a depth scale by assuming an energy loss as found for an amorphous solid.

The channeling experiments were performed with the Van de Graaff accelerator at the University of Pretoria using 1.5 MeV α particles. The semiconductor samples were mounted on a three axis goniometer with an angular precision better than 0.1°. The silicon surface barrier detector was mounted at a backscattering angle of 165°.

5.9. ERROR CALCULATIONS

The given errors for the range distribution and the second moments are calculated from several experimental uncertainties. The total error in the first moment is calculated by taking the following factors into account:

- statistical uncertainty of the maximum
- $\approx$ 5 % uncertainty in the tabulated values given for stopping
- uncertainty of the surface

The squares of these uncertainties were added to obtain the square of the total experimental error in the first range moment.

The total error from the second range moment was calculated from:

- statistical uncertainties
- $\approx$ 5 % uncertainty from stopping values, taking only into account the width of the curve.

The uncertainty of the surface channel is not important for the second moment. The squares of the given uncertainties add up to the square of the total error in the second range moment.

5.10. DIFFUSION ANALYSIS

The diffusion coefficients were obtained with the finite difference method using the computer code DIFFUS as described in chapter 2.4. by comparing the NRA depth profiles before and after annealing.

The sensitivity of the applied method to determine diffusion coefficients depends on several experimental parameters. High enough count rates in an energy scan are essential to reduce experimental errors in the obtained range parameters. Small energy step widths of the analysing beam increase the depth resolution. However, for smaller energy steps the total analysing time increases for a sufficient count rate, which can lead to a degradation of the

target surface by the analysing beam already after a few energy scans. For best results the parameters were adjusted to the values mentioned in chapter 5.6.3.

The lower detection limit of diffusion coefficients can be estimated by taking depth distributions of an implanted sample where no detectable diffusion occurred. Experimental uncertainties for the full width at half maximum (FWHM) of the depth distribution are typically about $\Delta x \approx 5$ *nm* for at typical FWHM of 150 to 200 *nm*.

From the change in FWHM of a gaussian depth distribution the diffusion coefficient is calculated to $W^2 = 4\ Dt\ \ln(2) + W_0^2$ [54], where W_0 and W are the widths before and after diffusion, respectively. The total uncertainty Δx_{tot} in the width for an initial and final distribution calculates to: $(\Delta x_{\mathrm{tot}}) = [(\Delta x_{\mathrm{i}})^2 + (\Delta x_{\mathrm{f}})^2]^{1/2} \approx 7 \times 10^{-7}\ cm$. For an annealing time of 1 hour an upper limit for diffusion coefficients of implanted samples are calculated to: $D_{\mathrm{min}} \approx 10^{-15}\ cm^2\ s^{-1}$.

Smaller FWHM of 10-20 *nm* and experimental uncertainties of about $\Delta x = 3$ *nm* in the determination of the FWHM of the thin films are due to smaller energy steps and higher count rates. Total uncertainties in the FWHM are in the range of $\Delta x_{\mathrm{tot}} \approx 4$ *nm*, which leads to a minimum detection limit for the diffusion coefficient of $D \leq 10^{-16}\ cm^2\ s^{-1}$.

CHAPTER 6

PREVIOUSLY PUBLISHED RESULTS

Over the last 100 years many investigations were done on diffusion in solids to understand the mechanisms that are involved in this process. Specialised conferences on diffusion were held for researchers to exchange their latest knowledge (for example: Diffusion in Materials 'DIMAT 96').

For this study the diffusion behaviour of aluminium in five different semiconductors was investigated. The investigated semiconductors can be summarised in two groups: elemental semiconductors (silicon and germanium) and *III-V* compound semiconductors (gallium arsenide, indium phosphide and indium antimonide).

Publications of the investigated systems are mentioned in this review as well as work on related or similar systems. Aluminium diffusion coefficients in indium phosphide and indium antimonide were not found in the literature.

6.1. ELEMENTAL SEMICONDUCTORS

An important summary on diffusion in silicon and germanium is a review article by *Seeger* and *Chik* [8]. Although this article was written in 1968 the major diffusion mechanisms and self-diffusion coefficients in these semiconductors are discussed. An extensive reference list concludes this review. The diffusion mechanisms mentioned in this review are discussed in chapter 2.2.1.

Recent research was done on implantation of impurities (dopants) followed by successive annealing to diffuse them onto a desired lattice site for electrical activation.

6.1.1. SILICON

A large amount of publications in the past 20 years is dealing with aluminium in silicon. This list can only give an overview and cannot claim to be complete.

The aluminium-silicon system is a simple eutectic system with two solid solution phases, fcc (aluminium) and diamond cubic (silicon) [55]. The maximum solubility of silicon in aluminium is found to be 1.5 ± 0.1 at.% at the eutectic temperature, and decreases to 0.05 at.% at 300 °C. The maximum solubility of aluminium in silicon is only 0.016 ± 0.003 at.% at 1190 °C, the retrograde point of the silicon solidus. Aluminium - silicon alloys have not been reported to form metastable intermetallic compounds or glassy alloys.

Some of the results on aluminium diffusion in silicon are summarised in ref. [56] including a list of diffusion coefficients and their references. The interest of aluminium as an impurity arises from the fact that it diffuses faster than other group *III* acceptors.

The diffusion coefficients found were subject to controversy because differences of up to two orders of magnitude were found.

D_0 [$cm^2\,s^{-1}$]	E_A [eV]	D (900 °C) [$10^{-15}\,cm^2\,s^{-1}$]	References
8	3.47	9.64	*Fuller, Ditzenberger* [57]
2800	3.9	128	*Goldstein* [58]
4.8	3.36	17.2	*Miller, Savage* [59]
0.5	3.0	63.2	*Kao* [60]
1.38	3.41	3.01	*Ghoshtagore* [61]
1.8	3.2	31.4	*Rosnowski* [62]
8.88	3.44	14.4	*Galvagno* [63]
7.40	3.42	15	*La Ferla* [64]

Table 2: Pre-exponential factors and activation energies in $D = D_0 \exp(-E_A / kT)$ quoted by different authors. The diffusion constant at 900 °C is given for the purpose of comparison.

The differences seen in table 2 are largely due to the nature of the impurity sources and diffusion conditions. In ref. [57] aluminium metal in an evacuated tube was used to deposit a film of aluminium onto silicon. The diffusion coefficient was measured using the *p-n*-junction method (see chapter 2.3). The lowest annealing temperature was 1085 °C for 234

hours. In ref. [58] an aluminium - silicon alloy button was placed on top of the silicon substrate within an evacuated tube. In ref. [59] the substrate and source were placed inside a silicon boat held within a tantalum tube which acted as a getter to avoid any reaction between the quartz tube and the substrate. This assembly was heated in an open arrangement under helium or argon gas flow. *Ghoshtagore* [61] diffused aluminium into Si <111> from doped epitaxially deposited source layers in a floating hydrogen atmosphere. The temperature dependence of the intrinsic diffusion coefficient was obtained above 1120 °C. *Rosnowski* [62] uses a high vacuum, open tube method for aluminium diffusion into silicon. The diffusion coefficient was determined in the temperature range 1025 –1175 °C.

Galvagno et al. [63] implanted a low dose (1 x 10^{14} cm^{-2}) aluminium ions at 80 *keV*, 300 *keV* and 6 *MeV*. The annealing temperature range was from 1000 °C - 1290 °C using rapid thermal processes in a nitrogen atmosphere for a few seconds and in a SiC tube furnace for longer times up to 16 hours. The depth profiles were obtained using SIMS. The aluminium dose lost through the surface was taken into account. It was concluded that SiO_2 is not a suitable capping layer to prevent loss of aluminium due to the reaction of aluminium with oxygen to form Al_2O_3. Aluminium arriving at the SiO_2 / Si interface is lost in Al_2O_3 precipitates and the range of aluminium in silicon is shifted towards the silicon surface.

To avoid surface effects aluminium was implanted with 100 *MeV* into CZ and FZ silicon substrates [64]. The natural oxygen content in CZ and FZ silicon was determined to be $\approx 10^{16}$ cm^{-3} and $\approx 10^{17}$ cm^{-3}, respectively The annealing temperature was 1200 °C at different annealing times. SIMS analysis apparently revealed a multipeak structure of O and Al around the projected range of Al. The results imply that the Al-O complex formation is enhanced by the presence of oxygen but that it is catalysed by the damage created during the implantation.

Bruesch et al. [76] implanted 3 x 10^{15} aluminium ions cm^{-2} at an energy of 150 *keV*. A maximum concentration at 218 *nm* with a range straggling value of 69 *nm*, determined with SIMS was obtained after implantation. The out-diffusion after annealing was determined. It was found that only 8% of the aluminium atoms remain in the sample. The rest (92%) was lost by out-diffusion. Annealing temperatures were 1060 °C for 10 min (rapid thermal annealing - *RTA*) in vacuum. The formation of Al_2O_3 precipitates was observed at a depth of 350 *nm* after annealing. This depth corresponds to the position of the interface between

damaged and undamaged region in the crystal. The oxygen for the formation of complexes is either present in the wafer or is coming from the residual gas. The precipitates consist of platelets lying on a well-defined lattice plane. Two types with orientation 90° to each other lying in the (110) plane are observed. A second row of small precipitates was observed in some areas of the specimen at a depth of 230 nm. These precipitates reveal no crystalline structure and are less than 6 nm in diameter. Their structure could not be clearly analysed. The determined aluminium diffusion constant D at 1333 K ranges between 1.7 x 10^{-13} and 1.6 x 10^{-11} $cm^2\ s^{-1}$, which is close to the value D = 1.2 x 10^{-11} $cm^2\ s^{-1}$ measured by Goldstein [58] at this temperature.

Annealing temperatures ≥ 1200 °C of aluminium implanted (FZ) Si <111> were used to investigate aluminium precipitates [66]. For this study 1 x 10^{15} aluminium ions cm^{-2} were implanted at an energy of 150 *keV*. Annealing took place in nitrogen atmosphere. Different capping layers were applied to prevent the loss of aluminium atoms. The observed precipitates were found to have a crystalline structure after annealing.

Ref. [67] reports on 3 x 10^{15} aluminium ions cm^{-2} that were implanted at an energy of 60 *keV*. Back-diffusion by using different capping layers was investigated. Annealing temperatures were 900 - 1250 °C for 1 hour and up to 16 hours in a nitrogen ambient. It was found that aluminium precipitates may be formed at temperatures as low as 350 °C in the damaged region induced by aluminium implantation. These precipitates are stable below 900 °C.

The latest study on this system was done by *Kuhlmann* et al. [68] (see figure 17). The diffusion of aluminium in silicon and its interaction with phosphorus and boron has been investigated. The aluminium predeposition was carried out in vacuum using a silicon sandwich structure consisting of a silicon-target wafer and a source wafer, which was covered by a 300 *nm* aluminium film. Additional results for the aluminium in-diffusion were obtained by annealing predeposited samples without the diffusion source (drive-in). The depth profiles before and after RTA (rapid thermal annealing) were characterised by SIMS. Additionally a big change in the aluminium diffusion behaviour in the presence of boron or phosphorus was observed. A supersaturation of self-interstitials caused by a high surface concentration of boron or phosphorus leads to an accelerated aluminium diffusion in Si <111>. The authors assume that aluminium migrates as a negative ion in silicon and that it uses self-interstitials as

diffusion vehicles. The annealing temperatures used were, like in most of the other reported results, higher than 1000 °C.

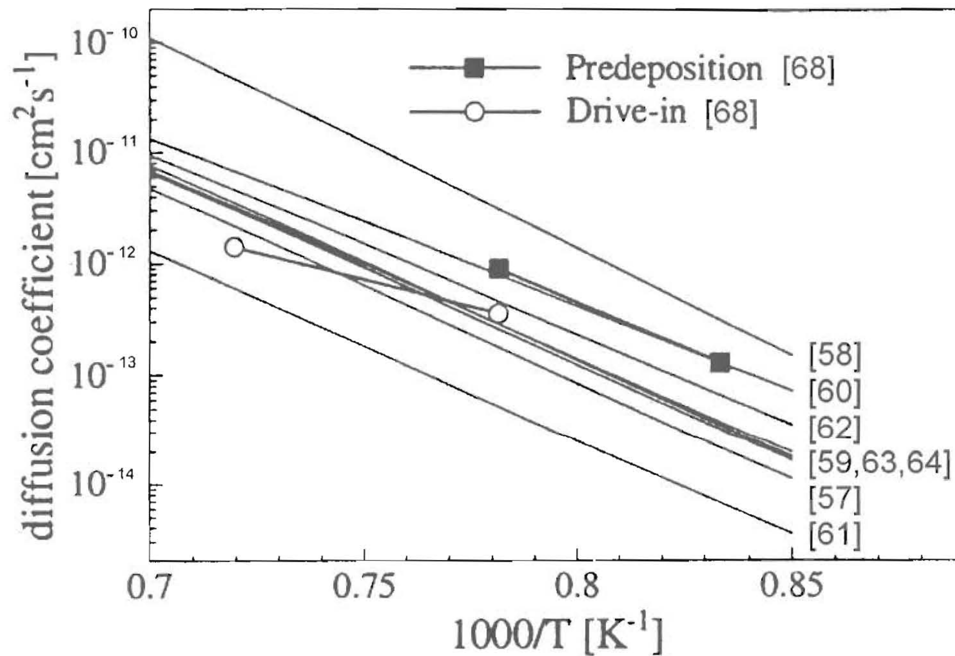

Fig.17: Diffusion coefficients of aluminium with bibliographical reference [68].

Recent publications dealing with aluminium implantations at elevated substrate temperatures were not found. The only previously reported work [69] of aluminium implanted into heated FZ – Si <111> substrates to avoid radiation defects dates back to 1969. Out-diffusion was observed after annealing the room temperature implanted samples, however an explicit analysis for diffusion coefficients was not performed.

A wide spread of the published results over the past years is evident. An extrapolation of the reported data in table 2 and fig. 17 results in an expected diffusion coefficient between 3 x 10^{-15} cm^2 s^{-1} and 1.3 x 10^{-13} cm^2 s^{-1} for T_a = 900 °C. An average of D_0 = 354 cm^2 s^{-1} is calculated for the pre-exponential factor with an average activation energy of E_A = 3.4 eV. The average diffusion coefficient at 900 °C is calculated to be D = 4 x 10^{-14} cm^2 s^{-1}. The main reasons for this spread over two orders of magnitude are different analysing methods and different diffusant sources as well as other factors like point or extended defects. All the reported results were done on only one diffusant source.

For an annealing temperature of T_a = 900 °C the previously reported results are in the detection range of our method. Therefore, investigations on different diffusant sources as well as radiation induced lattice defects and their influence on the diffusion coefficient were done in this work and compared with previously reported results.

6.1.2. GERMANIUM

The maximum solubility of aluminium in germanium is 1.09 at.% at an eutectic temperature of about 420 °C [70].

In *Seeger* and *Chik*'s review in 1968 [8] on diffusion of different elements in germanium and silicon no values for diffusion coefficients of aluminium in germanium were listed.

The diffusion coefficient of aluminium in germanium was reported by ref. [71]. Thin aluminium layers (5-28 *nm*) were deposited onto clean germanium crystals. Samples were annealed in vacuum from 827 *K* up to 1178 *K* and the diffusion behaviour was analysed with SIMS. An activation energy $E_A = 3.45 \pm 0.04$ *eV* and a pre-exponential factor $D_0 = (1.0 \pm 0.5) \times 10^3$ $cm^2\ s^{-1}$ was obtained for the diffusion coefficient of aluminium in germanium.

The only other work on this system was reported in 1967 by ref. [72] who used sheet resistance measurements. Annealing temperatures ranged from 1023 K up to 1123 K and resulted in an activation energy of $E_A = 3.24$ *eV* and a pre-exponential factor $D_0 = 160\ cm^2\ s^{-1}$.

The reported results on aluminium diffusion in germanium by *Dorner* [71] and *Meer* [72] calculate to $D_{[71]} = 1.1 \times 10^{-15}\ cm^2\ s^{-1}$ and $D_{[72]} = 2.2 \times 10^{-15}\ cm^2\ s^{-1}$ at a temperature of T_a = 700 °C and to $D_{[71]} = 3 \times 10^{-20}\ cm^2\ s^{-1}$ and $D_{[72]} = 1 \times 10^{-19}\ cm^2\ s^{-1}$ at a temperature of T_a = 500 °C.

The previously reported diffusion coefficients at T = 700 °C vary by a factor of two. They are in the range that can be detected with our method. Therefore, the measurements performed in this work are to verify which of the two reported results can be relied on at T_a = 700 °C.

6.2. COMPOUND SEMICONDUCTORS

The compound semiconductors in this work gallium arsenide, indium phosphide and indium antimonide are all combinations of group *III* elements with group *V* elements. These *III-V* semiconductors have the zincblende crystal structure, in which each group *III* atom has four group *V* atoms as nearest neighbours, and vice versa. Most of the *III-V* semiconductors can be produced as large bulk crystals, but only gallium arsenide and indium phosphide are currently made in larger quantities. The two major methods of growth are the horizontal Bridgeman and the Czochralski techniques.
Impurity diffusion analysis in compound semiconductors is more complicated than in elemental semiconductors because of the fact that three elements have to be considered. The impurity could occupy a substitutional site of the group *III* element or of the group *V* element.

A basic review on ion implantation applied in *III-V* semiconductors is summarised in ref. [19], however, without including aluminium ions. The introduced damage during implantation and annealing methods in indium phosphide, gallium arsenide and some other compounds (not indium antimonide) is discussed there.

Because of the zincblende structure six different single point defects have to be considered in *III-V* compounds: vacancies in the group *III* – sub-sublattice, vacancies in the group *V* - sub-lattice, group *III* - self-interstitials, group *V* - self-interstitials and antisite defects e.g. group *III* atoms on group *V* sites or of group *V* atoms on group *III* sites.

6.2.1. GALLIUM ARSENIDE

A review of recent developments in the understanding of self- and impurity diffusion processes in gallium arsenide can be found in ref. [73]. For a consistent description of the diffusion processes involved in gallium arsenide one has to know the intrinsic point defects involved in the diffusion in both sublattices. Fig. 18 summarises the results from this review with a list of the different authors and years.

Aluminium is a group *III* element and can therefore also be used with other group *V* elements to form a *III-V* compound semiconductors. As all *III – V* semiconductors have a zincblende

structure the possibility of epitaxial growth of one compound onto another arises. The difficulty here is the different lattice constant. However, some compounds are compatible for this procedure like for example gallium arsenide and aluminium arsenide. Inter-diffusion between gallium arsenide and aluminium arsenide, more precisely, the inter-diffusion between gallium and aluminium was studied by *Chang* and *Koma* [74]. The objects of their study were multilayer heterostructures of the type GaAs - AlAs - GaAs or $Al_xGa_{1-x}As$ - $Al_xGa_{1-x}As$ - ...... ($0 \leq x \leq 1$)grown by molecular beam epitaxy (*MBE*). The thickness and composition of each layer was monitored. The gallium arsenide and aluminium arsenide layers had identical thicknesses of about 0.155 μm. The diffusion anneal was carried out in the temperature range 850 - 1100 °C in vacuum with an arsenic source in the ampoule to provide an overpressure for the protection of the sample surface. Depth and composition profiles after annealing were obtained with Auger-electron spectroscopy (AES). The diffusion coefficient obtained can be empirically represented by a single modified Arrhenius expression, $D(x,T) = D_0 . \exp(-E_A(x) / kT)$, where the pre-exponential factor is given by $D_0(x)=92 \exp(-8.2x)$ (in $cm^2\ s^{-1}$) and the activation energy of diffusion $E_A(x)=4.3-0.7x$ (in eV). The Al-Ga inter-diffusion data approximate those for Ga self-diffusion closely, because the Al diffusivity in GaAs is very close to that of Ga. Therefore symbols for Ga-Al interdiffusion and for Ga self-diffusion D_{Ga} are used interchangeably.

Schlesinger and *Kuech* [75] have employed photoluminescence spectroscopy to determine the temperature dependence of the interdiffusion coefficient of aluminium and gallium in $GaAs/Al_{0.3}Ga_{0.7}As$ quantum wells. Structures were grown consisting of alternating layers with a thickness of GaAs in the range of 20-150 Å, while the two cladding layers of $Al_{0.3}Ga_{0.7}As$ were 500 Å. The slices were subjected to heat treatments over a temperature range of 650 - 910 °C for times between one and six hours. The results obtained for interdiffusion coefficients between aluminium and gallium were an activation energy $E_A \approx 6\ eV$ and a value for $D = 4 \times 10^{-19}\ cm^2\ s^{-1}$ at 850 °C which results in a pre-exponential factor of $D_0 = 3.2 \times 10^8\ cm^2\ s^{-1}$.

UNIVERSITEIT VAN PRETORIA
UNIVERSITY OF PRETORIA
YUNIBESITHI YA PRETORIA

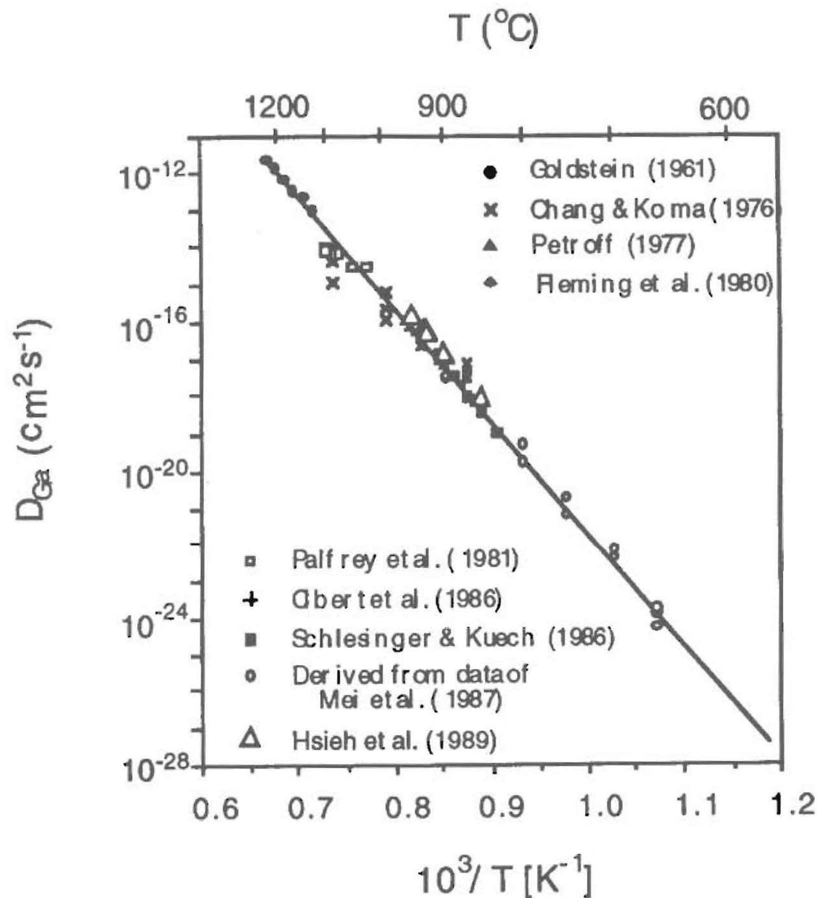

Fig.18: Self diffusion data of gallium and interdiffusion data of gallium / aluminium (open circles) in gallium arsenide as a function of reciprocal temperature [73].

Mei et al. [76] analysed the superlattice mixing of AlAs-GaAs as a function of silicon concentration. Silicon, introduced by MBE, was found to enhance the usually small diffusion coefficients of aluminium in gallium arsenide. Thermal anneals were performed in the temperature range 500-900 °C. An activation energy for aluminium diffusion in gallium arsenide of $E_A \approx 4\ eV$ was extracted. It was also found that the diffusion coefficient of aluminium was increased with increasing silicon doping concentration. The value for the activation energy of $E_A \approx 4\ eV$ in the temperature range between 800 and 1225 °C was confirmed by *Wang* et al. in ref. [77] by investigating the self-diffusion coefficient of gallium in gallium arsenide.

Goldstein [78] in 1961 was one of the first to analyse self diffusion in gallium arsenide using radio tracers. His results for the activation energy were E_A = 5.6 eV and for the pre-exponential factor $D_0 = 1 \times 10^7\ cm^2\ s^{-1}$.

Petroff [79] analysed the interdiffusion at GaAs / AlAs interfaces using transmission electron microscopy (TEM). The resulting interdiffusion coefficient D for aluminium and gallium at a temperature T = 850 °C is $5 \times 10^{-19} \leq D \leq 8.9 \times 10^{-19}\ cm^2\ s^{-1}$ without determining the activation energy E_A or the pre-exponential factor D_0.

Fleming et al. [80] studied the interdiffusion of aluminium and gallium in superlattices with X-ray diffraction analysis. The average diffusion coefficient for gallium and aluminium interdiffusion at 800 °C was reported to be $D = 5.3 \times 10^{-21}\ cm^2\ s^{-1}$ without determining the activation energy E_A or the pre-exponential factor D_0.

Palfrey et al. [81] studied the self-diffusion of gallium in gallium arsenide in the temperature range 1100 - 1025 °C using radiotracer techniques. An activation energy in the order of E_A = 2.6 ± 0.5 eV and a pre-exponential factor of $D_0 = 4 \times 10^{-5} \pm 16 \times 10^{-5}\ cm^2\ s^{-1}$ were obtained. Diffusion coefficients in the above mentioned temperature range were from $D = 3 \times 10^{-15}\ cm^2\ s^{-1}$ to $9 \times 10^{-15}\ cm^2\ s^{-1}$.

A review on point defects, diffusion mechanisms and superlattice disordering in gallium arsenide based materials is summarised by ref. [82]. To determine the diffusion mechanisms in gallium arsenide and related materials, experimental results must be interpreted in association with the effects of (1) doping, (2) the group V vapour pressure and (3) point defect non-equilibrium concentrations, which may be induced by a chemical or a physical process. Gallium self-diffusion and gallium - aluminium inter-diffusion under intrinsic conditions are governed by the triply negatively charged group III sublattice vacancies V_{Ga}^{3-}. The layer disordering reaction proceeds via gallium - aluminium interdiffusion, which is immeasurable at 600 °C.

All the above-described results are consistent. A diffusion coefficient of $D \approx 10^{-30}\ cm^2\ s^{-1}$ is expected for an annealing temperature at T_a = 500 °C which is much lower than our detection

limit. However, a huge influence of radiation induced defects on the diffusion behaviour was observed after high dose implantation into elemental semiconductors. It is of interest to investigate if such an influence on the diffusion coefficient can be observed in gallium arsenide e.g. if a detectable aluminium diffusion after annealing occurs in samples that were implanted at *RT* and at T_i = 250 °C at a high dose. The obtained diffusion results are compared with those obtained for the in-diffusion analysis.

6.2.2. INDIUM PHOSPHIDE

Aluminium diffusion coefficients as well as implantation of aluminium in indium phosphide were not found in previously reported results. Other isoelectronic impurities, e.g. impurities with the same electron shell configuration as indium or phosphorous (boron, nitrogen, phosphorous, arsenic, antimony and bismuth) were implanted in InP [83], however, without reporting diffusion coefficients.

The scope of this work is the investigation of the diffusion behaviour of aluminium in indium phosphide for temperatures up to T_a = 400 °C by NRA. Higher annealing temperatures were not applied to avoid surface oxidation, e.g. formation of In_2O_3, which was even observed in a N_2 ambient after annealing at T_a = 450 °C [84]. The diffusion sources in this work were deposited aluminium layers and aluminium implanted at *RT* and at 250 °C.

6.2.3.INDIUM ANTIMONIDE

Aluminium implantations as well as the diffusion coefficients of aluminium in indium antimonide were not found in previously reported results. Therefore these measurements were performed to investigate the diffusion behaviour of aluminium in indium antimonide.

Bulk indium antimonide is a well-established material for high quality thermal imaging in the 3-5 μm wavelength range. With the lowest band gap (E_g = 0.16 *eV* at *T* = 300 *K*) of any binary *III-V* semiconductor material, it exhibits a very low electron effective mass and high mobility [85].

The surface of an implanted indium antimonide is chemically very active. Oxide films form when exposed to atmosphere after high dose implantations of heavy ions [86]. Irradiation damage was investigated by nitrogen implantation at an energy of 150 keV [87]. During the irradiation the crystal structure was monitored with channeling methods. An irreversible degradation of the single-crystal properties in indium antimonide was observed for doses that exceeded (3-5) x 10^{15} ions cm^{-2}.

Another problem is the swelling of ion implanted indium antimonide, which was investigated by ref. [88]. Phosphorus, arsenic and nitrogen were implanted at different energies and different doses into indium antimonide that was partly masked. The swelling of the substrate between the masked and unmasked area was dependent on the implanted dose and was only observed for ions heavier than mass $m \approx 12$. The swelling of the surface reaches saturation at about 1 μm and is due to voids in the substrate that are formed during the thermal spike phase of the collision cascade. A discolouring of the indium antimonide surface was also observed after implantation. The surface was black after P_4^+, As_4^+ and N_2^+ implantations and grey in other cases. The visual appearance did not change after the N^+ implantation. However, no explanation for the discolouring of the sample surface was offered.

CHAPTER 7

RESULTS AND DISCUSSION

Our experimental results on aluminium diffusion in the elemental semiconductors silicon and germanium, as well as in the compound semiconductors gallium arsenide, indium phosphide and indium antimonide are discussed in this chapter.

For the in-diffusion investigation thin aluminium films were deposited onto the cleaned semiconductor surfaces and isochronally annealed at elevated temperatures. Thin films are commonly used as diffusion sources. However, this method has the disadvantage that a thin native oxide layer can build up instantaneously after cleaning the semiconductor before depositing the aluminium film. Such an oxide layer at the interface between the semiconductor and the thin film creates a diffusion barrier, which reduces the in-diffusion.

Additional measurements were made for comparison of the results, where the diffusion source was introduced into the semiconductors by ion implantation. Here the diffusion source is directly in contact with the investigated material. However, implantations at room temperature create point and extended defects that can also influence the diffusion behaviour dramatically. By implanting the diffusant at elevated temperatures such radiation-induced defects can largely be avoided.

All three methods described were applied on every semiconductor in this study.

7.1. SILICON

Many research results on aluminium diffusion in silicon were reported in recent years. However, the obtained diffusion coefficients were spread over a wide range. This study was performed to investigate the diffusion behaviour up to 900 °C. After annealing a sample with an aluminium film at 1000 °C complete surface oxidation was observed despite a vacuum better than 10^{-7} mbar during annealing. In order to compare results from all three methods annealing temperatures were kept below $T_a \leq 900$ °C.

Our results are compared with coefficients obtained after extrapolating previously reported results to this temperature (see chapter 6.1.).

7.1.1. ALUMINIUM DIFFUSION INTO SILICON

The aluminium diffusion into Si <100> at temperatures up to 900 °C was investigated. An aluminium film of 20 ± 3 *nm* thickness was deposited onto a cleaned Si <100> wafer surface. Samples from this wafer were analysed before and after different annealing cycles.

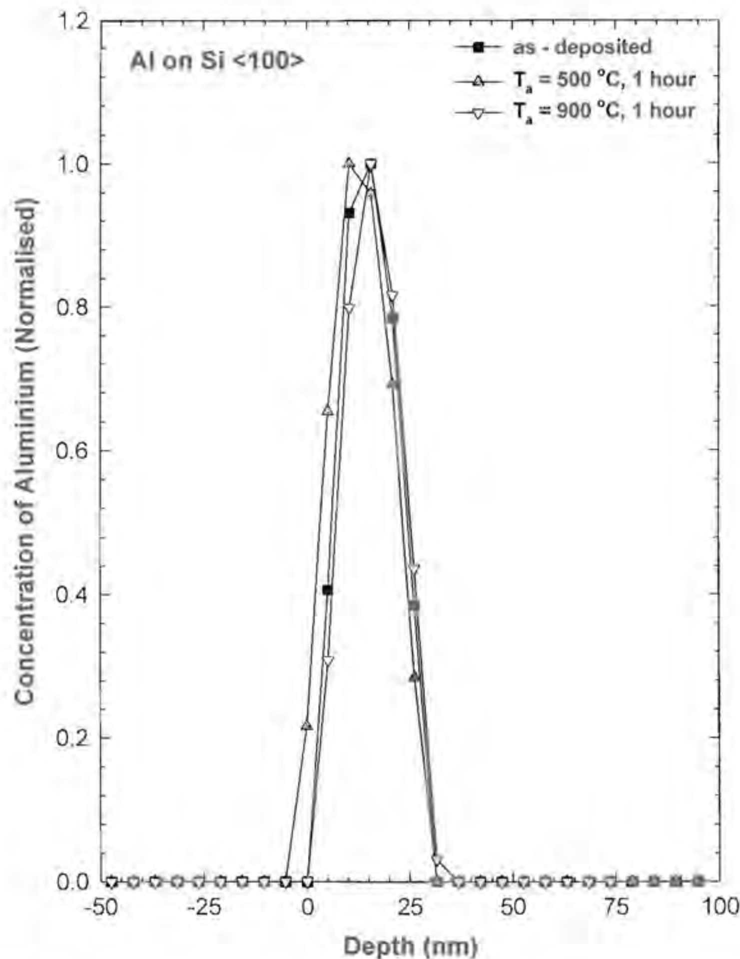

Fig. 19: Depth profiles of a vapour deposited aluminium film on Si <100> before and after annealing for one hour at different temperatures T_a.

The depth profiles of the deposited aluminium film before and after annealing for one hour at T_a = 500 and 900 °C respectively are shown in Fig. 19. The depth profiles, obtained with NRA, were corrected for proton straggling and energy resolution. A difference in the film thickness at the detection limit for our method at $\Delta d \approx 4$ *nm* was observed for T_a = 500 °C,

which is probably due to slight inhomogeneities when vapour depositing the aluminium film laterally onto the silicon wafer. However, it must be stressed that the film thickness does not contain information about in-diffusion.

If a detectable aluminium in-diffusion had occurred after annealing, the width of the interface between the aluminium film and the silicon substrate would increase. The interface width did not change within our detection limit and remained at 10 ± 4 *nm* before and after annealing at $T_a = 900$ °C. The aluminium in-diffusion at this temperature is below the detection limit for the applied method. An upper limit for the diffusion coefficient at $D \leq 10^{-16}$ $cm^2\ s^{-1}$ for 900 °C was extracted from these results.

The data reported by other workers, which were obtained applying different techniques and at higher annealing temperatures were summarised in Fig. 17 and table 2 (page 47). An extrapolation of these data to 900 °C results in a diffusion coefficient between $D = 1.3 \times 10^{-13}$ $cm^2\ s^{-1}$ and $D = 3 \times 10^{-15}$ $cm^2\ s^{-1}$, which is at least an order of magnitude higher than the results obtained in this work.

However, the extracted limit for our diffusion coefficient might be too small due to a native oxide layer at the interface that forms instantaneously after cleaning the silicon surface before depositing of the aluminium film. This oxide layer is a diffusion barrier for the aluminium atoms. In order to avoid such an oxide layer, aluminium ions were implanted into a certain depth to be in direct contact with silicon.

7.1.2. ROOM TEMPERATURE IMPLANTATION

The implantation of 5×10^{16} aluminium ions cm^{-2} into Si <100> and Si <111> at room temperature created an amorphous layer in the surface region with thicknesses of $X_a = 376 \pm 19$ *nm* and $X_a = 367 \pm 19$ *nm* respectively, as deduced from the channeling spectra in Fig. 20, Fig. 21 and summarised in table 3. Partial regrowth of the crystal lattice from the bulk after annealing at $T_a = 500$, 700 and 900 °C was observed.

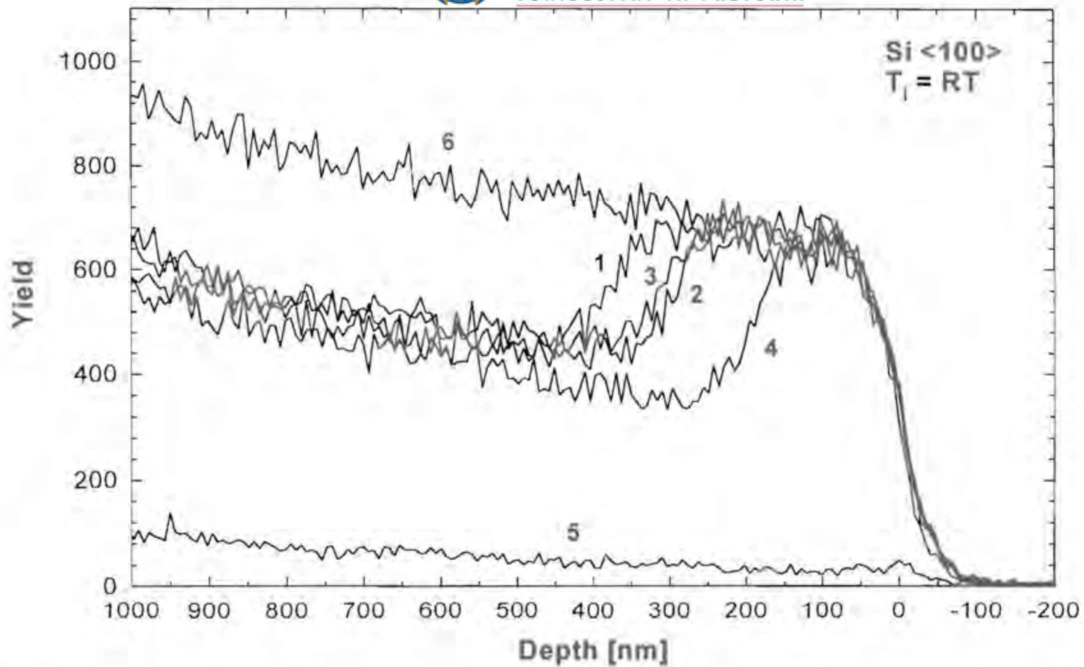

Fig. 20: Aligned backscattering spectra of Si <100> for room temperature implantation of 5×10^{16} Al^{+} cm^{-2} before (1) and after annealing for one hour at 500 °C (2), 700 °C (3) and 900 °C (4). Also given are aligned (5) and random (6) spectra of unimplanted samples; α - particle energies have been converted to a depth scale.

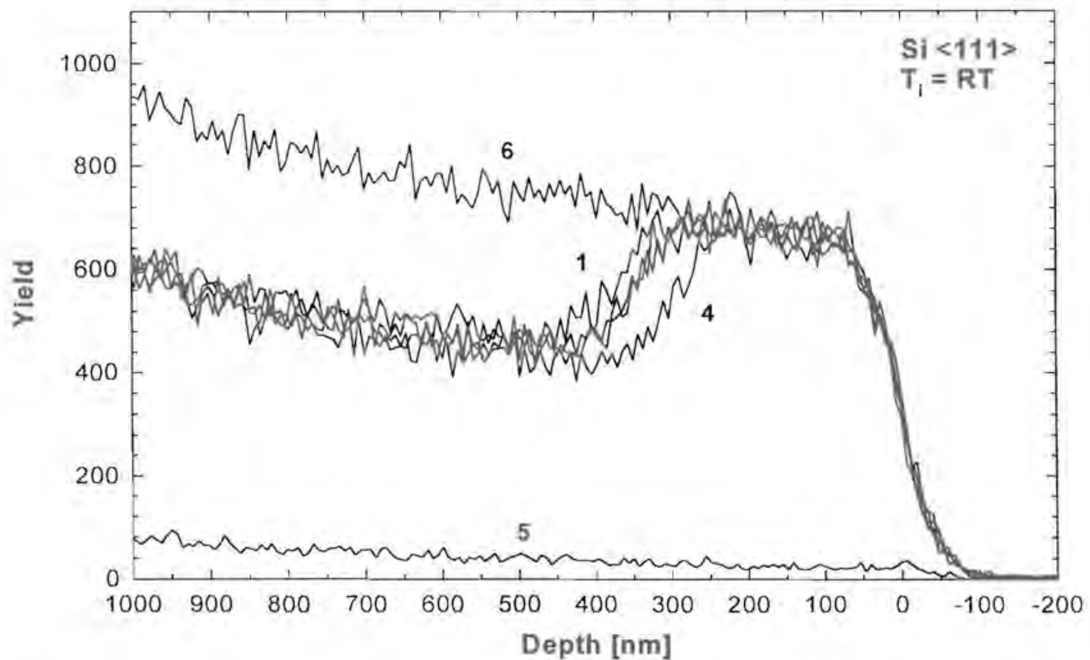

Fig. 21: Aligned backscattering spectra of Si <111> for room temperature implantation of 5×10^{16} Al^{+} cm^{-2} before (1) and after annealing for one hour at 500 °C, 700 °C and 900 °C (4). Also given are aligned (5) and random (6) spectra of unimplanted samples; α - particle energies have been converted to a depth scale.

UNIVERSITEIT VAN PRETORIA
UNIVERSITY OF PRETORIA
YUNIBESITHI YA PRETORIA

The amorphised surface layer of the Si <100> sample reduced to $X_a = 295 \pm 15$ *nm* during annealing at $T_a = 500$ °C. Within experimental uncertainty a similar thickness of the amorphous layer was found after annealing at $T_a = 700$ °C. However, during annealing at $T_a =$ 900 °C the thickness of the amorphous layer decreased further to $X_a = 197 \pm 11$ *nm* (Fig.20). For the Si <111> samples a significantly smaller crystalline regrowth was observed. The thickness of the amorphous layer reduced to $X_a = 349 \pm 18$ *nm* during annealing at $T_a = 500$ °C. A similar result within experimental uncertainty was obtained for the sample annealed at $T_a = 700$ °C, while the thickness of the amorphous layer decreased further to $X_a = 295 \pm 15$ *nm* after annealing at $T_a = 900$ °C (Fig. 21).

The apparent difference in annealing behaviour of the two lattice orientations might be explained by assuming that regrowth takes place along the preferred <100> direction. The experimentally observed ratio of $\Delta_{<111>} / \Delta_{<100>} = 0.40 \pm 0.14$ for the regrown layer thicknesses at 900 °C is just outside the 1σ error of the expected ratio of 0.58.

Sample	**Thickness of highly disordered surface region X_a [*nm*]**
Si <100> implanted at RT as implanted	376 ± 19
Annealed at 500 °C for 1 hour	295 ± 15
Annealed at 700 °C for 1 hour	308 ± 16
Annealed at 900 °C for 1 hour	197 ± 11
Si <111> implanted at RT as implanted	367 ± 19
Annealed at 500 °C for 1 hour	349 ± 18
Annealed at 700 °C for 1 hour	346 ± 18
Annealed at 900 °C for 1 hour	295 ± 15

Table 3: Thickness of the highly disordered surface region in silicon after aluminium implantation obtained with channeling.

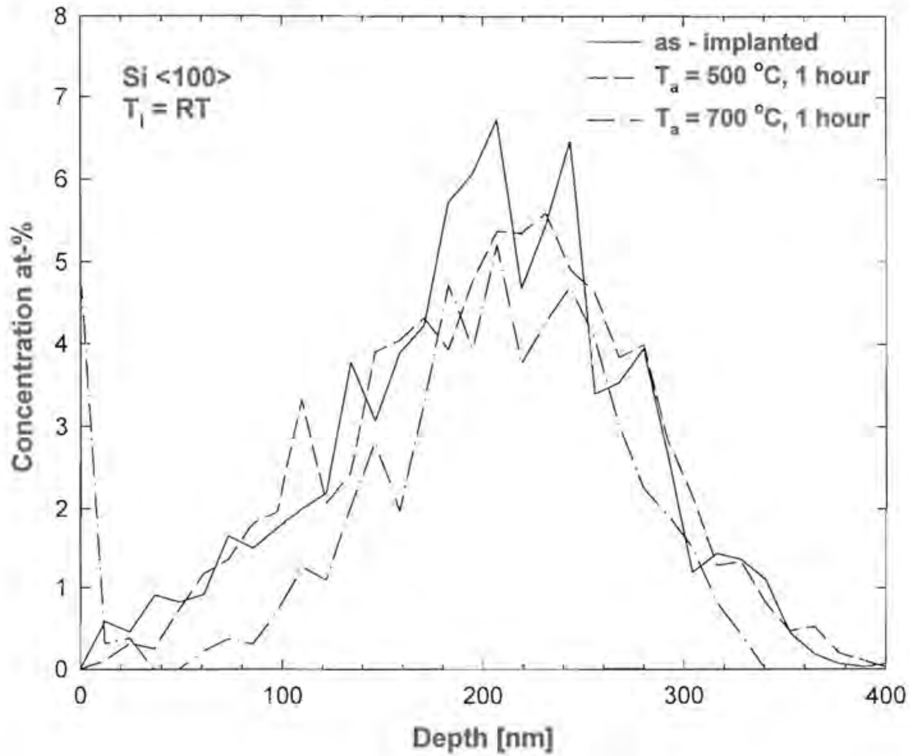

Fig. 22: Depth profiles of aluminium implanted at room temperature with a fluence of 5 x 10^{16} cm^{-2} into Si <100> before and after annealing for one hour at different temperatures.

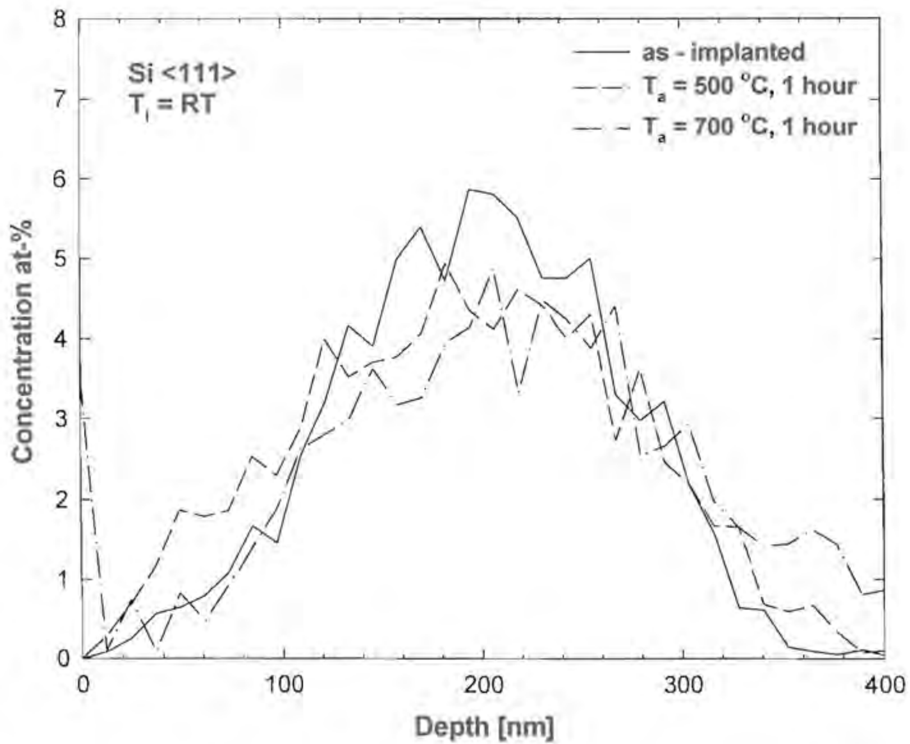

Fig. 23: Depth profiles of aluminium implanted at room temperature with a fluence of 5 x 10^{16} cm^{-2} into Si <111> before and after annealing for one hour at different temperatures.

The depth profiles of the implanted aluminium atoms before and after different annealing cycles are displayed in Fig. 22 and Fig. 23. The experimentally obtained mean ranges of the aluminium atoms were $R_p = 200 \pm 16$ *nm* in Si <100> and $R_p = 204 \pm 16$ *nm* in Si <111> before annealing.

Results for the second range moments were $\Delta R_p = 75 \pm 5$ *nm* for Si <100> and $\Delta R_p = 69 \pm 5$ *nm* for Si <111>. During annealing for one hour at $T_a = 500$ °C the second range moment stayed within experimental uncertainty at $\Delta R_p = 74 \pm 6$ *nm* in Si <100> and increased slightly to $\Delta R_p = 80 \pm 7$ *nm* in Si <111>. From these values aluminium diffusion coefficients below the detection limit of $D \leq 10^{-15}$ cm^2 s^{-1} were obtained for both orientations.

After annealing for one hour at $T_a = 700$ °C an aluminium surface peak appears. However, the first range moment of the remaining implantation profile does not differ significantly from the as-implanted distribution for both orientations. The second range moment is slightly smaller but still within the experimental error. Apparently a small percentage of the aluminium starts at this temperature to diffuse to the surface, where it is trapped after reducing the native silicon oxide layer SiO_2 [63,65]. The temperature increase from 500 to 700 °C is not high enough to further improve the crystalline re-growth. The thickness of the amorphous surface layer is unchanged compared with the one at $T_a = 500$ °C. However, $T_a = 700$ °C is high enough to activate aluminium diffusion through the highly disordered region to the surface.

During annealing at $T_a = 900$ °C the implanted aluminium atoms diffused completely out of the sample to the surface. The damage depth is strongly reduced, however, the anomalous diffusion with coefficients of $D \approx 10^{-13}$ cm^2 s^{-1} in both sample orientations is obviously due to defect structures still present after annealing at $T_a = 900$ °C and cannot be compared with aluminium diffusion coefficients in a defect-free silicon lattice.

7.1.3. HOT IMPLANTATION

The channeling spectra for Si <100> and Si <111> after implantation of 5 x 10^{16} aluminium ions cm^{-2} at $T_i = 250$ °C are displayed in Fig. 24 and Fig. 25. In both samples a surface region up to a depth of $X_c = 110 \pm 6$ *nm* was observed to be nearly defect-free.

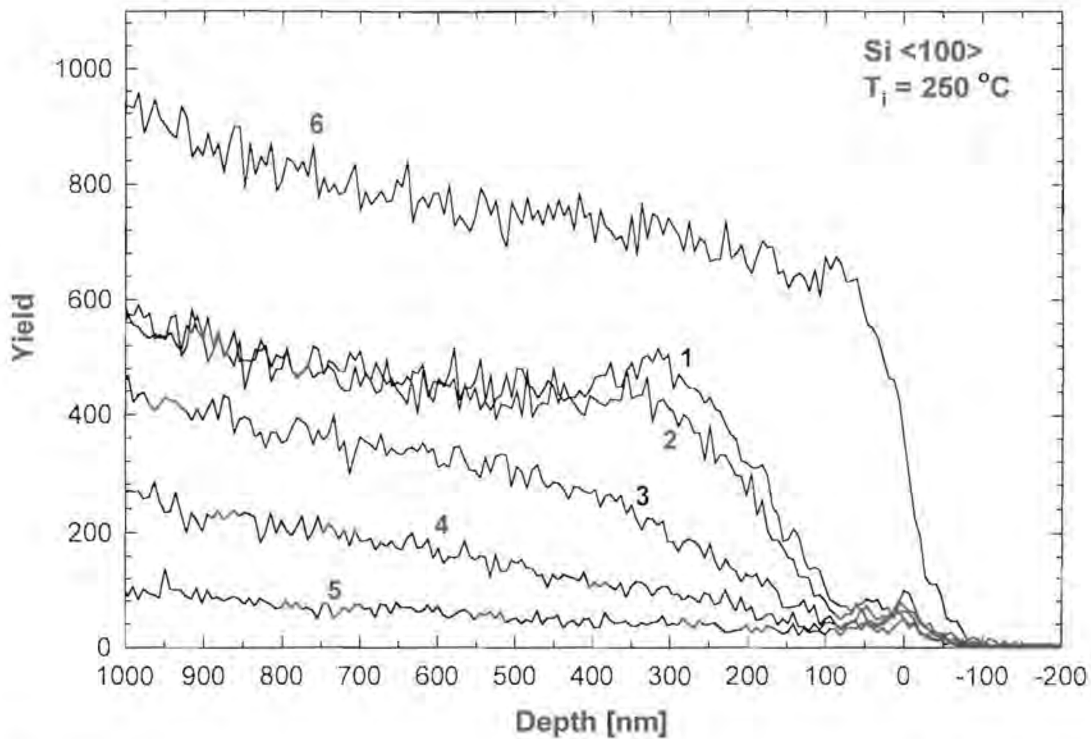

Fig. 24: Aligned backscattering spectra of Si <100> for implantation of 5 x 10^{16} Al^+ cm^{-2} at T_i = 250 °C before (1) and after annealing for one hour at 500 °C (2), 700 °C (3) and 900 °C (4). Also given are aligned (5) and random (6) spectra of unimplanted samples; α - particle energies have been converted to a depth scale.

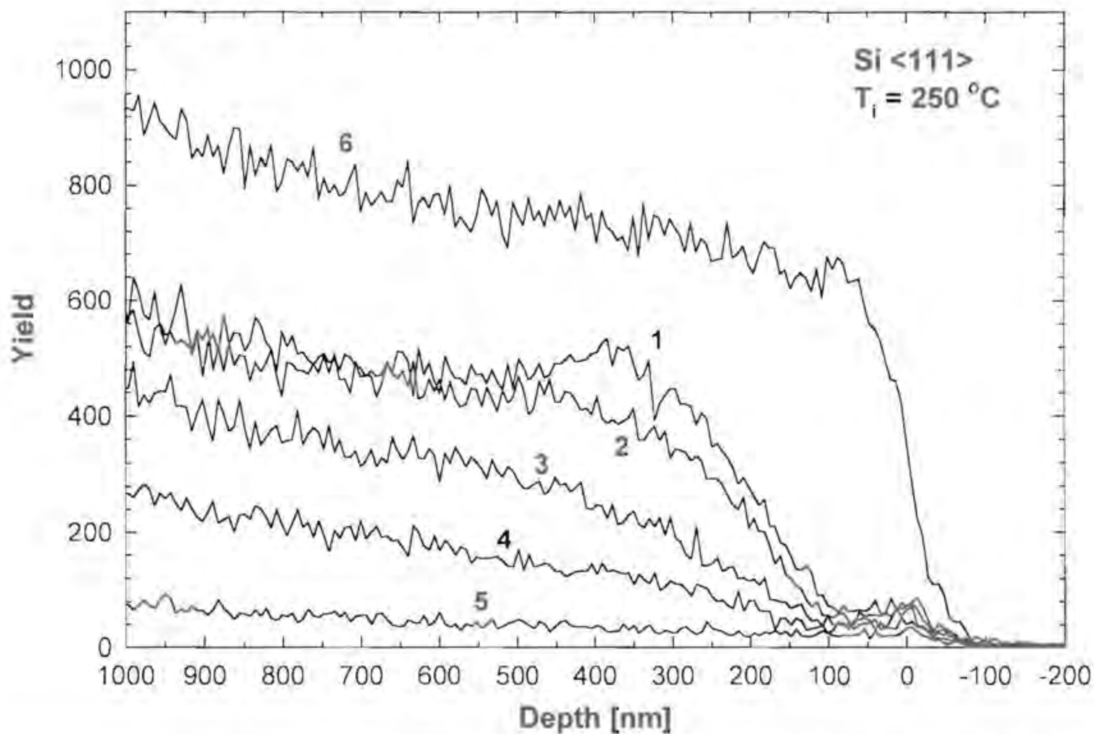

Fig. 25: Aligned backscattering spectra of Si <111> for implantation of 5 x 10^{16} Al^+ cm^{-2} at T_i = 250 °C before (1) and after annealing for one hour at 500 °C (2), 700 °C (3) and 900 °C (4). Also given are aligned (5) and random (6) spectra of unimplanted samples; α - particle energies have been converted to a depth scale.

Extended defect creation is prevented by irradiation induced annealing. No amorphous layer, as in the case of the room temperature implantation, was formed. The observed minimum yield in the region beyond the surface peak of the as-implanted Si<100> is χ_{min} = 14 %. After annealing at T_a = 500 °C the minimum yield reduced to χ_{min} = 9.8 % and to χ_{min} = 7 % after annealing at T_a = 700 °C. One hour of annealing at T_a = 900 °C resulted in a minimum yield of χ_{min} = 5.9 %. A similar behaviour was observed in Si <111>. Before annealing a minimum yield of χ_{min} = 14 % was obtained. The minimum yield improved to χ_{min} = 9.8 % after annealing at T_a = 500 °C and after annealing at T_a = 700 and 900 °C it was reduced to χ_{min} = 5.5 %.

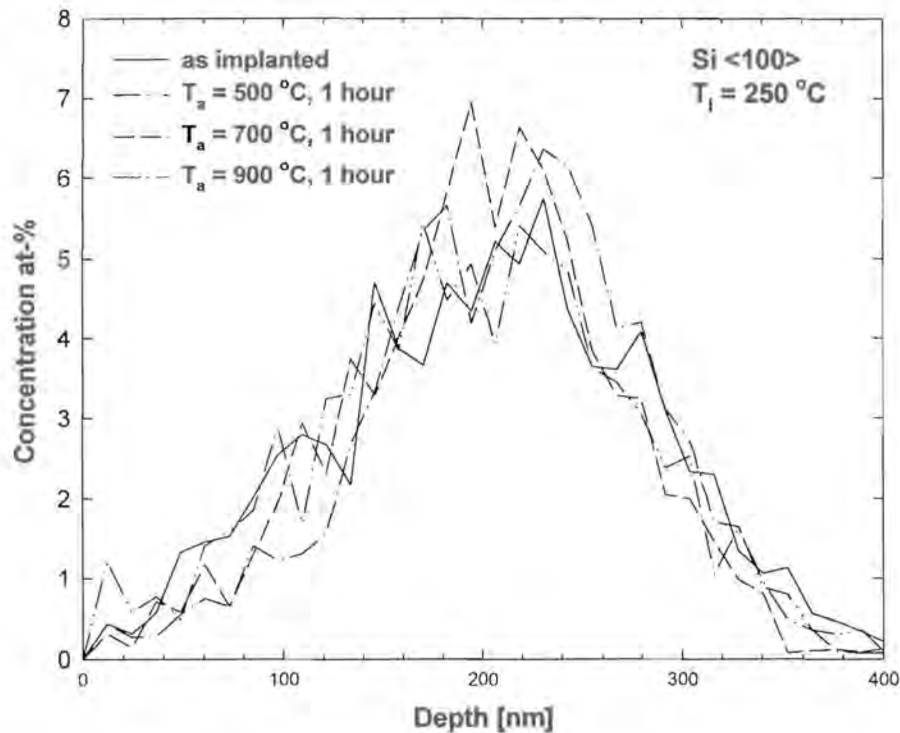

Fig. 26: Depth profiles of aluminium implanted at T_i = 250 °C with a fluence of 5 x 10^{16} cm^{-2} into Si <100> before and after annealing for one hour at different temperatures T_a.

In contrast to the room temperature implantation no significant difference is observed for the <100> and <111> orientation and strong annealing occurs between 500 and 700 °C. This is an indication that different radiation induced defects occur in the implanted depth compared to the room temperature implantation where complete amorphisation in the surface region up to and slightly beyond the implanted depth was observed.

From the reduction of the dechanneling yield it is obvious that the dislocation density reduces during each annealing temperature. The values for the minimum yield obtained after annealing at T_a = 900 °C were only slightly higher than those of unimplanted samples prepared from the same wafers. The χ_{min} of virgin Si <100> was at 4.4 % slightly higher than that of Si <111> at 3.7 %. From the shape of the channeling spectra and the low minimum yield it can be concluded that radiation induced annealing plays an important role during implantation at T_i = 250 °C.

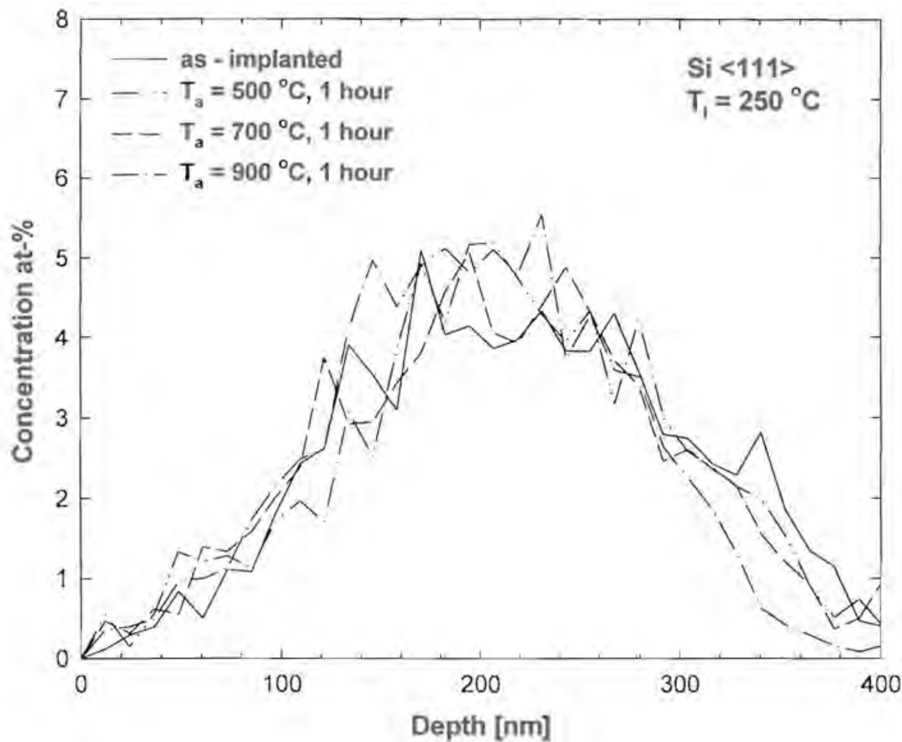

Fig. 27: Depth profiles of aluminium implanted at T_i = 250 °C with a fluence of 5 x 10^{16} cm^{-2} into Si <111> before and after annealing for one hour at different temperatures T_a.

The depth profiles of aluminium in Si <100> and Si <111> after the hot implantation are displayed in Fig. 26 and Fig. 27, respectively. Annealing at temperatures of T_a = 500, 700 and 900 °C for one hour does not change the shape of the implanted aluminium depth profile significantly. The mean projected range of the as-implanted aluminium is $R_p = 204 \pm 16$ *nm* in Si <100> and $R_p = 220 \pm 16$ *nm* in Si <111>. The values obtained for the second range moment are $\Delta R_p = 79 \pm 6$ *nm* and $\Delta R_p = 83 \pm 7$ *nm*, respectively. These values agree within experimental error with those obtained for the room temperature implantation before

annealing. For our hot implantation parameters radiation enhanced diffusion coefficients below the detection limit at $D \leq 10^{-15}$ cm^2 s^{-1} were obtained for both orientations by taking into account the implantation time. In Si <100> the mean projected range stays constant within experimental error during annealing for one hour at T_a = 900 °C. The value obtained for the second range moment stayed constant up to an annealing temperature of T_a = 700 °C. It decreased slightly to ΔR_p = 68 ± 5 nm during annealing at T_a = 900 °C, but was still within the experimental error.

Sample	Range R_p [nm]	Second moment ΔR_p [nm]	Thermal diffusion Coefficient D [cm^2 s^{-1}]
Si (100), T_i = RT	200 ± 16	75 ± 5	-
T_a = 500 °C, 1 hour	206 ± 16	74 ± 6	$\leq 10^{-15}$
T_a = 700 °C, 1 hour	210 ± 16	65 ± 5	(*) $\approx 10^{-15}$
T_a = 900 °C, 1 hour	Complete out-diffusion to the surface		(*) $\approx 10^{-13}$
Si (100), T_i = 250 °C	204 ± 16	79 ± 6	-
T_a = 500 °C, 1 hour	196 ± 16	78 ± 6	$\leq 10^{-15}$
T_a = 700 °C, 1 hour	199 ± 16	67 ± 5	$\leq 10^{-15}$
T_a = 900 °C, 1 hour	212 ± 16	68 ± 5	$\leq 10^{-15}$
Si (111), T_i = RT	204 ± 16	69 ± 5	-
T_a = 500 °C, 1 hour	204 ± 16	80 ± 6	$\leq 10^{-15}$
T_a = 700 °C, 1 hour	223 ± 16	76 ± 7	(*) $\approx 10^{-15}$
T_a = 900 °C, 1 hour	Complete out-diffusion to the surface		(*) $\approx 10^{-13}$
Si (111), T_i = 250 °C	220 ± 16	83 ± 7	-
T_a = 500 °C, 1 hour	215 ± 16	82 ± 7	$\leq 10^{-15}$
T_a = 700 °C, 1 hour	212 ± 16	83 ± 7	$\leq 10^{-15}$
T_a = 900 °C, 1 hour	200 ± 16	73 ± 6	$\leq 10^{-15}$

Table 4: Range parameters and thermal diffusion coefficients of implanted aluminium in silicon obtained with NRA.

A similar behaviour is observed in Si <111>. Here the second moment stayed constant up to an annealing temperature of T_a = 700 °C. It decreased slightly to ΔR_p = 73 ± 6 *nm* during annealing at T_a = 900 °C. A summary of the experimental range moments and diffusion coefficients is shown in table 4. The diffusion coefficients marked with (*) are defect induced and several orders of magnitude larger than those expected in defect free silicon.

The dechanneling yield in the aligned spectrum of the as-implanted sample reaches a maximum between 350 and 380 *nm* into the crystal, which is much deeper than the mean range of the implanted aluminium ions.

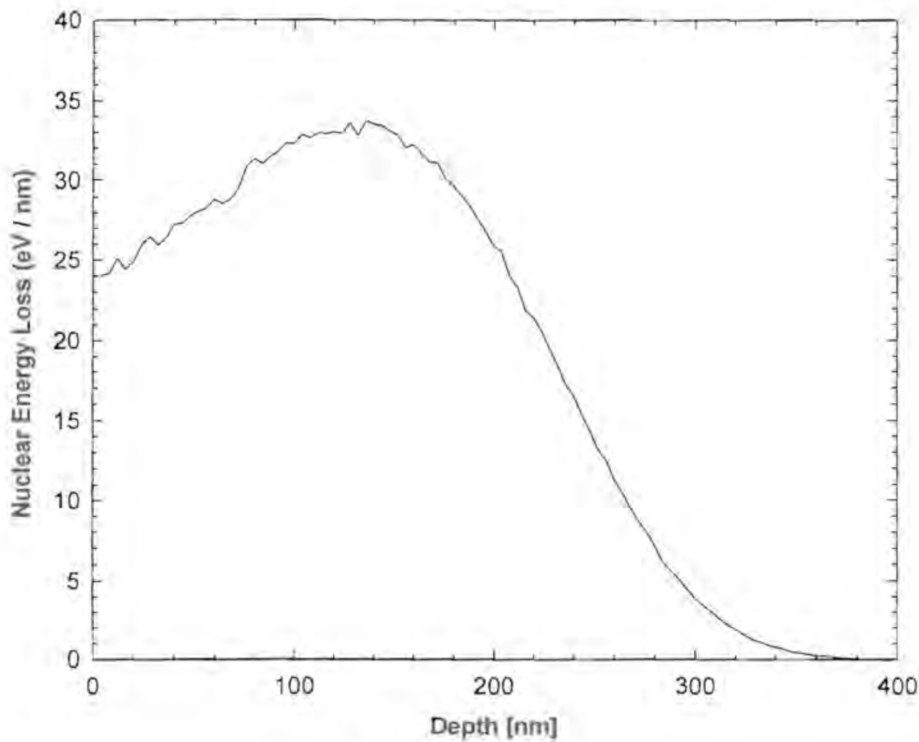

Fig. 28: TRIM calculation of the nuclear energy loss for an aluminium ion in silicon at an energy of 120 keV.

The nuclear energy loss depth distribution from an aluminium implantation at an energy of 120 *keV* calculated by TRIM (SRIM 2000 – Version) is displayed in Fig. 28. This nuclear energy loss was obtained by adding the energy losses due to recoil collisions and phonon creation. The radiation-induced damage in the target is closely related to this nuclear energy loss. From this calculation it is therefore deduced that the damage range, which is defined as the distance from the surface at which the defect density drops to 50 % of its maximum, is at

a depth of 243 *nm*. However, the experimentally observed damage reaches about 100 *nm* deeper into the crystal than the predicted nuclear energy loss. Such enhanced damage ranges were previously only reported in metals [93], where they could be explained with the formation of dislocations reaching much deeper than the mean range of the implanted ions.

The damage peaks disappear during annealing and the remaining slopes of the dechanneling yield near the surface for T_a = 900 °C is not much larger than for unimplanted samples. The slightly higher dechanneling slope beyond a depth of approximately 100 *nm* is due to the implanted aluminium, which reaches a peak concentration of about 5 at.% at 200 *nm*. No channeling effect was, however, observed for the γ-ray yield with a proton beam, indicating random lattice positions for the impurity atoms. This is expected because of the extremely low solubility of aluminium in silicon [55].

The dramatic change of the aligned spectra for α-particles during annealing, without a corresponding change of the implantation profiles can only be explained by assuming that during the hot implantation an amorphisation of the target is effectively prevented. Only short-range disorder appears to occur near the end of the ion range with most of the lattice information still available to allow complete re-growth during annealing.

From the binary phase diagram [55] for the silicon aluminium system it is obvious, that for a maximum concentration of about 5 at.% aluminium at a target depth of 200 *nm* two phases are formed at 900 °C. At this depth 8 % of the compound will be in the liquid phase, consisting of 37 % silicon and 63 % aluminium. The solid phase mainly consists of silicon due to the low solubility of aluminium. When cooling the samples after annealing, aluminium probably segregates at its implanted depth.

An Arrhenius plot of previously reported aluminium diffusion coefficients in silicon, including the results obtained in this study is displayed in Fig. 29. An upper limit for the diffusion coefficients at $D \leq 10^{-15}$ cm^2 s^{-1} was extracted after annealing samples of the hot implantation. Our diffusion coefficients are about an order of magnitude smaller than the values obtained by extrapolating previously published results to 900 °C and could be explained by segregation into metallic aluminium during annealing [64]. The value from the

room temperature implantation is much too high, due to defect assisted diffusion, but corresponds well with some of the published values. The upper limit from the in-diffusion investigation $D \leq 10^{-16}$ cm^2 s^{-1} at 900 °C is also included in this figure. However, this limit is probably too low due to the native silicon oxide layer at the interface.

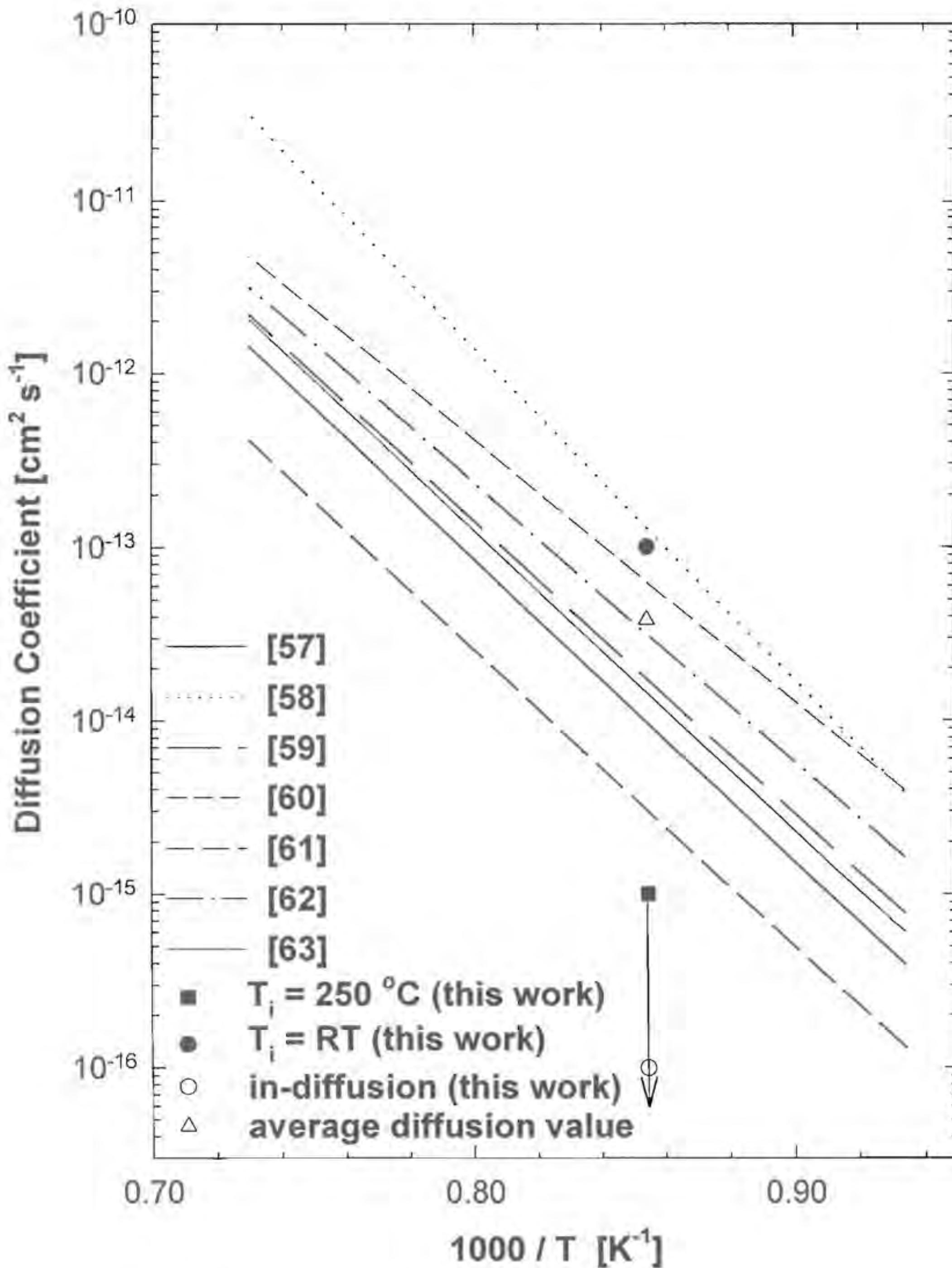

Fig.29: Comparison of the diffusion coefficients of aluminium in silicon obtained in this work at 900 °C with previously reported results (table 2).

7.2. GERMANIUM

In comparison with silicon relatively little research was done on germanium in recent years. To our knowledge only two investigations on aluminium diffusion in germanium were reported previously. One of them dating back to 1982 by *Dorner* et al. [71], the other to 1967 by *Meer* et al.[72]. From the results by *Meer* et al. expected diffusion coefficients are calculated to $D = 1 \times 10^{-19}\ cm^2\ s^{-1}$ and $D = 2.4 \times 10^{-15}\ cm^2\ s^{-1}$ at 500 °C and 700 °C, respectively. *Dorner* et al. measured a diffusion coefficient of $D = 1.2 \times 10^{-15}\ cm^2\ s^{-1}$ at 700 °C. After extrapolating their results to 500 °C a coefficient of $D = 3 \times 10^{-20}\ cm^2\ s^{-1}$ is calculated. As these are the only two reports on aluminium diffusion in germanium and their results differ by factors of 2-3, the present study was performed to verify the validity of these results by applying a different analysing method. At 700 °C the aluminium diffusion coefficients appear to be in the range that can be detected with our analysing method.

7.2.1. ALUMINIUM DIFFUSION INTO GERMANIUM

The in-diffusion of aluminium into <111> germanium for temperatures up to 700 °C was investigated. A thin aluminium film was deposited onto clean crystalline germanium. The deposited amount of aluminium is crucial [71]. It should not be too large because of its low solubility in germanium and due to its high vapour pressure at the selected annealing temperatures it can partly vaporise from the surface. Ideal film thicknesses for in-diffusion analysis were experimentally determined to be between 5 and 28 *nm* [71]. The thickness of our deposited aluminium film at 13 ± 3 *nm* is within this interval.

The samples cut from this wafer were analysed before and after the different annealing cycles. The normalised depth profiles of the aluminium films before and after annealing for 1 hour at $T_a = 500$ °C and $T_a = 700$ °C, respectively are shown in Fig. 30.

Slight differences in the film thickness of $\Delta d \approx 4\ nm$ just at the detection limit are due to inhomogeneities during the lateral vapour deposition onto the wafer. However, the film thickness holds no diffusion information and such small differences are actually below the detection limit of our system.

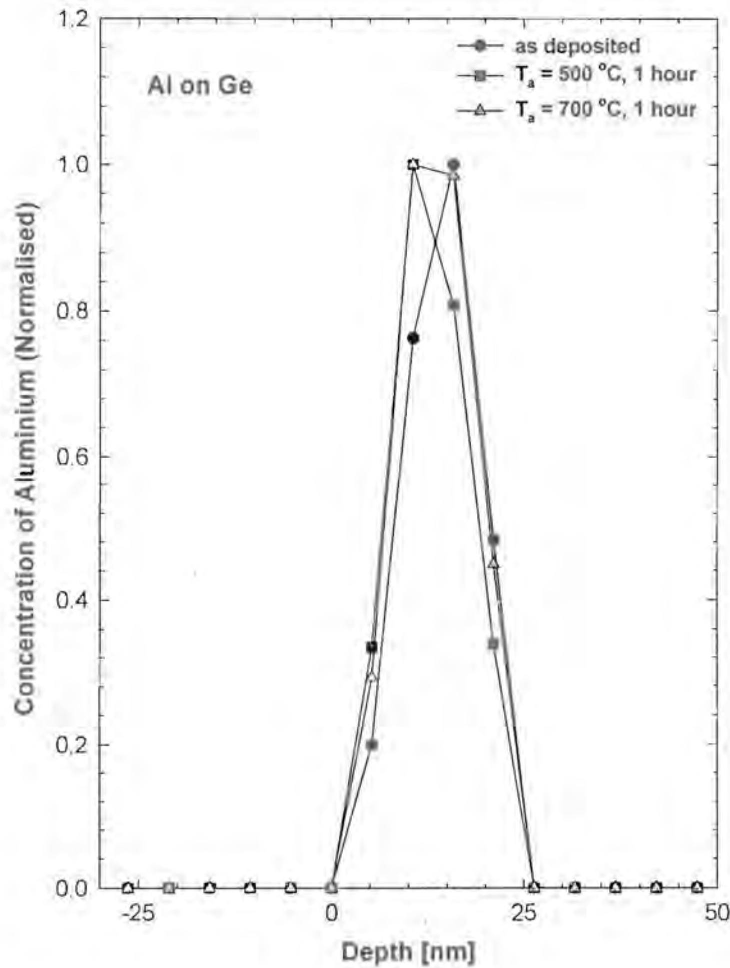

Fig. 30: Depth profiles of a vapour deposited aluminium layer on germanium before and after annealing for one hour at different temperatures T_a.

The width of the interface between the aluminium film and the germanium bulk material remains within experimental error at 5 *nm* before and after annealing for one hour at T_a = 700 °C. Therefore no significant aluminium diffusion into the germanium sample occurred. An upper limit for the diffusion coefficient at $D \leq 10^{-16}$ cm^2 s^{-1} for 500 and 700 °C was extracted from the aluminium depth profiles.

In the case of 500 °C the diffusion coefficient obtained in this study did not contradict the predicted values by *Dorner* and *Meer*. However, the upper limit for the diffusion coefficient of $D \leq 10^{-16}$ cm^2 s^{-1} extracted after annealing for one hour at T_a = 700 °C is an order of magnitude lower than the ones expected from *Dorner* and *Meer*.

A thin native oxide layer forms instantaneously after cleaning the germanium substrate due to the low heat of formation for this reaction. This oxide layer can act as a diffusion barrier for the aluminium atoms. The obtained upper limit of the diffusion coefficients is therefore probably too small. Additional measurements on this system were performed, where the diffusion source was placed within the germanium by aluminium ion implantation. This brings the two elements into direct contact with each other.

7.2.2. ROOM TEMPERATURE IMPLANTATION

The depth profiles of 5 x 10^{16} aluminium ions cm^{-2} implanted into germanium at room temperature before and after subsequent annealing for one hour at T_a = 500 and 700 °C are shown in Fig. 31. The experimentally obtained mean range of the implanted aluminium ions before annealing was at $R_p = 107 \pm 13$ *nm* with a second range moment of $\Delta R_p = 53 \pm 4$ *nm*. After annealing at T_a = 500 °C for one hour the mean range of the aluminium atoms in the germanium reduced to $R_p = 82 \pm 13$ *nm* which is just within experimental error of the value before annealing. However, the depth profile becomes also wider and changes dramatically. The second range moment $\Delta R_p = 86 \pm 6$ *nm* is outside the experimental error. Diffusion out of the sample to the surface occurred. The observed high aluminium concentration at the surface together with its high affinity for oxygen leads to the suspicion that Al_2O_3 segregates at the surface. An aluminium diffusion coefficient of $D \approx 10^{-14}$ cm^2 s^{-1} was extracted at T_a = 500 °C.

Annealing for one hour at T_a = 700 °C caused a large fraction of aluminium atoms to diffuse out of the sample to the surface. The mean range and the second range moment of the remaining aluminium atoms in the sample were at $R_p = 117 \pm 25$ *nm* and $\Delta R_p = 56 \pm 15$ *nm*, respectively, and therefore within experimental error of the range parameters before annealing. However, the remaining maximum aluminium concentration within the target was 1.5 at. %, which was much lower than the maximum concentration of 8 at. % before annealing. A diffusion coefficient of $D \approx 10^{-13}$ cm^2 s^{-1} at 700 °C was extracted for aluminium in germanium.

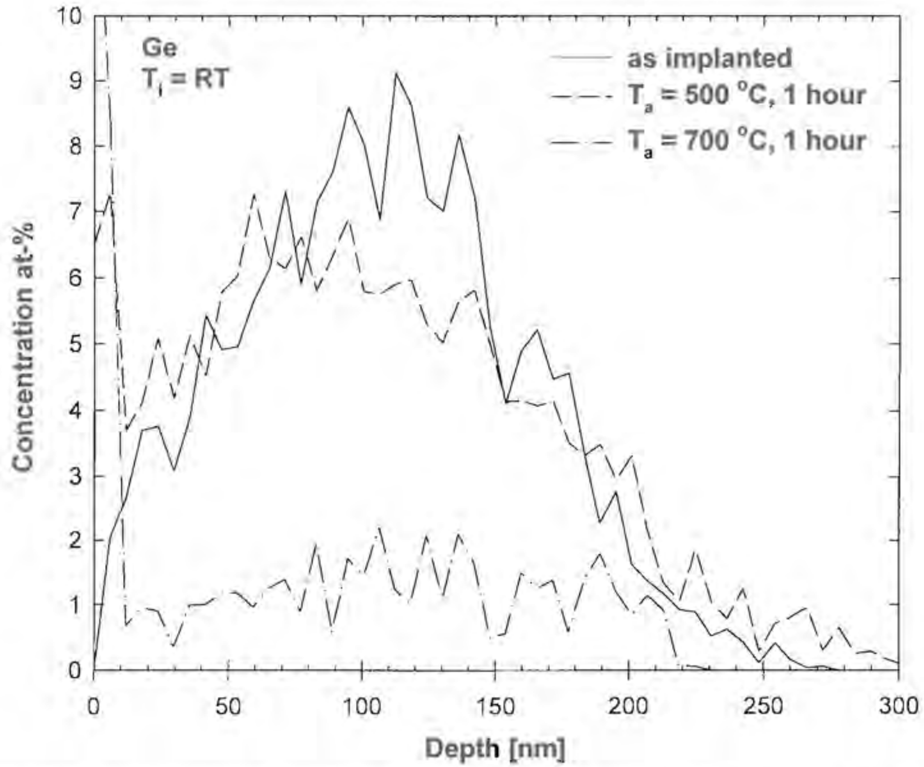

Fig. 31: Depth profiles of aluminium implanted at room temperature into germanium before and after annealing for one hour at different temperatures T_a.

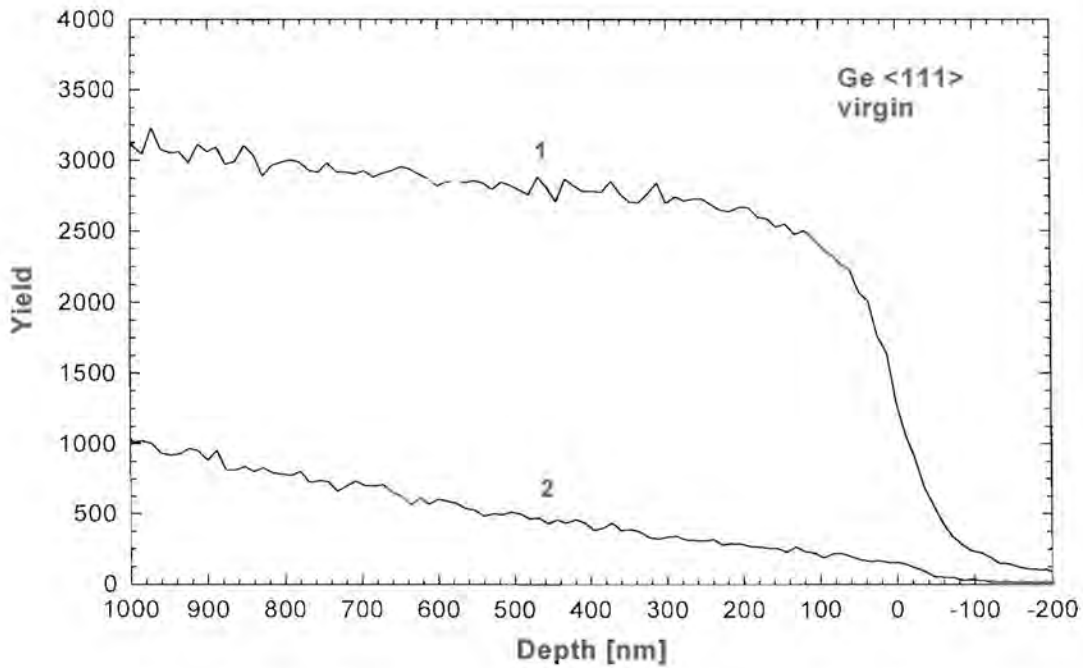

Fig. 32: Random (1) and aligned (2) backscattering spectra of Ge<111> before implantation.

The channeling spectra for a Ge<111> sample before implantation is displayed in Fig. 32. The minimum yield of the aligned spectrum is χ_{min} = 15 % and a rather high dechanneling yield is observed. No change in the dechanneling behaviour was observed after annealing the unimplanted germanium sample for two hours at T_a = 600 °C. This is an indication that extended defects such as dislocations are present deep into the crystal. Channeling spectra of implanted samples could not be obtained due to the heavy radiation-induced damage in samples with an already high defect concentration. A hot implant largely avoids this damage but those channeling spectra could also not be obtained because of the large scattering cross section of displaced germanium atoms.

Due to radiation induced damage in germanium the aluminium diffusion appears to be largely enhanced. This effect was also observed for the room temperature implanted silicon (chapter 7.1.) and the extracted diffusion coefficients are much too large if compared to those obtained from the aluminium in-diffusion experiments into germanium.

7.2.3. HOT IMPLANTATION

The same fluence of aluminium ions as for the room-temperature implantation was implanted at T_i = 250 °C into several germanium samples. The aluminium depth profiles before and after annealing for one hour at T_a = 500 and 700 °C respectively are displayed in Fig. 33.

The mean range of the aluminium atoms is at a depth of R_p = 111 ± 13 *nm* with a second range moment of ΔR_p= 59 ± 5 *nm*. These aluminium range moments in germanium agree within the experimental error with those obtained for the room temperature implantation. No noticeable difference is observed in the distribution. The upper limit for the radiation-enhanced diffusion during the hot implantation is therefore at $D \leq 10^{-15}$ cm^2 s^{-1} for our implantation parameters by taking into account the implantation time.

After annealing for one hour at T_a = 500 °C the mean range of the implanted aluminium atoms was measured at R_p = 106 ± 13 *nm* with a second range moment of ΔR_p= 54 ± 4 *nm*. The diffusion of aluminium atoms to the surface, which was observed after annealing the room-temperature implanted samples, did not occur after annealing the hot implants for one hour at T_a = 500 °C. An upper limit for the diffusion coefficient of $D \leq 10^{-15}$ cm^2 s^{-1} at 500 °C

was extracted, which does not contradict the predicted coefficients from *Dorner* [71] and *Meer* [72] as those are much smaller and not measurable with our method.

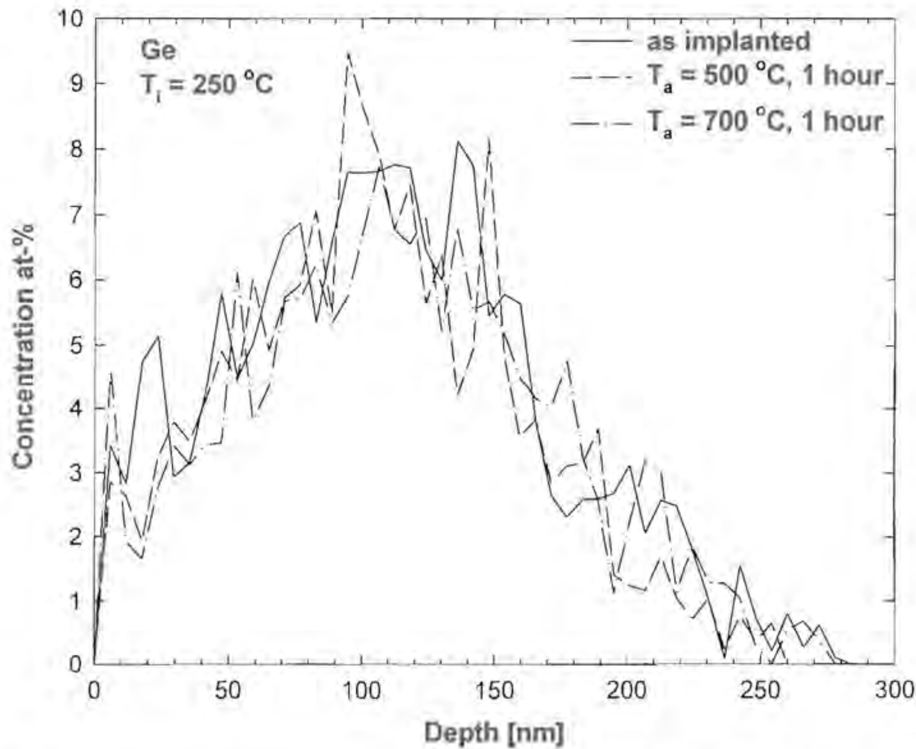

Fig. 33: Depth profiles of aluminium implanted at T_i = 250 °C with a fluence of 5 x 10^{16} cm^{-2} into germanium before and after annealing for one hour at different temperatures T_a.

Annealing for one hour at T_a = 700 °C results in a mean range of the implanted aluminium atoms of R_p = 115 ± 13 *nm* with a second range moment of ΔR_p= 59 ± 5 *nm*. These values agree within experimental error with those obtained before annealing. The upper limit for the diffusion coefficient is again at $D \leq 10^{-15}$ cm^2 s^{-1} and agrees with values obtained for the in-diffusion analysis. It is, however, smaller by a factor of two compared to the calculated coefficients from the data by *Meer* at 700 °C but does not contradict the experimental results by *Dorner*.

The maximum concentration of about 7 at.% aluminium in germanium is at a depth of 110 *nm*. For the germanium aluminium system it is obvious from the binary phase diagram [70], that at this depth two phases are formed at 700 °C. About 17 % of the compound are in the liquid phase, consisting of 57 % germanium and 43 % aluminium. The solid phase mainly consists of germanium due to the fairly low solubility of aluminium. When cooling the samples after annealing aluminium is suspected to segregate at the implanted depth.

An Arrhenius plot of the previously reported diffusion coefficients as well as the results obtained in this study is shown in Fig. 34. The rather small upper limit obtained from the in-diffusion analysis (hollow circle) is probably due to the native oxide layer at the interface between the aluminium film and the germanium substrate. A few monolayers of GeO_2 act as a diffusion barrier, which limits a possible aluminium in-diffusion. Diffusion coefficients obtained from the hot implantation agree well with results obtained by *Dorner*.

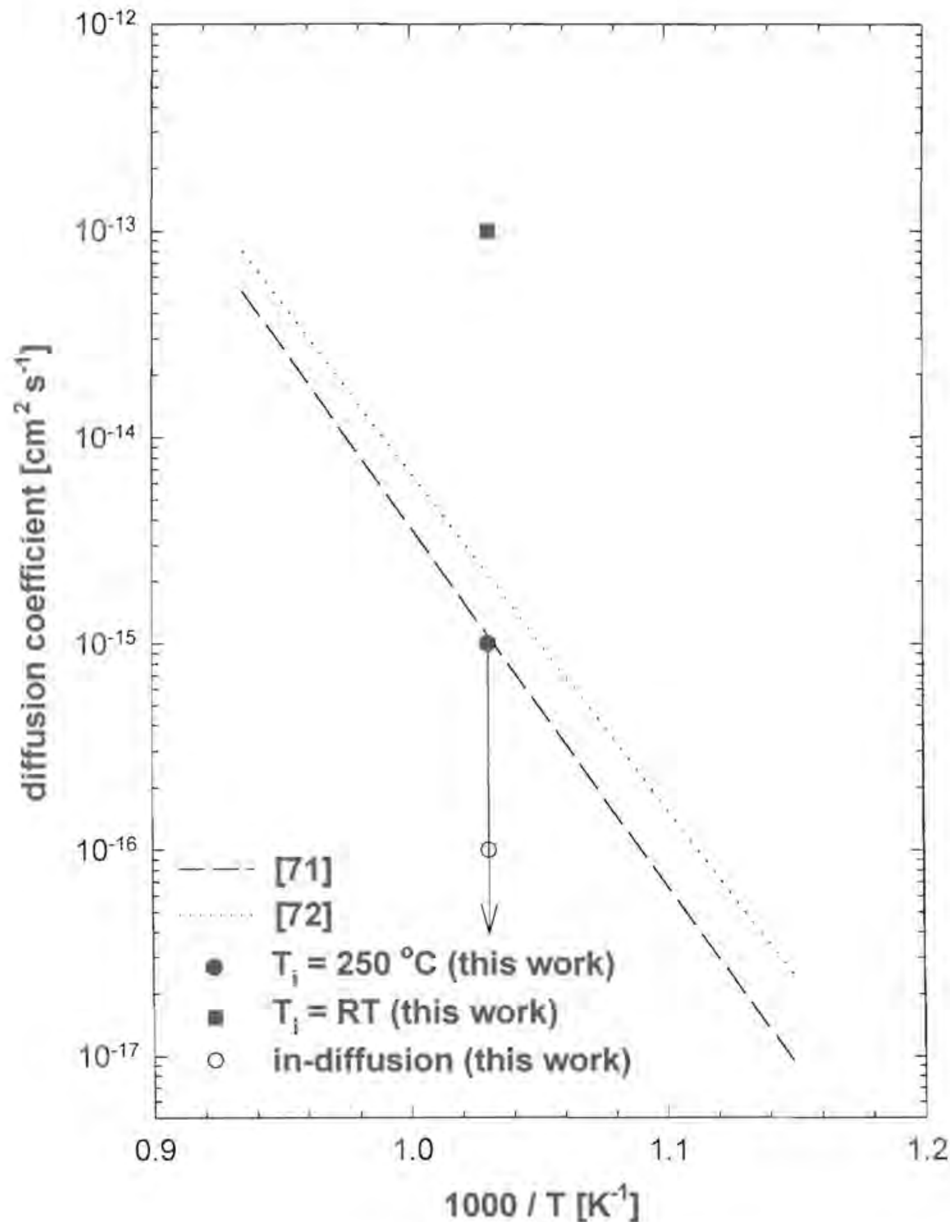

Fig. 34: Comparison of the diffusion coefficients of aluminium in germanium obtained in this work at 700 °C with previously reported results.

Sample Germanium	**Range R_p [nm]**	**Straggling ΔR_p [nm]**	**Thermal diffusion coefficient D [$cm^2 s^{-1}$]**
T_I = RT, as-implanted	107 ± 13	53 ± 4	-
T_I = RT, T_a = 500 °C	82 ± 13	86 ± 6	(*) $\approx 10^{-14}$
T_I = RT, T_a = 700 °C	117 ± 25	56 ± 15	(*) $\approx 10^{-13}$
T_I = 250 °C, as implanted	111 ± 13	59 ± 5	-
T_I = 250 °C, T_a = 500 °C	106 ± 13	54 ± 4	$\leq 10^{-15}$
T_I = 250 °C, T_a = 700 °C	115 ± 13	59 ± 5	$\leq 10^{-15}$

Table 5: Range parameters of aluminium in germanium and thermal diffusion coefficients.

Table 5 summarises obtained range parameters of the implanted aluminium in germanium before and after annealing, as well as the upper limits for the diffusion coefficients at 500 °C and 700 °C. The coefficients marked with (*) are probably damage induced and some orders of magnitude larger than those expected in nearly defect free germanium. The observed aluminium out-diffusion after annealing the room-temperature implanted germanium is most probably due to the radiation induced disorder still present after annealing at T_a = 700 °C as no detectable aluminium diffusion occurred during annealing the hot implanted germanium samples at this temperature.

7.3. GALLIUM ARSENIDE

Gallium arsenide is a widely used compound semiconductor. Due to the possibility of the formation of superlattices many results on the inter-diffusion of aluminium and gallium were reported as described in chapter 6.2.1. It was found that the self-diffusion of gallium in gallium arsenide is strongly correlated to the aluminium diffusion in this compound.

For higher annealing temperatures it is necessary to supply the samples with an arsenic overpressure in order to avoid arsenic loss to the vapour phase. This already happens at temperatures in excess of $T_a \approx 600$ °C [81,89]. From the binary phase diagram [90] it is obvious that an arsenic loss of the compound at temperatures above T > 29.7 °C shifts the alloy to a two-phase region, where a small percentage, consisting mainly of gallium, would be in the liquid phase. A diffusion prediction is not possible for such a degraded compound. An arsenic loss has therefore to be avoided. Due to unavailability of a facility to anneal the samples at an arsenic overpressure, anneals in this study were performed at $T_a \leq 500$ °C to stay well below the critical temperature. As there was generally no difference between the experimental results for $T_a = 400$ °C and $T_a = 500$ °C, only results for the higher annealing temperature are given in this chapter.

When extrapolating Fig. 18, the diffusion coefficient at 500 °C is expected to be about $D \approx 10^{-30}$ cm^2 s^{-1} and therefore much lower than the detection limit of the applied method. However, the radiation-induced amorphisation in elemental semiconductors silicon and germanium after room temperature implantation, which is described in chapters 7.1. and 7.2., respectively, resulted in an enhancement of the aluminium diffusion coefficient by several orders of magnitude. This study of the GaAs-Al system was performed to investigate if radiation induced aluminium diffusion is observed. Results from annealing room temperature implanted samples, where a diffusion enhancement could be possible, are compared with those from the in-diffusion investigation and the hot implantation study.

7.3.1. ALUMINIUM DIFFUSION INTO GALLIUM ARSENIDE

The in-diffusion of aluminium into gallium arsenide at T_a = 500 °C was investigated. This investigation was performed to compare our results with previously reported diffusion coefficients that were mainly obtained by investigating inter-diffusion of multilayered structures (chapter 6.2.1.). A gallium arsenide wafer was cut in half and cleaned. Onto one of the halves a 17 ± 4 *nm* film of aluminium was deposited. Samples cut from this piece were analysed before and after different annealing cycles.

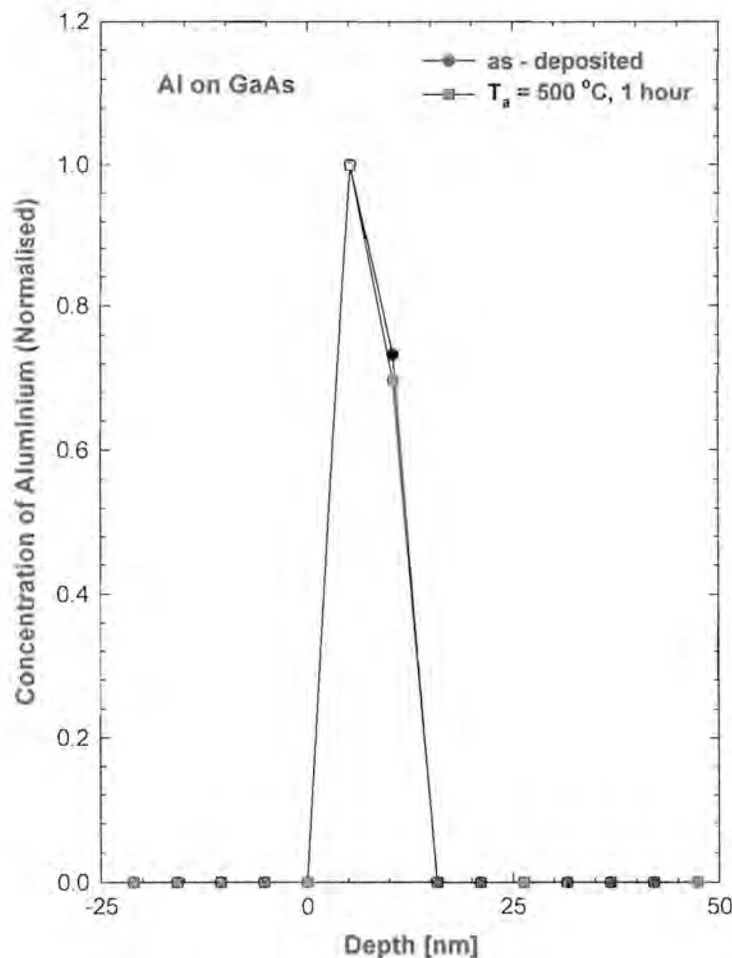

Fig. 35: Depth profiles of a vapour deposited aluminium layer on gallium arsenide before and after annealing for one hour at different temperatures T_a.

The depth profiles of the aluminium layer before and after annealing for one hour at T_a = 500 °C are shown in Fig. 35. The aluminium depth profile, measured after annealing another

sample for one hour at T_a = 400 °C, closely resembles the displayed profiles and is therefore not shown.

No variation in thickness of the aluminium films on gallium arsenide samples was observed from which it was concluded that the vapour deposition onto the gallium arsenide half was homogeneous. The width of the interface between the aluminium layer and the gallium arsenide sample stayed constant within experimental error at 5 *nm* before and after annealing at T_a = 500 °C for one hour, and no change in shape of the depth profiles was observed.

As the interface remains sharply defined up to the highest annealing temperature no significant aluminium in-diffusion into the gallium arsenide sample occurred. An upper limit for the diffusion coefficient of $D \leq 10^{-16}\ cm^2\ s^{-1}$ at 500 °C was extracted from the aluminium depth profiles which was expected because of the predicted undetectable diffusion coefficient from previous investigations on inter-diffusion in multilayer-structures.

7.3.2. ROOM TEMPERATURE IMPLANTATION

Defect induced diffusion played an important role in the diffusion behaviour of the room temperature implanted elemental semiconductors. This study is to investigate if such an enhancement is also observed in gallium arsenide. The room temperature implantation of 5×10^{16} aluminium ions cm^{-2} into gallium arsenide created an amorphous region at the surface of the sample. Strong dechanneling prevents the channeling effect to be seen at larger depths even after annealing samples for one hour at T_a = 400 °C.

After annealing samples for one hour at T_a = 500 °C a highly disordered surface region still remains, however some of the introduced damage annealed out already at this temperature and a channeling effect was seen at larger depths, which is displayed in Fig. 36. This agrees with previously reviewed minimum temperatures for measurable regrowth, which was observed to occurs in the annealing behaviour of amorphised layers in *III-V* semiconductors at T_a = 500 °C [91]. The thickness of the disordered surface region in the sample is about X_a = 160 ± 20 *nm* and is therefore still slightly deeper than the mean range of the implanted aluminium atoms.

The depth profiles of 5 x 10^{16} aluminium ions cm^{-2} implanted into gallium arsenide at room temperature before and after annealing for one hour at T_a = 500 °C are shown in Fig. 37. The experimentally obtained mean range of the implanted aluminium ions before annealing was R_p = 152 ± 16 *nm* and the second range moment was ΔR_p= 66 ± 5 *nm*.

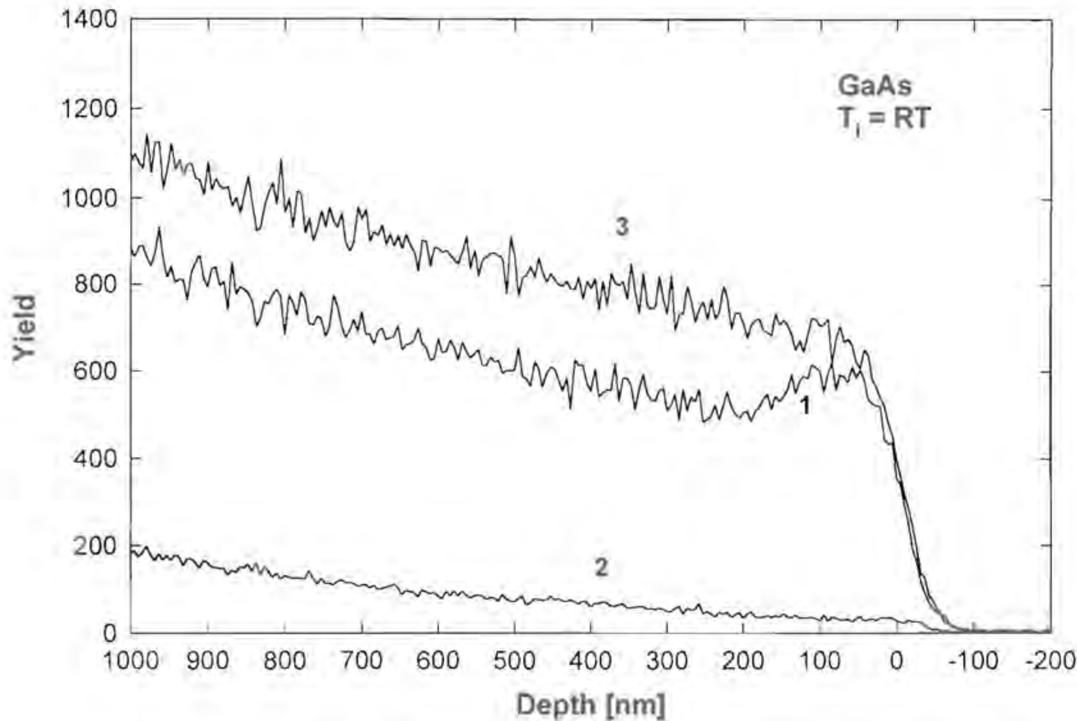

Fig. 36: Aligned backscattering spectra of gallium arsenide for room temperature implantation of 5 x 10^{16} Al^+ cm^{-2} after annealing for one hour at 500 °C (1). Also given are aligned (2) and random (3) spectra of unimplanted samples; α - particle energies have been converted to a depth scale in both, gallium and arsenic.

After annealing for one hour at T_a = 500 °C the measured mean range of the aluminium atoms in gallium arsenide remained unchanged at R_p= 147 ± 16 *nm*. The second range moment stayed at ΔR_p= 65 ± 5 *nm*, which is the same as before annealing. No aluminium diffusion to the surface was observed, contrary to the investigated elemental semiconductors in this study. Obviously the aluminium atoms are still inside the remaining highly disordered gallium arsenide lattice after annealing where they could be incorporated on gallium sites during the regrowth which is possible, considering that AlAs and GaAs are completely miscible into each other [104].

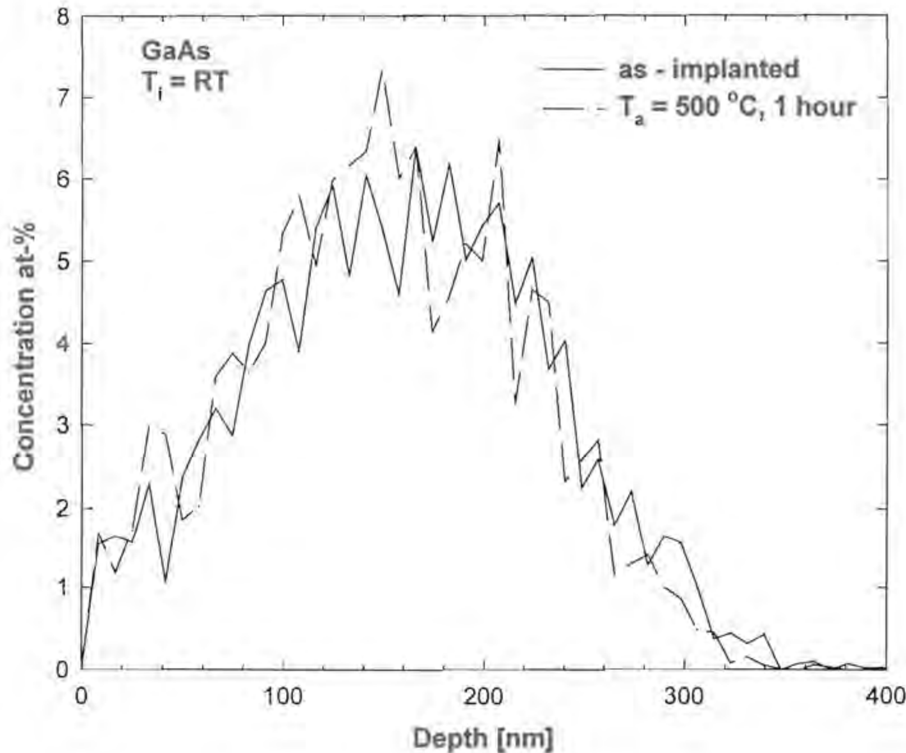

Fig. 37: Depth profiles of aluminium implanted at room temperature into gallium arsenide before and after annealing for one hour T_a = 500 °C.

An upper limit for the diffusion coefficient of $D \leq 10^{-15}$ cm^2 s^{-1} for 500 °C was extracted. However, a defect induced diffusion enhancement cannot be excluded because even an increase of the coefficient by several orders of magnitude would still be below our detection limit.

7.3.3. HOT IMPLANTATION

The channeling spectra for gallium arsenide after implantation of 5 x 10^{16} aluminium ions cm^{-2} at T_i = 250 °C are displayed in Fig. 38. The surface region was observed to be nearly defect-free. No highly disordered region, as was observed after room temperature implantation, was formed. From the shape of the channeling spectra and the low minimum yield it was concluded that radiation induced annealing plays an important role during implantation at T_i = 250 °C. This agrees well with reports on ion implantations at elevated temperatures into *III-V* compounds [91], where already during implantations at about 200 °C the point defect concentration will never exceed the critical limit for amorphisation, except probably near the end of the ion tracks, especially for light and medium mass ions (< 30

amu). Amorphous zones that are created along an ion track will shrink faster than new zones are created.

The observed minimum yield in the region beyond the surface of the as-implanted gallium arsenide sample is at χ_{min} = 10%. During annealing for one hour at T_a = 500 °C the minimum yield reduced to χ_{min} = 8% which indicates a slight recovery of the gallium arsenide lattice in the surface region, which is almost as low as the minimum yield of unimplanted gallium arsenide samples at χ_{min} = 5%. However, beyond a depth of 50 nm a rather large slope in the dechanneling yield is observed.

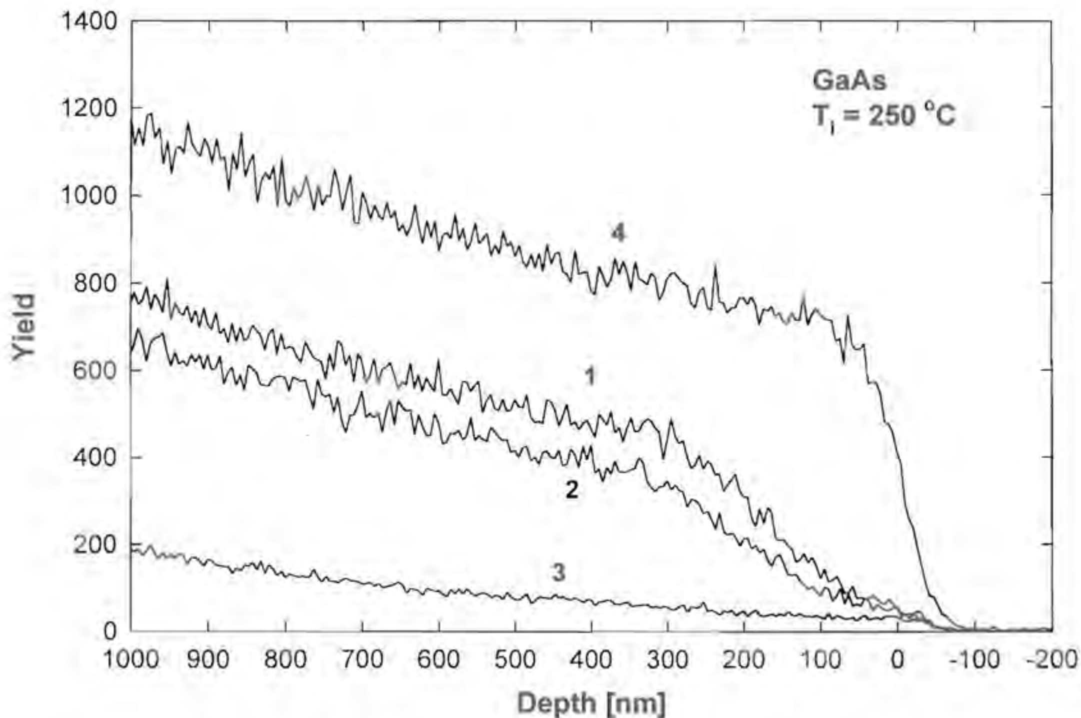

Fig. 38: Aligned backscattering spectra of gallium arsenide implantation of 5 x 10^{16} Al^+ cm^{-2} at T_i = 250 °C before (1) and after annealing for one hour at 500 °C (2). Also given are aligned (3) and random spectra of unimplanted samples; α - particle energies have been converted to a depth scale.

The increased slope of the dechanneling yield reaches to a depth of about 320 *nm* into the crystal, which is deeper than the detected mean range of the implanted aluminium ions. The shape of the dechanneling slope indicates extended defects such as dislocations that are

introduced during the hot implantation. The density of the dislocation network reduced slightly during annealing for one hour at 500 °C.

A similar result was already reported for implantation of 10^{15} Se^{+} cm^{-2} into gallium arsenide at T_i = 200 °C, where a discrete band of small dislocation loops and clusters was detected below the surface [92]. Their results were obtained with XTEM, RBS/channeling, SIMS and electrical measurements. They did not measure the selenium mean range in their study. However, from TRIM simulations a mean range of R_p = 174 *nm* was calculated, which is slightly deeper than our aluminium implant. The mean depth of their observed band of defects is at approximately 300 *nm* and therefore similar to the damage depth observed in this study. They concluded that the introduced defects from their hot selenium implantation were mainly dislocation loops and clusters.

The nuclear energy loss depth distribution as calculated with TRIM is displayed in Fig. 39. The nuclear energy loss is calculated by adding the ion energy losses due to recoils and the creation of phonons. As it is closely related to the introduced defects the damage range is calculated to be 165 *nm*, which is about half of the depth of our experimentally observed damage after the hot implantation. The damage depth after the room temperature implantation could not be measured because a channeling effect was not observed. However, a channeling effect was observed after annealing at 500 °C indicating crystalline regrowth from the bulk. A damage range similar to the mean range of the implanted aluminium was measured. In comparison hardly any regrowth occurred after annealing the hot implanted samples at this temperature. The damage depth remained much deeper than calculated and the slope reduced only slightly. It must be concluded that different types of defects are created during the different implantation temperatures. Radiation-induced defects in the surface region anneal out already during implantation. When considering that the hot implantation was performed at a higher dose rate than the room temperature implantation, the observed dislocation network is most probably because of denser collision cascades. Such dense collision cascades lead to shock-waves, which reach much deeper into the crystal than the mean range of the implanted ion.

Such enhanced damage ranges were previously only reported in metals [93], where they were explained with the formation of dislocations reaching much deeper than the mean range of the implanted ions due to dense collision cascades.

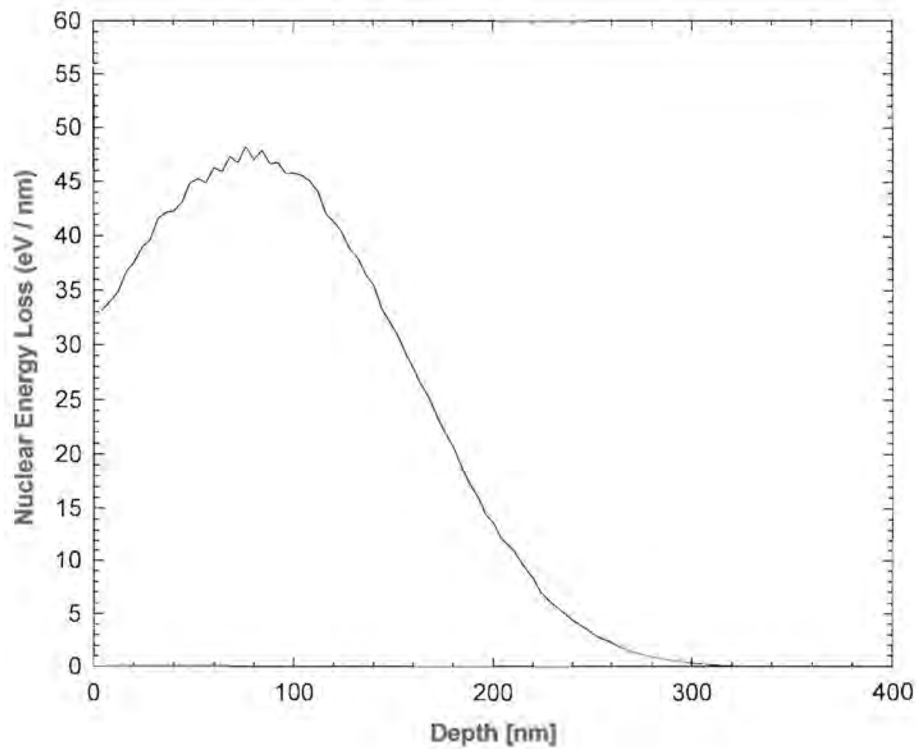

Fig. 39: Nuclear energy loss depth distribution of an aluminium ion at an energy of 120 keV in gallium arsenide as calculated with TRIM.

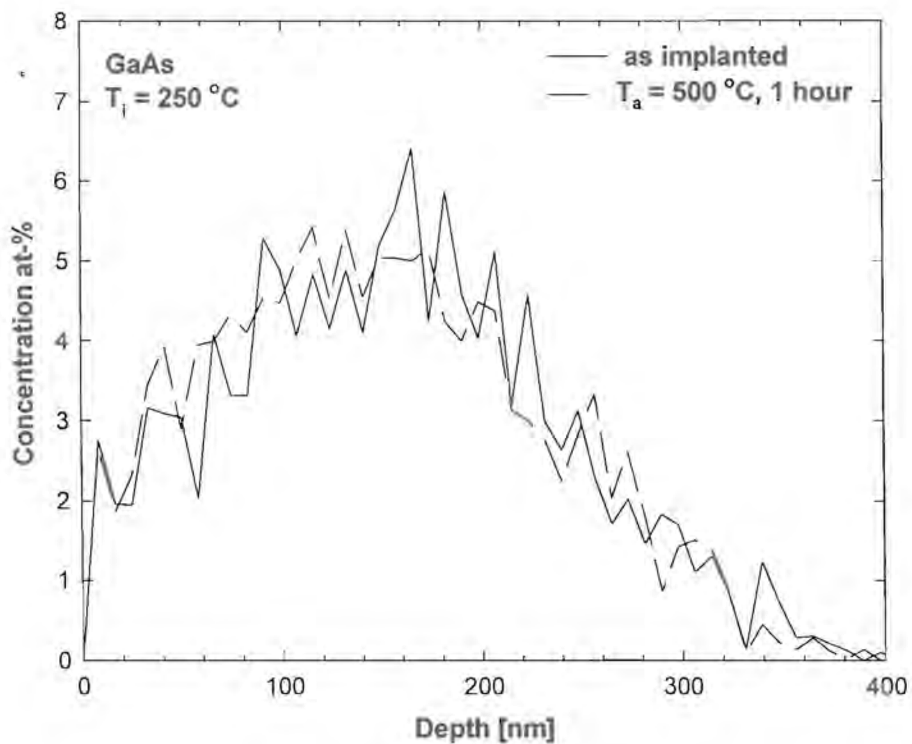

Fig. 40: Depth profiles of aluminium implanted at T_i= 250 °C into gallium arsenide before and after annealing for one hour T_a = 500 °C.

Aluminium depth profiles before and after annealing for one hour at T_a = 500 °C are displayed in Fig. 40. After implantation the mean range of the aluminium atoms is at a depth of R_p = 144 ± 16 *nm* with a second range moment of ΔR_p= 70 ± 5 *nm*. This is well within the experimental error of the values obtained for the room temperature implantation. The upper limit for the radiation-enhanced diffusion for these experimental parameters is at $D \leq 10^{-15}$ $cm^2\ s^{-1}$ by taking into account the implantation time.

After annealing for one hour at T_a = 500 °C the mean range of the implanted aluminium atoms was at R_p = 141 ± 16 *nm* with a second range moment of ΔR_p= 72 ± 5 *nm*. No visible diffusion to the surface occurred. An upper limit of the diffusion coefficient of $D \leq 10^{-15}$ $cm^2\ s^{-1}$ was extracted for annealing at T_a = 500 °C. However, the expected diffusion coefficient is not measurable with our method and therefore the obtained result is not in disagreement with previously published results.

Sample **Gallium arsenide**	**Range** R_p **[*nm*]**	**Straggling** ΔR_p **[*nm*]**	**Thermal diffusion** **coefficient** D **[$cm^2\ s^{-1}$]**
$T_i = RT$, as-implanted	152 ± 16	66 ± 5	-
$T_i = RT$, T_a = 500 °C	147 ± 16	65 ± 5	$\leq 10^{-15}$
T_i = 250 °C, as implanted	144 ± 16	70 ± 5	-
T_i = 250 °C, T_a = 500 °C	147 ± 16	72 ± 5	$\leq 10^{-15}$

Table 6: Summary of the experimental range parameters and thermal diffusion coefficients of implanted aluminium into gallium arsenide.

7.4. INDIUM PHOSPHIDE

Indium phosphide is one of the most important compound semiconductors. Many investigations were done because of its optoelectronic and high-speed digital applications. Picosecond optoelectronic switches with response times $\tau < 100$ picoseconds can be realised in indium phosphide after proton bombardment [94].

Diffusion coefficients of aluminium in indium phosphide were not found in the literature. It is important to understand the behaviour of doped semiconductors when they are exposed to heat. This study was therefore necessary to obtain information on diffusion coefficients of aluminium in indium phosphide. Decomposition occurs at annealing temperatures, typically in excess of $T_a = 600$ °C, necessary to activate implanted ions [95]. A phosphorous loss from the surface changes the stoichiometry in this compound. After phosphorous loss two phases exist in equilibrium already at room temperature. At lower annealing temperatures, e.g. for $T_a > 400$ °C, even in a nitrogen ambient a strong tendency for the surface to oxidise was observed [96,97]. To avoid these degrading effects the annealing temperatures for this study were kept at $T_a \leq 400$ °C during annealing in vacuum.

In order to investigate the in-diffusion a thin aluminium film was deposited onto a piece of indium phosphide. The obtained results are compared with those obtained after implantations at room temperature and at $T_i = 250$ °C in order to evaluate the influence of defect assisted diffusion effects in indium phosphide.

7.4.1. AL DIFFUSION INTO INDIUM PHOSPHIDE

The in-diffusion of aluminium into indium phosphide up to an annealing temperature of T_a = 400 °C was investigated. An indium phosphide wafer was cut in four pieces and cleaned. Onto one of the quarters a 12 ± 4 *nm* film of aluminium was deposited. The samples of 5 x 5 mm cut from this piece were analysed before and after annealing. The depth profiles of the aluminium layer before and after annealing for one hour at $T_a = 400$ °C are shown in Fig. 41.

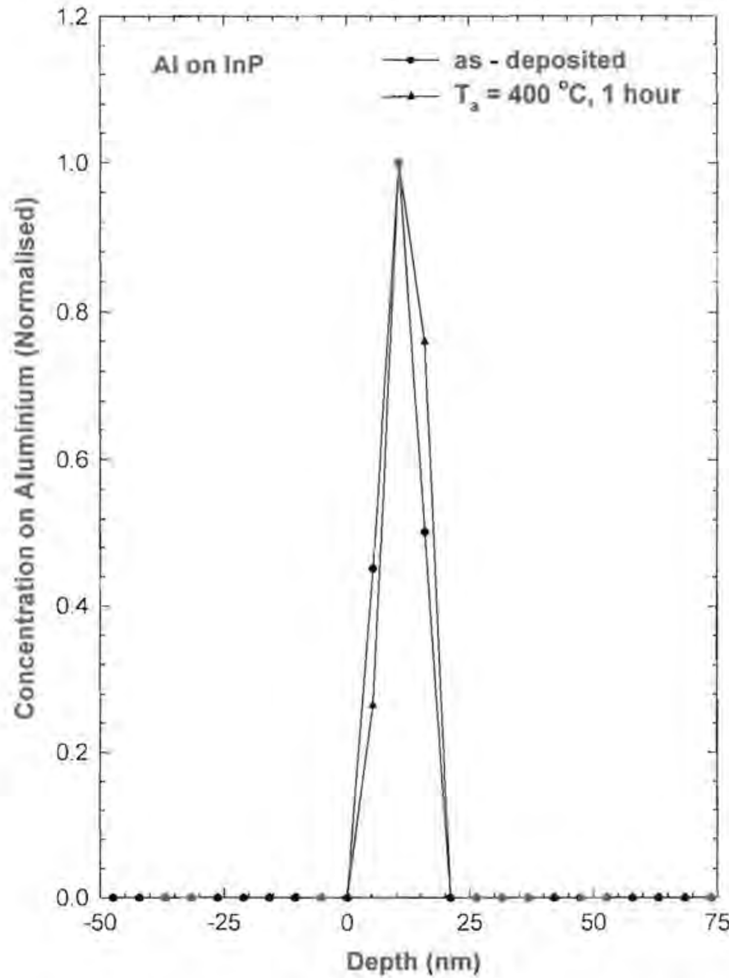

Fig. 41: Depth profiles of a vapour deposited aluminium layer on indium phosphide before and after annealing for one hour at T_a = 400 °C.

As it was the case for most of the semiconductors investigated and summarised in this chapter a slight difference in the film thickness due to inhomogenities during the vapour deposition onto the specimen is observed. However, diffusion effects are only related to the sharpness of the interface between the aluminium film and the indium phosphide wafer. The width of this interface remains within the detection limit of our method at 2.5 *nm* before and after annealing at a temperature of T_a = 400 °C. The interface remains therefore sharply defined and no change in shape of the depth profiles is observed before and after annealing. As no aluminium diffusion into the indium phosphide sample occurred within our detection limit at 400 °C, an upper limit for the aluminium diffusion coefficient in indium phosphide at $D \leq 10^{-16}$ $cm^2\ s^{-1}$ was extracted. The actual coefficient could be higher due to a possible formation of a polycrystalline In_2O_3 layer at the interface [98]. However, a surface discolouring, which is supposed to indicate the surface oxidation was not observed before and after annealing. Therefore we expect this limit for the coefficient at 400 °C to be in the right range.

7.4.2. ROOM TEMPERATURE IMPLANTATION

The implantation of 5 x 10^{16} aluminium ions cm^{-2} implanted into indium phosphide at room temperature created a highly disordered region with a thickness of $X_a = 465 \pm 24$ *nm* at the surface of the sample as deduced from the channeling spectra in Fig. 42. The thickness of this disordered layer is about four times deeper than the mean range of the implanted aluminium atoms at $R_p = 117 \pm 10$ *nm* (Fig. 44). The α-particle energies in the backscattering spectrum were converted to a depth scale.

After annealing for one hour at $T_a = 300$ °C the thickness of the amorphous layer reduced to $X_a = 409 \pm 22$ *nm*. No further crystalline regrowth of the highly disordered layer was observed after annealing a sample for one hour at $T_a = 400$ °C.

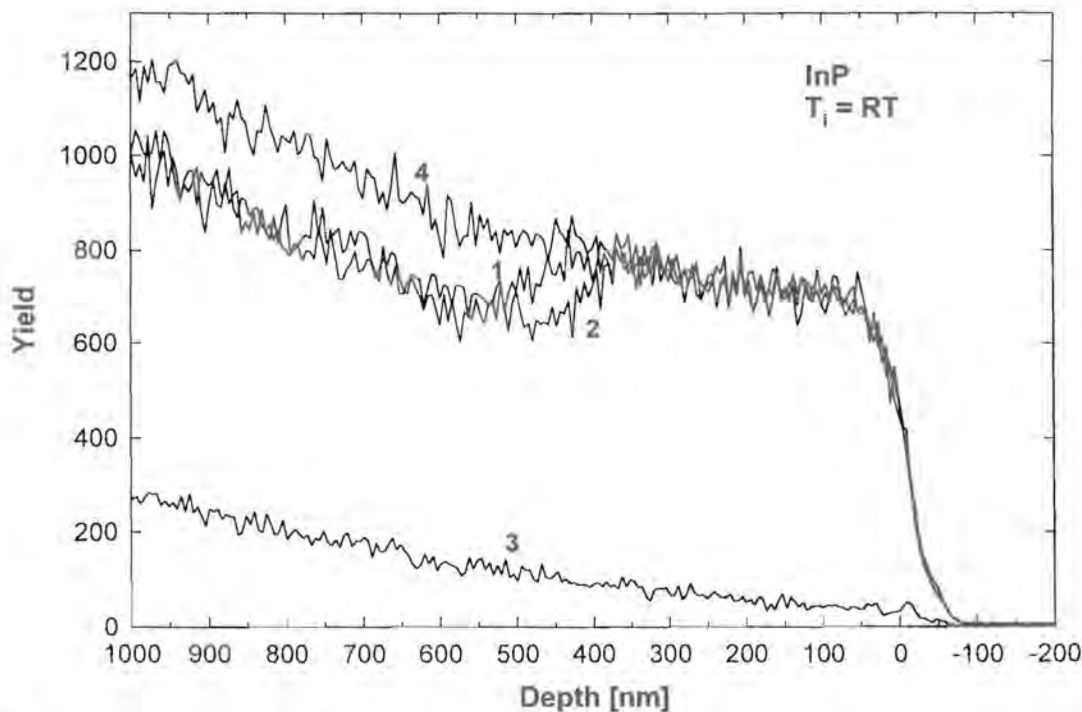

Fig. 42: Aligned backscattering spectra of indium phosphide for room temperature implantation of 5 x 10^{16} Al^{+} cm^{-2} before (1) and after annealing for one hour at 300 °C (400 °C) (2). Also given are aligned (3) and random (4) spectra of unimplanted samples; α - particle energies have been converted to a depth scale.

The nuclear energy loss depth distribution of aluminium in indium phosphide as calculated with TRIM is displayed in Fig. 43. A damage range of 192 *nm* can be extracted from this distribution. When we compare the thickness of our amorphous layer after implantation with the predicted damage range, then the observed amorphous layer is larger by more than a factor of two. In this study larger defect layers than predicted were already observed after hot aluminium implantations into gallium arsenide. After room temperature implantations of aluminium in silicon larger defect layers were also observed. It could have been also present in gallium arsenide but the samples could not be channeled.

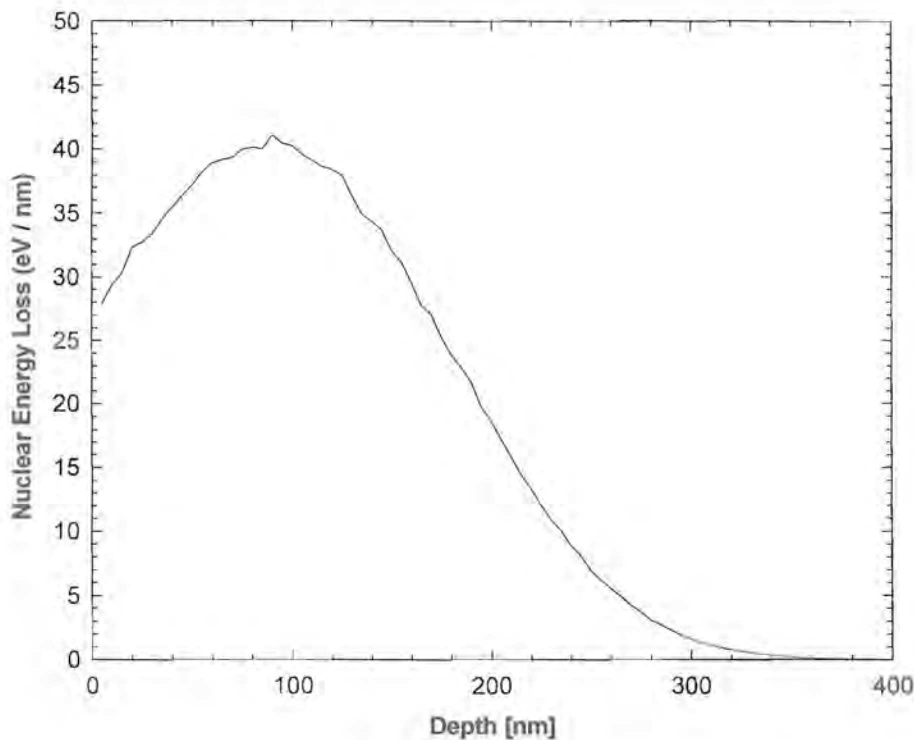

Fig. 43: Nuclear energy loss depth distribution of an aluminium ion at an energy of 120 keV in indium phosphide as calculated by TRIM.

The depth profiles of 5×10^{16} aluminium ions cm^{-2} implanted into indium phosphide at room temperature before and after annealing for one hour at $T_a = 300$ and 400 °C are shown in Fig. 44. The experimentally obtained mean range of the implanted aluminium ions before annealing was at $R_p = 117 \pm 10$ *nm* and the second range moment was at $\Delta R_p = 56 \pm 4$ *nm*.

During annealing for one hour at T_a = 300 °C the mean range of the aluminium atoms in the indium phosphide remained the same within experimental error at R_p= 113 ± 10 *nm*. The second range moment ΔR_p= 55 ± 4 *nm* also did not change within experimental error.

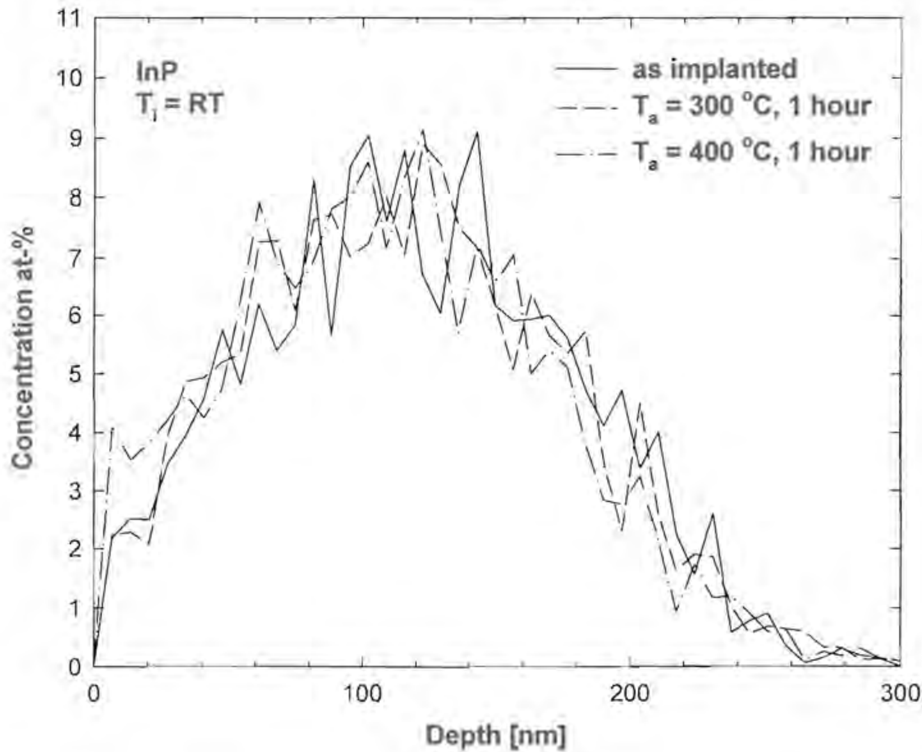

Fig. 44: Depth profiles of aluminium implanted at room temperature into indium phosphide before and after annealing for one hour at different annealing temperatures T_a.

The same results within experimental error were obtained during annealing for one hour at T_a = 400 °C. Here the mean range of the aluminium atoms was at R_p= 108 ± 10 *nm* and the second range moment at ΔR_p= 55 ± 4 *nm*. No aluminium diffusion to the surface was observed. An upper limit of the diffusion coefficient of $D \leq 10^{-15}$ cm^2 s^{-1} for T_a = 400 °C agrees well with the results obtained for in-diffusion. Diffusion coefficients at 400 °C are suspected to be much lower than the obtained upper limit because no radiation damage enhanced diffusion, which is often a few magnitudes higher than the diffusion in defect free crystals, was observed.

7.4.3. HOT IMPLANTATION

The channeling spectra for indium phosphide after implantation of 5×10^{16} Al^+ cm^{-2} at T_i = 250 °C are displayed in Fig. 45. A complete amorphisation in the surface region, as it was observed after the room temperature implantation, did not occur during implantation at T_i = 250 °C. Radiation-induced disorder in the surface region annealed out already during implantation. When comparing the dechanneling yield beyond the surface with the results from the hot aluminium implantation into gallium arsenide in Fig. 38, it is obvious that the slope in indium phosphide is constant from the surface. A fully recovered surface layer was not observed. Apparently a constant defect density is present that reaches from the surface to a depth of about 340 *nm*. This depth is about 1.5 times deeper than the predicted defect range (see Fig. 43). From the shape of the slope of the dechanneling yield, as well as from the fact that no regrowth occurs during annealing at 400 °C, it is obvious that a dense and stable dislocation network is present to a depth of approximately 340 *nm* below the surface.

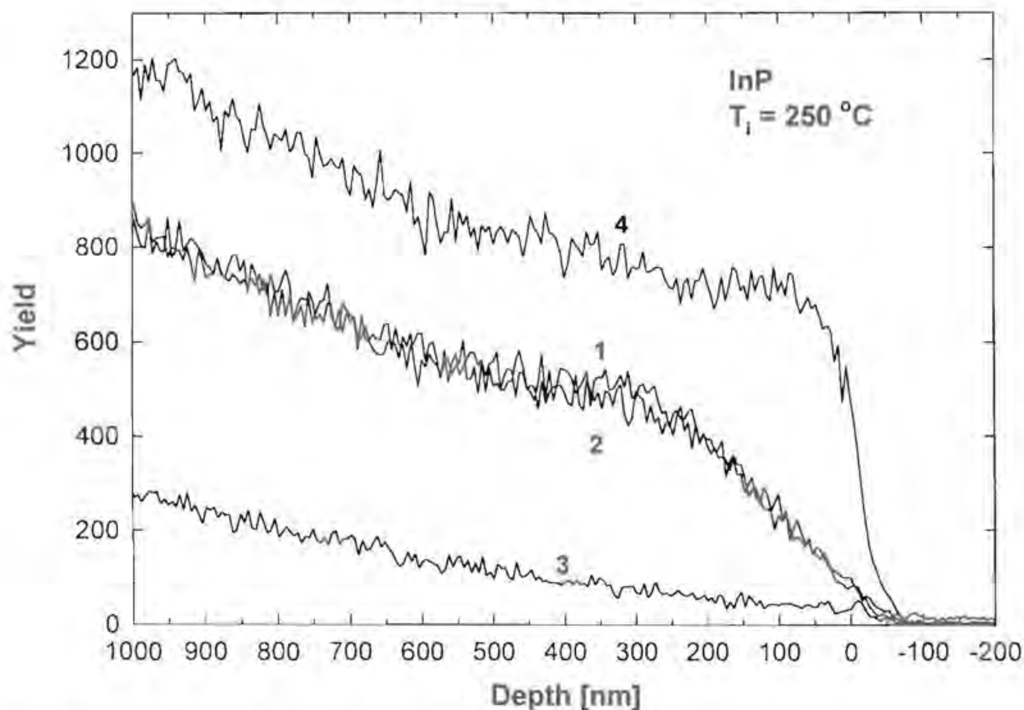

Fig. 45: Aligned backscattering spectra of indium phosphide implantation of 5×10^{16} Al^+ cm^{-2} at T_i = 250 °C before (1) and after annealing for one hour at 400 °C (2). Also given are aligned (3) and random spectra of unimplanted samples; α - particle energies have been converted to a depth scale.

Aluminium depth profiles before and after annealing for one hour at T_a = 300 and 400 °C are displayed in Fig. 46. The mean range of the as-implanted aluminium atoms is at a depth of R_p = 109 ± 10 *nm* with a second range moment of ΔR_p= 58 ± 4 *nm*. This is well within experimental error of the range moments obtained for the room temperature implantation. As no noticeable change occurs in the range moments of the room temperature implantation and the hot implantation, the upper limit of the radiation enhanced diffusion coefficients for our experimental parameters can be extracted to $D \leq 10^{-15}$ cm^2 s^{-1}.

After annealing for one hour at T_a = 300 °C the mean range of the implanted aluminium atoms was unchanged at R_p = 109 ± 10 *nm* with a second range moment of ΔR_p= 56 ± 4 *nm*. The range moments of the implanted aluminium atoms extracted after annealing for one hour at T_a = 400 °C were at R_p = 114 ± 10 *nm* with a second range moment of ΔR_p= 55 ± 4 *nm*. No visible diffusion to the surface occurred. An upper limit for the diffusion coefficient $D \leq 10^{-15}$ cm^2 s^{-1} was obtained for 400 °C.

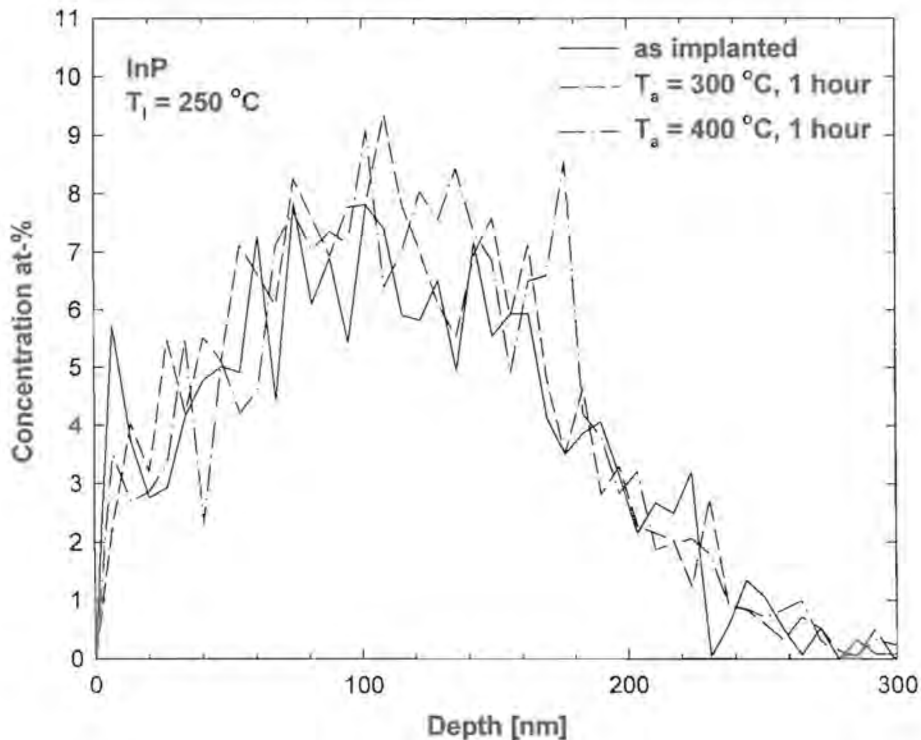

Fig. 46: Depth profiles of aluminium implanted at T_i = 250 °C with a fluence of 5 x 10^{16} cm^{-2} into indium phosphide before and after annealing for one hour at different temperatures T_a.

Sample **Indium phosphide**	**Range** R_p **[nm]**	**Straggling** ΔR_p **[nm]**	**Thermal diffusion coefficient** D **[$cm^2 s^{-1}$]**
$T_i = RT$, as-implanted	117 ± 10	56 ± 4	-
$T_i = RT$, $T_a = 300$ °C	113 ± 10	55 ± 4	$\leq 10^{-15}$
$T_i = RT$, $T_a = 400$ °C	108 ± 10	55 ± 4	$\leq 10^{-15}$
$T_i = 250$ °C, as implanted	109 ± 10	58 ± 4	-
$T_i = 250$ °C, $T_a = 300$ °C	109 ± 10	56 ± 4	$\leq 10^{-15}$
$T_i = 250$ °C, $T_a = 400$ °C	114 ± 10	55 ± 4	$\leq 10^{-15}$

Table 7: Summary of the experimental range parameters and thermal diffusion coefficients of 5×10^{16} aluminium ions cm^{-2} implanted into indium phosphide.

7.5. INDIUM ANTIMONIDE

The last compound semiconductor investigated for this study was indium antimonide. This material is used for infrared detectors in the 3-5 μm wavelength range. Several studies on implantations of several elements and the resulting radiation induced damage were published previously (see chapter 6.2.3.). However, results on aluminium diffusion in indium antimonide were not found in the literature. It is important to know the behaviour of an impurity in a semiconductor under different conditions for stability predictions.

Indium antimonide is a *III-V* compound semiconductor with a melting point of T_m = 525 °C. However, at this temperature the antimony evaporates, leaving only liquid indium [99]. The eutectic temperature of this binary system is at T_e = 494 °C [100], but already at lower temperatures ($T_a \approx$ 400 °C) a surface oxidation should be prevented by annealing the compound in a nitrogen or argon ambient [101]. Due to the unavailability of a facility for anneals under protective gas flow we had to stay well below this temperature. For this investigation the in-diffusion of aluminium into indium antimonide, as well as the diffusion behaviour of implanted aluminium within this compound semiconductor was investigated at an annealing temperature of T_a = 300 °C in vacuum.

7.5.1. ALUMINIUM DIFFUSION INTO INDIUM ANTIMONIDE

The aluminium diffusion into indium antimonide was investigated at an annealing temperature of T_a = 300 °C. A 12 ± 4 *nm* aluminium film was deposited onto a quarter of a clean indium antimonide wafer. Samples cut from this piece were annealed for one hour at T_a = 300 °C. The depth profiles of the deposited aluminium film before and after annealing are shown in Fig. 47.

A slight difference in the film thickness of about $\Delta d \approx 4$ *nm* is observed. These variations in film thickness are just at the experimental detection limit of the system. The difference refers to only a few monolayers of aluminium, which is probably due to inhomogeneities during vapour depositing the aluminium film over the lateral spread of the sample.

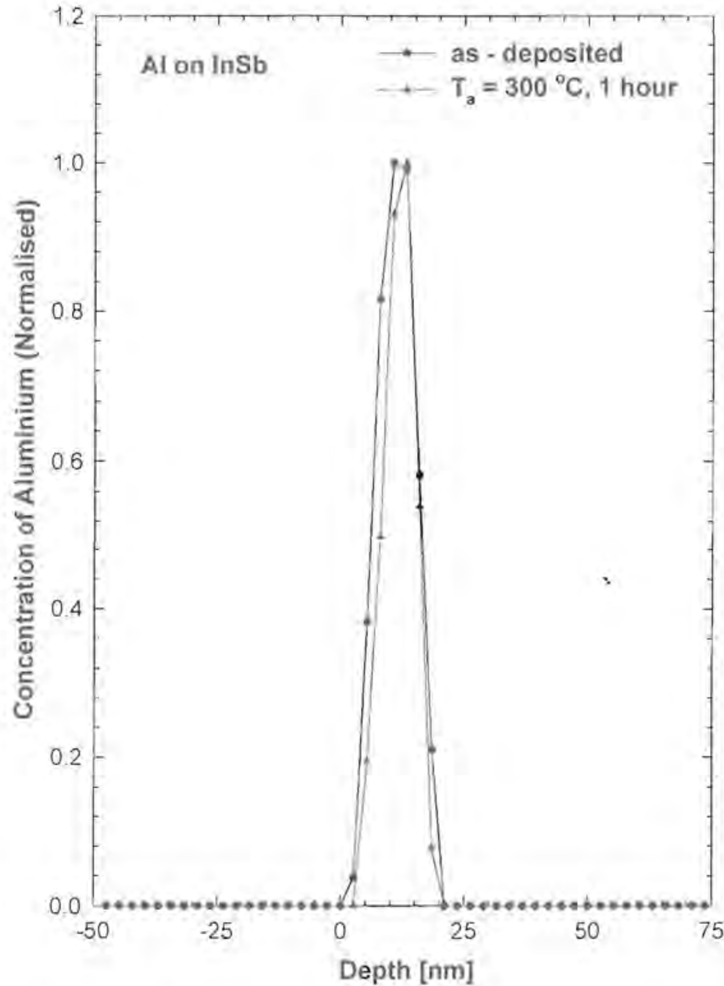

Fig. 47: Depth profiles of a vapour deposited aluminium layer on indium antimonide before and after annealing for one hour at $T_a = 300$ °C.

Results from the in-diffusion analysis are obtained from a possible change in width of the interface between the aluminium film and the indium antimonide substrate before and after annealing. After annealing the width remains within experimental error at 4 *nm*. Therefore the interface between the aluminium layer and the indium antimonide remains sharply defined after annealing for one hour at a temperature of T_a = 300 °C. The aluminium in-diffusion is obviously below the detection limit for our analysing method. An upper limit for the diffusion coefficient at $D \leq 10^{-16}$ cm^2 s^{-1} at 300 °C was extracted.

However, the actual aluminium diffusion coefficients at his temperature could be slightly higher than this upper limit due to native oxide layers that form at the interface before deposition of the aluminium film, and which can act as diffusion barriers [102]. In order to

bring the diffusant aluminium into direct contact with the indium antimonide, e.g. without such a diffusion barrier, it was implanted into the sample.

7.5.2. ROOM TEMPERATURE IMPLANTATION

A heavy dose ion implantation, which exceeds (3-5) x 10^{15} ions cm^{-2}, creates an irreversible structural damage in the indium antimonide crystal [86]. The observed swelling of indium antimonide after ion implantation is due to the formation of a large number of pores where the single crystal structure degraded dramatically. However, for analysis by NRA the fluence of implanted aluminium has to be high enough in order to have a moderate fluence of analysing protons combined with a high enough counting efficiency. Therefore we implanted 5 x 10^{16} aluminium ions cm^{-2} at room temperature into indium antimonide for the present study. No channeling effect was observed because of the loss of crystallinity at such a high fluence.

The depth profiles of 5 x 10^{16} aluminium ions cm^{-2} implanted into indium antimonide at room temperature before and after annealing for one hour at T_a = 300 °C are shown in Fig. 48. The experimentally obtained mean range of the implanted aluminium ions before annealing was at R_p = 115 ± 10 *nm* and the second range moment at ΔR_p= 63 ± 5 *nm*.

During annealing for one hour at T_a = 300 °C the mean range of the aluminium atoms in the indium antimonide stayed unchanged at R_p= 116 ± 10 *nm*. No change was observed in the second range moment at ΔR_p= 64 ± 5 *nm*.

Aluminium diffusion to the surface as in the case of the investigated elemental semiconductors was not observed with this compound semiconductor. Obviously the implanted aluminium atoms are still inside the highly disordered indium antimonide lattice. While in the elemental semiconductors silicon and germanium a defect enhanced diffusion was noted, such an enhancement was not observed in the investigated temperature range. One of the reasons, that there is no aluminium out-diffusion might be that SbAl and InSb are miscible in all proportions [103], to form (AlIn) Sb.

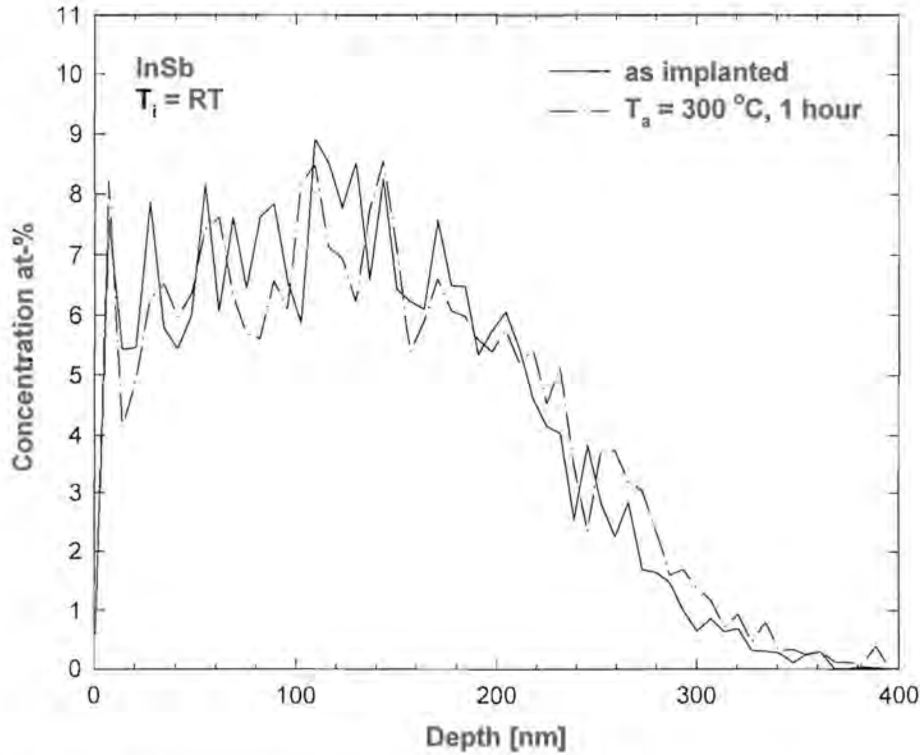

Fig. 48: Depth profiles of aluminium implanted at room temperature into indium antimonide before and after annealing for one hour at T_a = 300 °C.

Sample Indium antimonide	Range R_p [*nm*]	Straggling ΔR_p [*nm*]	Thermal diffusion coefficient D [$cm^2\ s^{-1}$]
$T_i = RT$, as-implanted	115 ± 10	63 ± 5	-
$T_i = RT$, T_a = 300 °C	116 ± 10	64 ± 5	$\leq 10^{-15}$

Table 8: Summary of the experimental range parameters and thermal diffusion coefficients of implanted aluminium into indium antimonide.

As no detectable diffusion occurred an upper limit for the diffusion coefficient at $D \leq 10^{-15}$ $cm^2\ s^{-1}$ for 300 °C was extracted. A summary of the diffusion analysis after the room-temperature implantation is listed in table 8. The obtained result is consistent with the one obtained for the aluminium in-diffusion investigation. As no diffusion was observed, we

expect the diffusion coefficient at this temperature to be much lower than the upper limit given here due to the radiation induced damage, which in the case of the elemental semiconductors enhanced the diffusion by several magnitudes.

7.5.3. HOT IMPLANTATION

After implantation of 5 x 10^{16} aluminium ions cm^{-2} at 250 °C a discolouring of the surface of the indium antimonide samples was observed. The surface appeared to be black. A surface discolouring of indium antimonide after implantation was already reported in ref. [88].

Aluminium depth profiles before and after annealing for one hour at T_a = 300 °C are displayed in Fig. 49. The shape of the implanted aluminium atoms changed dramatically during implantation at T_i = 250 °C in comparison to the room temperature implantation. The aluminium depth distribution is not gaussian anymore. The voids formed in the thermal spike of the collision cascade probably could cause the aluminium out-diffusion already during the implantation [88]. However, such a void formation would then be already expected after the room temperature implantation. We rather suspect that the outdiffusion occurs via vacancies created by an antimony loss from the surface. The loss occurs during the hot implantation and shifts this compound during annealing to a two-phase region above 157 °C, with a liquid phase containing mainly indium and the remaining solid phase [100]. After cooling the compound to room temperature an indium rich crystal remains. Considering an excess of indium with its high affinity for oxygen, the formation of In_2O_3 is expected to be responsible for the change of colour. Implanted indium antimonide surfaces are reported to oxidise easily [101]. It must be stressed, however, that a surface discolouring was not observed after the room temperature implantation.

As the aluminium depth profiles have no gaussian shape the calculation of the range moments makes no sense.

After annealing for one hour at T_a = 300 °C more aluminium diffused out of the sample as displayed in Fig. 48. This diffusion probably takes place via the above mentioned vacancies that are created by the antimony loss from the surface. Such an enhanced diffusion was not observed after the room-temperature implantation at 300 °C.

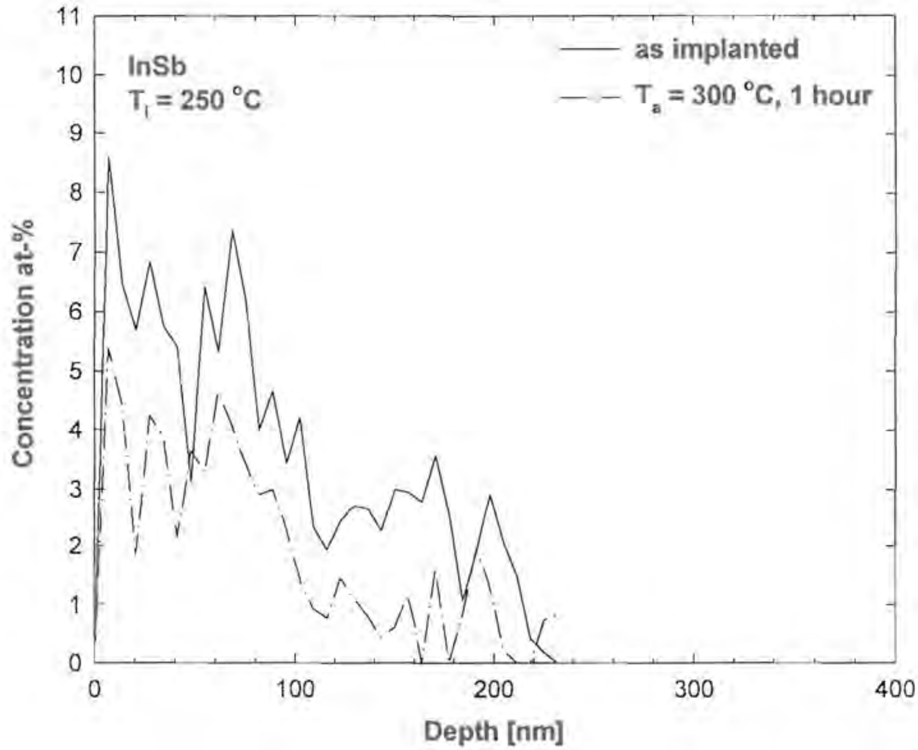

Fig. 49: Depth profiles of aluminium implanted at $T_i = 250$ °C with a fluence of 5 x 10^{16} cm^{-2} into indium antimonide before and after annealing for one hour at $T_a = 300$ °C.

A calculation of the aluminium diffusion coefficient does not make sense for the hot implantation because it will be much too large compared to the expected coefficient in an undisturbed indium antimonide crystal at 300 °C.

CHAPTER 8

SUMMARY OF RESULTS

Aluminium diffusion was investigated by NRA in five different semiconductors. Different experimental methods were employed. For in-diffusion investigation thin aluminium films were deposited onto the specimen followed by subsequent annealing. Aluminium diffusion within the investigated semiconductors was analysed after implantations at room temperature and T_i = 250 °C followed by subsequent annealing. The diffusion coefficients obtained were compared with previously reported results when available.

No aluminium in-diffusion was observed into any of the studied semiconductors. From this it can be concluded that within the respective temperature range aluminium is a suitable contact material for the investigated semiconductors.

From the diffusion enhancement of aluminium in the highly damaged elemental semiconductors silicon and germanium it can be concluded that the diffusion occurs via a vacancy mechanism in these materials as already suggested by *Seeger* et al. [8].

8.1. SILICON

The in-diffusion of aluminium into Si<100> at temperatures ranging from 500 °C to 900 °C has been investigated. Coefficients expected from previously published results are extrapolated to these temperatures. An extrapolation was necessary because most of the reported results were obtained for temperatures above 1000 °C. At 900 °C a diffusion coefficient between $D = 1.3 \times 10^{-13}$ $cm^2\ s^{-1}$ and $D = 3 \times 10^{-15}$ $cm^2\ s^{-1}$ with an average value of $D = 4 \times 10^{-14}$ $cm^2\ s^{-1}$ is expected. Higher annealing temperatures in our vacuum system were avoided after complete oxidation of the thin aluminium film was observed during annealing at T_a = 1000 °C.

No detectable aluminium in-diffusion was observed at any stage and an upper limit for the diffusion coefficient at $D \leq 10^{-16}$ $cm^2\ s^{-1}$ was obtained for 900 °C, which is significantly

smaller than expected from the literature. However, a native layer of SiO_2 that forms instantaneously after cleaning the silicon surface before depositing the aluminium film acts as a diffusion barrier and thus reduces the diffusion during annealing. Therefore the actual diffusion coefficient is expected to be higher and could be in the interval calculated from the literature.

Aluminium diffusion within Si<100> and Si<111> was investigated after implantations at room temperature and at T_i = 250 °C with subsequent annealing for one hour at temperatures up to T_a = 900 °C. By comparing aluminium depth profiles for room temperature implantation and for implantation at T_i = 250 °C, radiation enhanced diffusion for our implantation parameters has been calculated to be smaller than $D \leq 10^{-15}$ cm^2 s^{-1}.

The room temperature implantation resulted in a highly disordered region that did only recover partly during annealing for one hour at T_a = 900 °C. An enhanced diffusion of the aluminium atoms to the surface was observed due to radiation induced damage. Complete aluminium out diffusion to the surface was observed at this temperature. The obtained diffusion coefficients at 900 °C are two to three orders of magnitude larger than those obtained for the implantation at T_i = 250 °C. However, they are in the same range as some of the published coefficients as seen in Fig. 28. We therefore believe that some of the higher results reported in the literature are due to defect enhanced diffusion. Our diffusion results after room temperature implantations are furthermore in accordance with the reported poor electrical activation due to out-diffusion and precipitation of Al_2O_3 at the surface after annealing at T_a > 900 °C [63-69].

After implantation at T_i = 250 °C radiation induced damage in the surface region was largely avoided and the aluminium-rich implantation region was bordered by a nearly defect-free surface region and the highly crystalline bulk. An upper limit for the diffusion coefficient at $D \leq 10^{-15}$ cm^2 s^{-1} was obtained for 900 °C, which is significantly smaller than the smallest coefficients reported in the literature. It does not contradict our results obtained for in-diffusion.

During annealing the hot implanted silicon sample at T_a = 900 °C two phases are expected in the implanted depth [55]. In a silicon depth of 200 *nm* we measured a maximum of about 5

at.% of aluminium. For this maximum density about 8 % of the compound is in the liquid phase, consisting of 37 % silicon and 63 % aluminium. The remaining 92 % in the solid phase consist mainly of silicon due to the low solubility of aluminium at this temperature. When cooling the sample down to room temperature aluminium segregates from the liquid [64].

8.2. GERMANIUM

The in-diffusion of aluminium into germanium at temperatures of 500 °C and 700 °C has been investigated. As expected diffusion coefficients from the literature are below our detection limit at 500 °C only the coefficients at 700 °C are extracted. No detectable diffusion is observed at any stage. From this we calculated an upper limit for the diffusion coefficient of $D \leq 10^{-16}\ cm^2\ s^{-1}$ at 700 °C. This coefficient is about a magnitude lower than both previously reported coefficients $D = 1.2 \times 10^{-15}\ cm^2\ s^{-1}$ [71] and $D = 2.4 \times 10^{-15}\ cm^2\ s^{-1}$ [72]. These coefficients at 700 °C were measured by *Dorner* et al. [71], whereas the results by *Meer* et al. [72] were extrapolated from higher temperatures. Our upper limit for the diffusion coefficient is probably too low due to a thin native oxide layer that forms instantaneously after cleaning the germanium surface before depositing the aluminium film. This oxide layer forms a diffusion barrier and therefore lowers the extracted upper limit for the coefficient.

Aluminium diffusion within germanium was investigated after implantations at room temperature and to $T_i = 250$ °C with subsequent annealing for one hour at temperatures up to $T_a = 700$ °C. From comparing the aluminium depth profiles after room temperature implantation with those after implantation at $T_i = 250$ °C, an upper limit for the radiation enhanced diffusion was calculated at $D \leq 10^{-15}\ cm^2\ s^{-1}$ for our implantation parameters, by taking into account the implantation time.

Channeling effects of α-particles were not observed in the implanted germanium samples due to a rather high dechanneling yield in the samples already before the implantation. However, when comparing the aluminium diffusion results in germanium with the results from the silicon investigation similarities are observed.

A comparison with the results obtained for the silicon implantation indicates that the room temperature implantation also resulted in an amorphous surface region that did only recover partly during annealing for one hour at T_a = 500 °C and T_a = 700 °C. Aluminium diffusion to the surface was observed after T_a = 500 °C due to radiation induced defects. Most aluminium atoms diffused out of the sample to the surface during T_a = 700 °C. The diffusion coefficient after room-temperature implantation is about two orders of magnitude larger than coefficients reported previously. However, the obtained diffusion coefficients are much too high due to the large amount of defects in the surface region and can therefore not be compared with coefficients expected in defect free germanium.

After implantation at T_i = 250 °C it appears from the similarity with the silicon results, that radiation induced damage in the surface region was largely avoided. However, a channeling effect was not observed. One reason for this is probably due to the fact that the mass of germanium is much larger than the mass of silicon, which leads to denser collision cascades and a dislocation network already at T_i = 250 °C.

An upper limit of the diffusion coefficient at $D \leq 10^{-15}\ cm^2\ s^{-1}$ was obtained for 700 °C, which does not contradict the results by *Dorner* [71] and is slightly lower than the coefficient calculated from the results by *Meer* [72] (see Fig. 34).

From the binary phase diagram for the germanium aluminium system [70] it can be seen that at 700 °C two phases are formed in a germanium depth of 115 *nm*, where the aluminium reaches a maximum concentration of about 7 at.%. At this temperature about 17 % of the compound is in the liquid phase, consisting of 57 % germanium and 43 % aluminium. The solid phase consists mainly of germanium due to the low solubility of aluminium. When cooling the samples after annealing segregations of metallic aluminium are expected in the implanted depth.

8.3. GALLIUM ARSENIDE

The in-diffusion of aluminium into gallium arsenide at temperatures up to 500 °C was investigated. Expected diffusion coefficients at 500 °C are obtained when extrapolating the results from the literature in Fig. 18 to 773 K, which corresponds to a value on the abscissa of

1.3 and a diffusion coefficient of about $D \approx 10^{-30}$ cm^2 s^{-1}. The expected coefficient is therefore much lower than our upper detection limit. However, radiation induced defects accounted for a dramatic diffusion enhancement in the elemental semiconductors investigated in this study. This investigation was made to analyse if defects also play such an important role in the aluminium diffusion in gallium arsenide.

As in the case for the other investigated semiconductors no detectable aluminium in-diffusion into gallium arsenide is observed at any stage. An upper limit for the diffusion coefficient of $D \leq 10^{-16}$ cm^2 s^{-1} is extracted for 500 °C, which is expected from the literature.

The aluminium diffusion within gallium arsenide was investigated after implantations at room temperature and at T_i = 250 °C with subsequent annealing for one hour at temperatures up to T_a = 500 °C. When comparing the aluminium depth profiles after room temperature implantation and after implantation at T_i = 250 °C no difference could be detected. From this an upper limit of the radiation enhanced diffusion at $D \leq 10^{-15}$ cm^2 s^{-1} for our implantation parameters was extracted by taking into account the implantation time.

The room temperature implantation resulted in a highly disordered region. No channeling effect within the crystal was observed. No regrowth was observed after annealing at T_a = 400 °C for one hour. After annealing for one hour at T_a = 500 °C a channeling effect was observed in the crystal. However, the surface layer remained highly disordered. No aluminium diffusion through this highly disordered layer to the surface was observed. The upper limit of the aluminium diffusion coefficients for the room-temperature implantation is at $D \leq 10^{-15}$ cm^2 s^{-1}at 500 °C. For the elemental semiconductors a diffusion enhancement by a few orders of magnitude was observed. With an expected diffusion coefficient of about $D \approx 10^{-30}$ cm^2 s^{-1} defect enhanced diffusion by a few magnitudes could still take place without being detected by our method. The aluminium solubility in the investigated elemental semiconductors was very small which resulted in out diffusion from the room temperature implanted samples to the surface when annealing at elevated temperatures. When considering that the compounds AsAl and AsGa are completely miscible [105] and that the aluminium diffusion coefficient in gallium arsenide is strongly correlated to the gallium self-diffusion in this compound, then there is no aluminium out diffusion expected from the sample.

After implantation at T_i = 250 °C radiation induced disorder in the surface region was largely avoided as in the case of the elemental semiconductors. From the channeling spectra it is obvious that no amorphisation is present but the large slope of the dechanneling yield indicates a high density of extended defects.

A comparison of the aluminium depth profiles before and after annealing leads to the upper limit for the diffusion coefficient of $D \leq 10^{-15}$ cm^2 s^{-1} at 500 °C, which was expected.

8.4. INDIUM PHOSPHIDE

No previously reported results on the aluminium diffusion in indium phosphide were found in the literature. Predictions about the behaviour of this system are difficult for there are contradictory thermodynamic calculations of the aluminium solubility in this compound semiconductor [105]. Investigations in this study were performed up to 400 °C to avoid surface oxidation, which could influence the results.

Aluminium in-diffusion has been investigated at 400 °C by annealing thin aluminium films that were deposited onto clean indium phosphide substrates. The interface between the aluminium film and the indium phosphide substrate remained sharply defined after annealing. From this it was concluded that no detectable aluminium in-diffusion occurred at this temperature. An upper limit of the diffusion coefficient at $D \leq 10^{-16}$ cm^2 s^{-1} is extracted for 400 °C.

Aluminium diffusion within indium phosphide was investigated after implantations at room temperature and at T_i = 250 °C with subsequent annealing for one hour at temperatures up to T_a = 400 °C. The radiation enhanced diffusion for our implantation parameters, analysed by comparing the aluminium depth profiles for room temperature implantation and for implantation at T_i = 250 °C by taking into account the implantation time, was lower than our detection limit at $D \leq 10^{-15}$ cm^2 s^{-1}.

The room temperature implantation resulted in a highly disordered surface layer that reached much deeper into the crystal than the mean ranges of the implanted aluminium ions. A slight crystalline regrowth from the bulk is observed after annealing the compound for one hour at

T_a = 300 °C. No further regrowth was observed from a sample that was subsequently annealed for one hour at T_a = 400 °C.

Müller et al. [106] measured thicknesses of amorphous surface layers in indium phosphide after 80 and 180 *keV* silicon room temperature implantation to be 150 and 290 *nm*, respectively. These results are more in line with the calculated damage thicknesses of 121 *nm* and 261 *nm* for these energies. However, their implantation parameters were rather different to ours, e.g. their dose rates were at 3 x 10^{11} ions cm^{-2} s^{-1}, which is more than thirty times lower and the fluences were at about 10^{14} ions cm^{-2}, which is about five hundred times lower than the parameters for this study. However, tail effects can be excluded as the reason for the observed enhancement in the damage depth when considering the measured aluminium depth profiles.

The aluminium depth profiles are unchanged before and after annealing for one hour at T_a = 400 °C. It was concluded that no detectable aluminium diffusion to the surface occurred. The diffusion coefficients in this case are also lower than our detection limit at $D \leq 10^{-15}$ cm^2 s^{-1}. We suspect a high aluminium solubility in indium phosphide after considering the aluminium out diffusion through highly damaged layers in elemental semiconductors where its solubility is low. The behaviour of this system is similar to the one observed for the Al-GaAs system, where the components were completely miscible in one other.

During implantation at T_i = 250 °C a different defect type is observed. The introduced damage reached about 1.5 times deeper than predicted from simulations and consists of a dense network of dislocations. No change in the dislocation density was observed during annealing for one hour at T_a = 400 °C.

The shape of the aluminium depth profile did not change before and after annealing for one hour at T_a = 400 °C. An upper limit for the diffusion coefficient at $D \leq 10^{-15}$ cm^2 s^{-1} was extracted at 400 °C, which agrees well with the results obtained for the room temperature implantation and does not contradict the result obtained from the in-diffusion analysis.

8.5. INDIUM ANTIMONIDE

Previously reported results on aluminium diffusion in indium antimonide were not found. SbAl and InSb are miscible in all proportions to form (AlIn)Sb over most of the system [107]. From this fact very small diffusion coefficients are expected for this system.

For recording a NRA depth profile we had to implant high doses of at least 5 x 10^{16} aluminium ions cm^{-2}, to obtain a sufficient count rate in a reasonable analysing time. Longer analysing times bear the danger that target degradation occurs due to the analysing beam. Already relatively low ion fluences cause amorphisation of the indium antimonide target, where no α-particle channeling effect could be observed for the implanted samples.

Aluminium diffusion into indium antimonide was investigated after deposition of a thin aluminium film onto this compound followed by annealing at T_a = 300 °C. The interface between the aluminium film and the substrate remained unchanged before and after annealing. It was concluded that no detectable aluminium in-diffusion occurred at 300 °C. An upper limit for the aluminium diffusion coefficient at 300 °C is extracted to $D \leq 10^{-16}\ cm^2\ s^{-1}$.

Aluminium diffusion within indium antimonide was investigated after implantations at room temperature and at T_i = 250 °C with subsequent annealing for one hour at a temperatures of T_a = 300 °C. A comparison of the aluminium depth profiles after room temperature implantation and after implantation at T_i = 250 °C revealed a dramatic difference. The depth profile after the hot implantation did not have a gaussian shape (Fig. 49), which was observed after the room-temperature implantation (Fig.48). Obviously aluminium atoms diffused out already during the hot implantation.

Annealing the room temperature implanted indium antimonide sample for one hour at T_a = 300 °C did not change the depth profile of the implanted aluminium. An enhanced aluminium diffusion to the surface due to radiation induced defects was not observed after annealing. Since no aluminium diffusion is detected an upper limit for the diffusion coefficients at 300 °C is $D \leq 10^{-15}\ cm^2\ s^{-1}$.

A black discolouring of the sample surface was observed after the hot implantation, which is suspected to be the result of antimony loss from the surface during the implantation. Such an antimony loss leads to a phase transition with a liquid phase consisting mainly of indium (above 155 °C). When cooling down, an oxide layer (In_2O_3) can form on the surface [88]. Annealing a hot aluminium implanted indium antimonide sample for one hour at T_a = 300 °C results in aluminium out diffusion, which can also be explained with the antimony loss from the sample and the resulting vacancies that can enhance the diffusion.

8.6. OUTLOOK

The diffusion results in this study were obtained by NRA. A relatively high dose of aluminium has to be implanted to obtain depth profiles with a reasonable counting efficiency for a proton fluence that does not degrade the target surface. One possibility to increase the counting efficiency would be by replacing the intrinsic germanium detector with a second NaJ detector. This would enable our system to measure lower aluminium concentrations within a reasonable fluence of protons.

Another interest for future research lies in investigating the damage introduced into some of the semiconductors during hot implantation, which reveals a much deeper damage than expected from TRIM calculations. Damage ranges that are much deeper than the mean ranges of the implanted ions was previously only reported for metal targets [93], whereas in semiconductors the damage was usually found in the depth of the mean range [108]. A fluence and implantation temperature dependent investigation of this effect is intended.

APPENDIX A

Listing of the batch Program for the PCA Multiport multichannel analyser to save spectra automatically after a predefined number of energy scans. The 'preset passes' sets the number of scans after which to save. The number after 'loop begin' tells how often to save. In the example below 10 scans are acquired the spectrum of each scan is saved. The filenames are numbered and incremented before saving. As an optional feature it is possible to save the files under the same name by not incrementing the file number. This batch program has to be compiled with the build in compiler before it can be started.

```
CONFIRM   "START OF NRA, PRESS ANY KEY TO CONTINUE."
COLLECT   "PLEASE ENTER FILENAME: " %F TONE LEN 7

MCS EXTERNAL          ; EXTERNAL DWELL
SYNC EXTERNAL
LOOP BEGIN 10         ; THIS NUMBER TELLS HOW OFTEN TO SAVE
 ACQUIRE
 PRESETS  ON
 PRESET PASSES 1       ; THIS NUMBER TELLS AFTER HOW MANY SCANS TO SAVE
 WAIT                  ; WAIT FOR PRESETS TO ELAPSE
 STEP FILENAME 1       ; INCREMENT THE FILENAME BY ONE NUMBER
 ID %F                 ; UPDATE THE ID STRING
 SAVE %F OVERWRITE ; SAVE THE DATA TO A BINARY DISK FILE
LOOP END

STOP

CONFIRM "END OF NRA ACQUISITION, STRIKE ANY KEY TO CONTINUE."
```

REFERENCES

[1] W.C. Roberts-Austen, Phil. Trans. Roy. Soc. (London), A 187 (1896) 404.

[2] L.W. Barr, Defect and Diffusion Forum, 143-147 (1997) 3.

[3] C. Tuijn, Defect and Diffusion Forum, 143-147 (1997) 11.

[4] K.N. Tu, Ann. Rev. Mater. Sci., 15 (1985) 147.

[5] A. Fick, Ann. Phys. Lpz., 170 (1855) 59.

[6] A. Fick, Phil. Mag., 10 (1855) 30.

[7] R.M. Barrer, Diffusion in and through solids, Cambridge press, Cambridge England, (1951) 3.

[8] A. Seeger and P.K. Chik, Phys. Stat. Sol, 29 (1968) 455.

[9] S.J. Pearton, Int. Journ. of Mod. Phys. B, Vol 7, 28 (1993) 4687.

[10] J. Crank, The Mathematics of Diffusion, 2nd ed. , Clarendon Press, Oxford, (1975) 186.

[11] J.R. Kaschny, private communication.

[12] D. Fink, R. Klett, M. Behar, G. Sànchez, J.R. Kaschny, and W.G. Hertlein, Nucl. Inst. and Meth., B132 (1997) 660.

[13] J.R. Tesmer and M. Nastasi, Handbook of Modern Ion Beam Materials Analysis, Mat. Res. Soc. Pittburgh, Pennsylvania, (1995) 5.

[14] J.P. Biersack and L.G. Haggmark, Nucl. Instr. and Meth., 174 (1980) 257.

[15] S. Kalbitzer and H. Oetzmann, Phys. Lett., 59A (1976) 197.

[16] J.F. Ziegler, J.P. Biersack and U. Littmark, The Stopping and Ranges of Ions in Matter (Vol.1), Pergamon Press, New York, (1985).

[17] J.P. Biersack and J.F. Ziegler, in Ion Implantation Techniques, ed. H. Ryssel and H. Glawischnig, Springer Verlag Berlin, (1982) 148.

[18] J. Lindhard and M. Scharff, K. Dan. Vidensk. Selsk. Mat. Fys. Medd., 27 (1953) No.15.

[19] J. Lindhard and M. Scharff, Phys Rev. 124 (19961) 128.

[20] J. Lindhard, M. Scharff,and H.E. Schiott, K. Dan. Vidensk. Selsk. Mat. Fys. Medd., 33 (1961) No.14.

[21] N. Bohr, Phil. Mag., 25 (1913) 10.

[22] H.A. Bethe, Ann. Phys., 5 (1930) 325.

[23] F. Bloch, Ann. Phys., 16 (1933) 285.

[24] H. Bichsel, ICRU Report, 37 (1984).

[25] N. Bohr, Phys. Rev., 58 (1940) 654.

[26] N. Bohr, Phys. Rev., 59 (1941) 270.

[27] J.F. Ziegler and J.M. Manoyan, Nucl. Inst. and Meth., B35 (1988) 215.

[28] W.K. Chu, J.W. Mayer and M.A. Nicolet, Backscattering Spectrometry, Academic Press, New York (1978) 45.

[29] N. Bohr, Mat. Fys. Medd. Dan. Vid. Selsk, 18 (1948) 8.

[30] N. Bohr, Mat. Fys. Medd. Dan. Vid. Selsk, 24 (1948) 19.

[31] J.R. Tesmer and M. Nastasi, Handbook of Modern Ion Beam Materials Analysis, Mat. Res. Soc., Pittburgh, Pennsylvania, (1995) 37.

[32] T. Mayer-Kuckuck, Kernphysik, Teubner Verlag, (1984) 344.

[33] J.M. Blatt and V.F. Weisskopf, Theoretical Nuclear Physics, John Wiley and Sons Inc., New York, (1952).

[34] T. Mayer-Kuckuck, Kernphysik, Teubner Verlag, (1984) 99.

[35] J.R. Tesmer and M. Nastasi, Handbook of Modern Ion Beam Materials Analysis, Mat. Res. Soc., Pittburgh, Pennsylvania, (1995) 170.

[36] E. Friedland, Nucl. Inst. and Meth., 150 (1978) 301.

[37] G.Amsel, J.P. Nadai, E. d'Artemare, D. Davis, E. Girard and J. Moulin, Nucl. Instr. and Meth., 92 (1971) 418.

[38] G. Amsel, E. d'Artemare and E. Girard, Nucl. Inst. and Meth., 191 (1981) 189.

[39] G. Amsel, E. d'Artemare and E. Girard, Nucl. Inst. and Meth., 205 (1983) 5.

[40] The Energy Scanning System of the University of Pretoria, Users Manual (1993).

[41] M.Hayes, PhD Thesis, University of Pretoria, (1995) 38.

[42] J.R. Tesmer and M. Nastasi, Handbook of Modern Ion Beam Materials Analysis, Mat. Res. Soc., Pittburgh, Pennsylvania, (1995) 186.

[43] J.R. Tesmer and M. Nastasi, Handbook of Modern Ion Beam Materials Analysis, Mat. Res. Soc., Pittburgh, Pennsylvania, (1995) 173.

[44] I. Vickbridge and G. Amsel, Nucl. Inst. and Meth., B45 (1990) 16.

[45] M.Hayes, PhD Thesis, University of Pretoria, (1995) 47.

[46] M.A. Meyer and N.S. Wolmarans, Nucl. Phys., A136 (1969) 663.

[47] L.C. Feldman and J.W. Mayer, Fundamentals of Surface and Thin Film Analysis, Elsevier Science Publishing, New York, (1986) 100.

[48] D.S. Gemmel, Rev. Mod. Phys., 46 (1974) 129.

[49] L.C. Feldman, J.W. Mayer and S.T. Picraux, Material Analysis by Ion Channeling, Academic Press, New York, (1982).

[50] D.V. Morgan, Channeling, John Wiley and Sons, New York, 1973.

[51] W.K. Chu, J.W. Mayer and M.A. Nicolet, Backscattering Spectrometry, Academic Press, New York (1978) 223.

[52] J.R. Tesmer and M. Nastasi, Handbook of Modern Ion Beam Materials Analysis, Mat. Res. Soc., Pittburgh, Pennsylvania, (1995) 231.

[53] T. Hauser, Diplomarbeit, Karlsruhe, (1993) 20.

[54] S.M. Myers, S.T. Picraux and T.S. Prevender, Phys. Rev. B9, 10 (1974) 3953.

[55] J.L. Murray and A.J. McAllister, Bull. Alloy Phase Diagrams, 5(1) Feb. 1984, in: Binary Alloy Phase Diagrams, Ed. T.B Massalski, J.L. Murray, L.H.Bennett and H. Baker, Am. Soc. for Metals, Ohio, (1986) 164.

[56] D. de Cogan, in: Properties of Silicon, EMIS Datareviews Series No 4, INSPEC, (1988) 337.

[57] C.S. Fuller and J.A. Ditzenberger, J. Appl. Phys., 27 (1956) 544.

[58] B.Goldstein, Bull. Am. Phys. Soc. Ser. II, 1 (1956)145.

[59] R.C. Miller and A. Savage, J. of Appl. Phys., 27 (1956) 1430.

[60] Y.C. Kao, Electrochem. Technol., 5 (1967) 90.

[61] R.N. Goshtagore, Phys. Rev. B, 3 (1971) 2507.

[62] W. Rosnowski, J. Electrochem. Soc., 125 (1978) 957.

[63] G. Galvagno, F. La Via, F. Priolo and E. Rimini, Semicond. Sci. Technol., 8 (1993) 488.

[64] A. La Ferla, L. Torrisi, G. Galvagno, E. Rimini, G. Ciavola, A. Carnera and A. Gasparotto, Appl. Phys. Lett., 62 (1993) 393.

[65] P. Brüesch, E. Halder, P. Kluge, J. Rhyner, P. Roggwiller, Th. Stockmeier, F. Stucki and H.J. Wiesmann, J. Appl. Phys., 68 (1990) 2226.

[66] H.R. Chang, N. Lewis, G.A. Smith E.L. Hall and V.A.K. Temple, J. Electrochem. Soc., 135 (1988) 252.

[67] M. Watanabe, O. Ishiwata, M. Nagano and H. Kirihata, J. Electrochem. Soc., 138 (1991) 3427.

[68] U. Kuhlmann, D. Nagel and R. Dittig, Defect and Diff. Forum, 143-147 (1997) 1009.

[69] R. Baron, G.A. Shifrin, O.J. Marsh and J.W. Mayer, J. Appl. Phys, 40 (1969) 3702.

[70] A.J. McAllister and J.L. Murray, Bull. Alloy Phase Diagrams, 5(4) Aug. 1984, in: Binary Alloy Phase Diagrams, Ed. T.B Massalski, J.L. Murray, L.H.Bennett and H. Baker, Am. Soc. for Metals, Ohio, (1986) 117.

[71] P. Dorner, W. Gust, A. Lodding, H. Odelius, B. Predel and U. Roll, Acta Metall., 30 (1982) 941.

[72] W. Meer and D. Pommerrenig, Z. angew. Phys., 23 (1967) 369.

[73] U. Gösele, T.Y. Tan, M. Schultz, U.Egger, P. Werner, R. Scholz and O. Breitenstein, Defect and Diff. Forum, 143-147 (1997) 1079.

[74] L.L. Chang and A. Koma, Appl. Phys. Lett., 29 (1976) 138.

[75] T.E. Schlesinger and T. Kuech, Appl. Phys. Lett., 49 (1986) 519.

[76] P. Mei, H.W. Yoon, T. Venkatesan, S.A. Schwarz and J.P. Harbison, Appl. Phys. Lett., 50 (1987) 1823.

[77] L. Wang, L. Hsu. E.E. Haller, J.W. Erickson, A. Fischer, K. Eberl and M. Cardona, Phys. Rev. Lett., 76 (1996) 2342.

[78] B. Goldstein, Phys. Rev., 121 (1961) 1305.

[79] P.M. Petroff, J. Vac. Sci. Technol., 14 (1977) 973.

[80] R.M. Fleming, D.B. McWhan, A.C. Gossard, W. Wiegmann and R.A. Logan, J. Appl. Phys., 51 (1980) 357.

[81] H.D. Palfrey, M. Brown and A.F.W. Willoughby, J. Electrochem. Soc., 128 (1981) 2224.

[82] T.Y. Tan, U. Gösele and S. Yu, Crit. Rev. Solid State Mater. Science, 17 (1991) 47.

[83] A. Yamada, Y. Makita, K.M. Mayer, T. Iida, H. Yoshinaga, S. Kimura, S. Niki, H. Shibata, S. Uekusa and T. Matsumori, Nucl. Inst. and Meth., B80/81 (1993) 910.

[84] D.E. Davis, J. of Crystal Growth, 54 (1981) 150.

[85] E. Michel, H. Mohseni, J.D. Kim, J. Wojkowski, J. Sandven, J. Xu, M. Razeghi, R. Bredthauer, P. Vu, W. Mitchel and M. Ahoujja, Appl. Phys. Lett., 71 (1997) 1071.

[86] P. Martin, E. Ligeon and J.P. Gailliard, Nucl. Inst and Meth., 197 (1982) 47.

[87] V.K. Vasil'ev, O.N. Gorshkov, Y.A. Danilov and V.S. Tulovchikov, Sov. Phys. Solid State, 25 (1983) 118.

[88] G.L. Destefanis, J.P. Belle, J.M. Ogier-Collin and J.P. Gailliard, Nucl. Inst. and Meth., 182/183 (1981) 637.

[89] D.V. Morgan, F.H. Eisen and A. Ezis, IEE Proc., 128 (1981) 109.

[90] M. Hansen, in: Binary Alloy Phase Diagrams, Ed. T.B Massalski, J.L. Murray, L.H.Bennett and H. Baker, Am. Soc. for Metals, Ohio, (1986) 202.

[91] D.K. Sadana, Nucl. Inst and Meth., B7/8 (1985) 375.

[92] D.K. Sadana, M. Strathman, J. Washburn, G.R Booker and M.H. Badawi, Mat. Res. Soc. Symp. on Defects in Semiconductors, eds. J. Narayan and T.Y. Tan, (Nov 1980) 515.

[93] E. Friedland, N.G. van der Berg, J. Hanβmann and O. Meyer, Surf. and Coatings Techn., 83 (1996) 10.

[94] A.G. Foyt, F.J. Leonberger and R.C. Williamson, Appl. Phys. Lett., 40 (1982) 447.

[95] S.S. Gill and B.J. Ealy, J. Appl. Phys., 56 (1984) 1189.

[96] D.E. Davis, J.P. Lorenzo, T.G. Ryan and J.J. Fitzgerald, Appl. Phys. Lett., 35 (1979) 631.

[97] D.E. Davis, J. of Crystal Growth, 54 (1981) 150.

[98] D.E. Davis, E.F. Kennedy, J..J. Comer and J.P. Lorenzo, Appl. Phys.Lett.,36 (1980) 922.

[99] M. Kruer, L. Esterowitz, R. Allen and F. Bartoli, Infrared Physics, 16 (1976) 375.

[100] Binary Alloy Phase Diagrams, Ed. T.B Massalski, J.L. Murray, L.H.Bennett and H. Baker, Am. Soc. for Metals, Ohio, (1986) 1395.

[101] N.A. Skakun, I.G. Stoyanova, N.P. Dikil, P.A. Svetashev, A.S. Trokhin and A.L. Chapkevich, Sov. Phys. Semicond., 15 (1981) 1112.

[102] F.D. Auret, J. Elechtrochem. Soc., Vol. 129, 12 (1982) 2752.

[103] L.F. Mondolfo, Aluminium Alloys: Structure and Properties, Butterworth, England (1976) 552.

[104] L.F. Mondolfo, Aluminium Alloys: Structure and Properties, Butterworth, England (1976) 431.

[105] G. Petzow and G. Effenberg, Ternary Alloys, Vol(3), VCH Publishers, New York, (1993) 254.

[106] P. Müller, W. Wesch, V.S. Solovyev, P.I. Gaiduk, E. Wendler, F.F. Komarov and G. Götz, Nucl. Inst and Meth., B80/81 (1993) 721.

[107] L.F. Mondolfo, Aluminium Alloys: Structure and Properties, Butterworth, England (1976) 552.

[108] A. Föhl, R.M. Emrick and H.D. Carstanjen, Nucl. Inst. and Meth., 65 (1992) 335.